PLASMA-ASSISTED MBE GROWTH KINETICS AND CHARACTERIZATION STUDIES OF WIDE BANDGAP III-V EPITAXIAL MATERIALS

By

MARK LEE O'STEEN

Bachelor of Science
Southeastern Oklahoma State University
Durant, Oklahoma
1993

Master of Science
Oklahoma State University
Stillwater, Oklahoma
1995

Submitted to the Faculty of the
Graduate College of the
Oklahoma State University
in partial fulfillment of
the requirements for
the Degree of
DOCTOR OF PHILOSOPHY
December, 2000

LIST OF TABLES

LIST OF FIGURES

Figure Page

CHAPTER 1

INTRODUCTION

1.1 Overview

InN, GaN, and AlN are direct bandgap semiconductors with bandgaps of 1.9, 3.4, and 6.2 eV, respectively at room temperature.[1,2] Additionally, GaN and its associated alloys with In and Al are thermally stable, chemically inert, and mechanically robust.[2] The group III nitrides have been aggressively pursued in recent years for numerous optical, optoelectronic, and electronic applications. Unfortunately, viable bulk growth techniques have not yet been developed for the growth of the group III nitrides.[1–3] Consequently, most of the research is performed on materials grown either by metalorganic chemical vapor deposition (MOCVD) or molecular beam epitaxy (MBE).

This thesis will present the results of research conducted into the molecular beam epitaxial growth of GaN epitaxial layers and InGaN/GaN superlattice structures on Al_2O_3 (0001) substrates. A variation of conventional solid-source MBE called RF plasma-assisted molecular beam epitaxy (RF-MBE) has been used for this research. In this chapter, the background materials necessary to understand this thesis will be discussed. In particular, a discussion of the properties and interests in the nitrides will be presented. Additionally, MBE and RF-MBE growth and the characterization techniques used throughout this thesis will be discussed.

1.2 III-V Refractory Nitrides

1.2.1 Interest and Applications

As already mentioned, the group III nitrides are semiconductors with wide, direct bandgaps. These semiconductors are often referred to as the "refractory" semiconductors, because like the refractory metals, they are thermally stable, chemically inert, and mechanically robust. This combined with the fact that the bandgaps of the nitrides range from 1.9 to 6.2 eV at room temperature, makes it desirable to use the group III nitrides to fabricate devices for a number of optical, optoelectronic, and electronics applications.

1.2.1.1 Optoelectronic Devices. Since the group III nitrides have direct bandgaps that range from 1.9 to 6.2 eV at room temperature, it is possible, in principle, to fabricate light emitting diodes (LEDs) and laser diodes (LDs) that span the entire visible range of wavelengths. Numerous groups have already reported operation of current injection laser diodes. As evidence of this, the first 20 papers reporting operating current injection lasers[4–23] are listed in Table 1.1 on p. 3. Visible and UV laser diodes are anticipated to be used in a wide variety of devices ranging from color laser printers to optical storage devices such as CD and DVD players. Additionally, GaN doped with Er has been found to be an efficient emitter of 1.54 μm light over a wide range of temperatures. This is currently being pursued as a high efficiency, high power laser diode for fiber optic applications.[2] Furthermore, Nichia has already demonstrated LEDs that span the visible range of wavelengths and has developed LEDs which emit white light through the use of a UV excited phosphor. It is anticipated that LEDs based on the nitrides will be used in a number of applications ranging from high brightness color displays to high efficiency traffic signals. Lastly, the wide bandgaps of the nitrides combined with their refractory properties make the nitrides potentially useful in devices for use as solar blind detectors for space applications.

No. of QWs	Current type	Temp.	J_{th} (kA/cm^2)	Wavelength (nm)	Ref.	Company/ University
26	pulsed	RT	4.0	417	4	Nichia
20	pulsed	RT	9.6	416	5	Nichia
20	pulsed	RT	8.0	410	6	Nichia
10	pulsed	RT	13.0	419	7	Nichia
7	pulsed	RT	4.6	406	8	Nichia
1	pulsed	RT	2.9	376	9	Meijo
3	continuous	233 K	8.7	411	10	Nichia
25	pulsed	RT	50	417.5	11	Toshiba
3	continuous	RT	9.0	409	12	Nichia
3	continuous	RT	7.0	400	13	Nichia
4	continuous	20-70 °C	3.6	406	14	Nichia
4	continuous	RT	7.3	399–401	15	Nichia
4	continuous	RT	3.6	405-407	16	Nichia
8	pulsed	RT	48	402.8	17	CREE
	continuous	RT	11	404–435	18	CREE
4	continuous	RT	4	396-397	19	Nichia
10	pulsed	RT	12.7	420	20	UCSB
5	pulsed	RT	12	405–425	21	Fujitsu
5	pulsed	RT	9.5	417.5	22	Sony
	continuous	20–60 °C	1.5	390-440	23	Nichia

TABLE 1.1. The first 20 reports of operating current injection laser diodes based on GaN. Listed are the number of quantum wells in the structure (if reported), the type of current injection, operating temperature range, threshold current density, wavelength(s) of operation, and the company or university with which the authors were affiliated. Reprinted from Ref. 24 with permission of the author.

1.2.1.2 Electronic Devices. In addition to optical applications, there are numerous electronics applications for the nitrides as well. The high thermal stability of the nitrides makes them potentially useful for numerous high-temperature and high-power devices. Already, Pankove *et. al.*[2] have demonstrated the operation of a heterojunction transistor based on the group III nitrides operating at 535 °C. Additionally, GaN is being pursued as an alternative to microwave devices based on other III-V materials in order to achieve higher power operating conditions. Such devices are of particular interest to the telecommunications industry, where the effective ranges of cell phones are often limited by the power at which microwave transistors can be operated.

1.2.2 Technological Challenges

Despite numerous recent achievements in the growth of devices based on the nitrides, significant technological challenges remain. Currently, the two most significant challenges are (1) the lack of suitable substrates, and (2) difficulties in doping the nitrides. Unfortunately, the GaN bulk crystals that can be produced at this time are not viable for serious growth research due to their small size and low rate of production. GaN crystallizes in either a wurtzite or zincblende structure, with the wurtzite structure being the thermodynamically more stable of the two. Additionally, the lattice parameters of GaN are small compared to most other semiconductors.[2,3] Consequently, there are few suitable substrates for GaN overgrowth. A suitable choice for a substrate must (1) be crystallographically matched to GaN (in terms of the stacking sequence and lattice parameters), (2) be thermally stable at typical growth temperatures, (3) have a coefficient of thermal expansion similar to that of GaN, and (4) have electrical properties that can be modified through doping. Currently, the most popular choices for substrates are Al_2O_3 and SiC. These materials are popular either for their availability at low cost (in the case of Al_2O_3) or for the better crystallographic match to GaN (in the case of SiC).

Additionally, doping remains a technological challenge as well. Epitaxial films that are not deliberately doped are generally found to have a high n-type carrier

concentration. This autodoping has most often been attributed to N-vacancies in the material.[2,3] For materials that are deliberately doped, the most commonly used dopants are Si and Mg for n-type and p-type doping, respectively. The nitrides are readily doped n-type using Si, which has a binding energy reported to be in the range 15–27 meV.[2,3] Doping to achieve p-type material remains a more challenging problem. The binding energy of the Mg acceptor level has been reported to be in the range of 150–250 meV.[2,3] Because of this large binding energy, only 1–5% of the Mg atoms are ionized at room temperature.[2] Consequently, extremely high Mg concentrations are needed to achieve high levels of hole concentrations.

1.3 Molecular Beam Epitaxial Growth

Molecular beam epitaxy (MBE) is one of a number of deposition techniques used to grow epitaxial thin films. MBE grown materials are generally of extremely high quality compared to those of other growth techniques. MBE growth offers a level of control over the epilayer composition and thickness which is difficult, if not impossible, to match in other growth techniques. Additionally, the UHV environment in which MBE growth is conducted allows for *in situ* characterizations, such as reflection high energy electron diffraction (RHEED), so that samples may be monitored in real-time during growth.

1.3.1 Solid-Source MBE Growth

Conventional MBE growth relies on the evaporation or sublimation of materials which are normally solids at room temperature and low pressure as sources for molecular beams. Consequently, this is often referred to as *solid-source* MBE growth. There are numerous variations of the conventional MBE growth process. However, all MBE growth techniques have three common core elements: (1) a pristine ultrahigh vacuum (UHV) growth environment, (2) a heated single-crystal substrate, and (3) controllable (usually shutterable) molecular beams incident on the heated substrate. These core components are depicted schematically in Fig. 1.1 on p. 6.

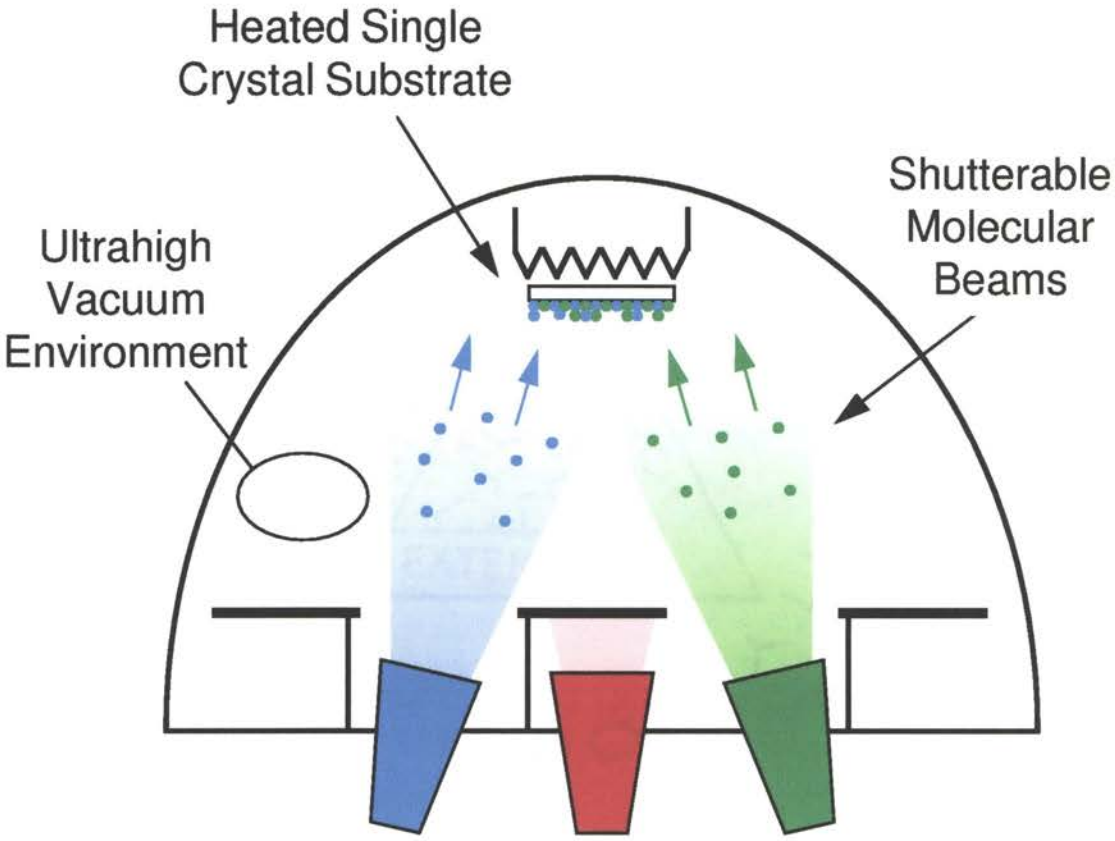

Figure 1.1. Core components common to all MBE growth techniques. MBE growth techniques will always involve (1) a heated single crystal substrate, (2) molecular beams which may be blocked by shutters, and (3) a pristine ultrahigh vacuum environment.

The UHV environment in which MBE growth is conducted is necessary for two reasons. First, it is necessary that species in the molecular beam flux have a large mean-free path to avoid (significant) attenuation through scattering collisions with the background gases in the chamber. Secondly, and more importantly, it is necessary the background gas pressure be orders of magnitude smaller than the beam equivalent pressures of the molecular beam fluxes so as to avoid serving as a large source of contaminants that may be incorporated into epilayers. The rate at which gas molecules impact a surface (expressed as a number/area/time) is related to its partial pressure p by $r = p/\sqrt{2\pi mkT}$, where m and T are the mass and temperature of the gas.[25,26] From this relationship, it can be shown that the partial pressure necessary to achieve a typical growth rate of 1 monolayer/s is approximately 10^{-6} Torr. Consequently, in order to prevent contamination of the sample, it is necessary that the background pressure in the chamber be in the UHV pressure range.

To achieve and maintain such a low base pressure in a vacuum system requires highly specialized equipment and operational procedures. In conventional MBE growth, ion-pumps are used exclusively. However, as will be elaborated upon later, the gas loads in plasma-assisted MBE growth require pumps with higher pumping speeds than are possible with conventional ion-pumps. Consequently, cryo-pumps and turbopumps are frequently used. Additionally, MBE growth chambers are normally manufactured using either type 304 or 316 stainless steel and are highly electropolished. Whenever the MBE growth chamber must be vented, it is necessary to perform a thorough bakeout procedure to expedite the removal of contaminants that become trapped on the growth hardware and chamber walls. Lastly, liquid nitrogen filled cryopanels within the growth chamber provide limited additional pumping during epitaxial growth. For the research presented in this thesis, both ion- and cryo-pumps have been used.

The next core component of MBE growth to be considered is the heated single-crystal substrate. The single-crystal substrate serves as a template for crystal formation as the epilayer is deposited. Ideally, the substrate should be the same material

as the first epilayer to be deposited. However, high quality bulk growth is not currently possible for many technologically useful semiconductors. In general, there are many factors to be considered in choosing a substrate for epitaxial growth. Most important among these are the crystal structure, lattice mismatch, thermal stability at the growth temperature, chemical compatibility, and degree to which the substrate's electrical properties can be modified through doping.

The single-crystal substrate must be heated with precise temperature control in order to thermally activate the migration of deposited species on the growth surface. For the research presented in this thesis, two different substrate heater configuration have been employed; both configurations are illustrated in Fig. 1.2 on p. 9. The first GaN epilayers were grown using the original MBE system substrate heater configuration, shown in Fig. 1.2(a). The original heater (designed for GaAs growth) was a resistive, serpentine style Ta foil filament attached to a pyrolytic boron nitride (PBN) support disk. Temperature measurements were performed by a thermocouple protruding through the center of the filament in direct contact with the substrate.

Due to the higher substrate temperatures used in the growth of the nitrides, there were a number of difficulties with the original stage heater configuration. Firstly, due to limitations of the electrical vacuum feedthru, the heater could only marginally achieve the high temperatures needed for the growth of GaN. Secondly, the Ta filament became embrittled when exposed to nitrogen under growth conditions and failed rapidly. Finally, the thermocouple in contact with the substrate acted as a heat sink, resulting in a cold spot at the substrate center.

The preponderance of samples for this thesis were growth using the second substrate heater configuration illustrated in Fig. 1.2(b). In this new heater configuration, there were several major changes: Firstly, the current carrying bus was substantially upgraded to allow for a greater electrical power to be applied to the filament. Secondly, the stage thermocouple was moved so that it measured the temperature of the PBN support disk rather than the temperature of the wafer. By doing so, the heat sink due to the thermocouple was eliminated; however, the temperature measurements from the thermocouple must be treated as a parametric value which can

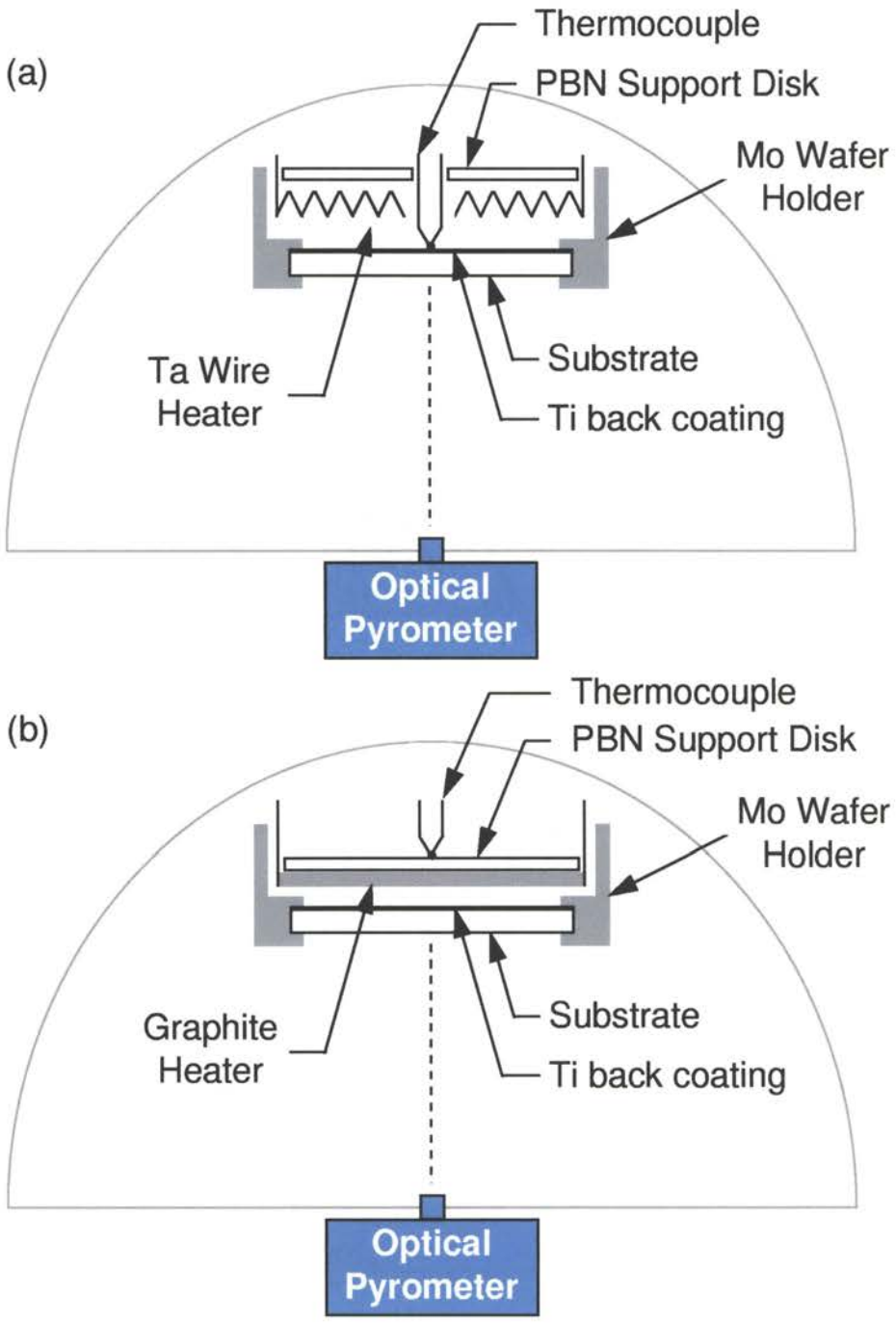

Figure 1.2. Sample heater configurations used in the growth of III-V semiconductors. In the first configuration (a), the substrate is heated by a serpentine Ta foil heater; the thermocouple is in direct contact with the substrate. The second heater configuration (b) uses a spiral graphite filament to facilitate heating the substrate to higher temperatures with improved uniformity.

be calibrated against the substrate temperature rather than as a direct measure of the substrate temperature. Finally, the Ta foil filament was replaced with a spiral graphite filament. This new filament design allowed for higher substrate temperatures and an improved chemical resistance to the nitrogen plasma. Additionally, the new filament design combined with moving the thermocouple provided for improved temperature uniformity across the substrate. A typical temperature distribution map is presented in Fig. 1.3 on p. 11. A 3 °C standard deviation in the surface temperature is observed.

The last of the core components of MBE growth are the molecular beam fluxes. In solid-source MBE, molecular beams are usually generated using Knudsen or Langmuir style effusion cells. A schematic drawing of a typical effusion cell is shown in Fig. 1.4 on p. 12. An electrical current is driven through the wire heater in order to heat the crucible and either evaporate or sublimate the source material. The temperature of the crucible is monitored using a ring thermocouple in direct thermal contact with the base of the crucible. Typically, the thermocouple voltage is used to regulate the electrical power delivered to the cell via standard electronic controllers. Since the temperature of the crucible cannot change quickly in response to changes in the applied electrical power, it is necessary to place a mechanical shutter at the orifice of the effusion cell. By opening and closing the shutter, molecular beams may be effectively turned on and off at the response rate of the mechanical shutter.

The material flux from an effusion cell observed at a particular point of the wafer is a function of both the cell temperature and the growth geometry. The dependence of the material flux on cell temperature is well described by an Arrhenius factor; that is, the flux J is given by $J(t_{cell}) = J_0 e^{\frac{-\Delta H}{kt_{\text{cell}}}}$, where ΔH is the heat of evaporation, t_{cell} is the cell temperature, and J_0 is a calibration factor.* In general, it is not practical to derive an analytic expression describing the material flux as a function of position on the growth surface. Firstly, the details of the crucible shape and the system geometry leads to expressions that are prohibitively complex. Additionally, detailed

*The details of the calibration procedure to obtain J_0 are described in Section A.2 of Appendix A.

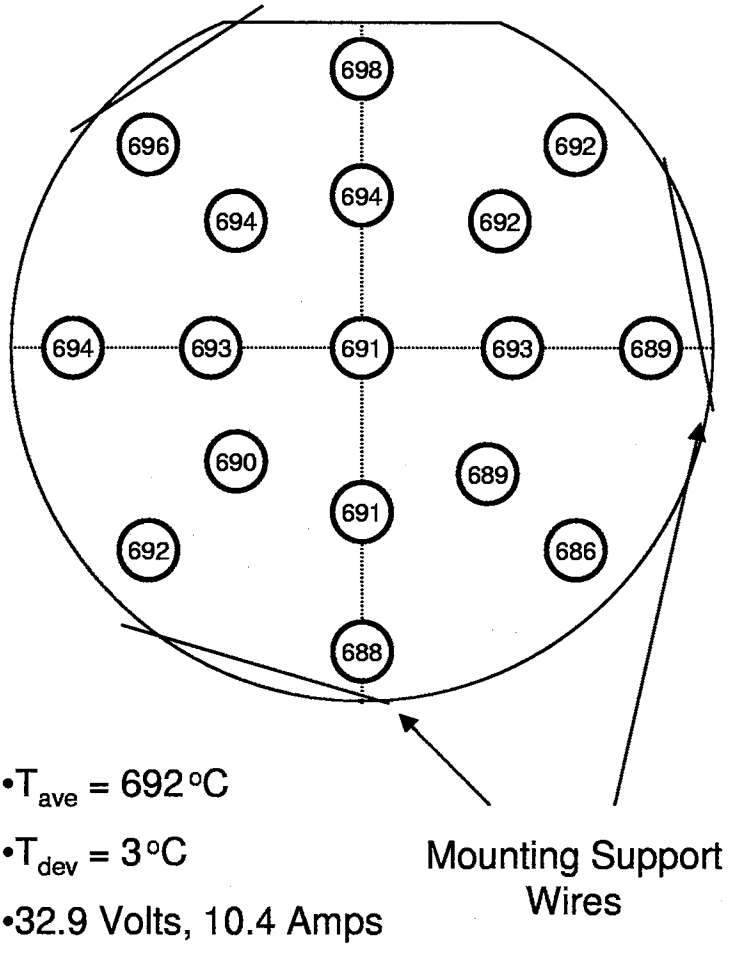

Figure 1.3. Typical wafer temperature distribution indicating high uniformity across the wafer surface. Temperatures were mapped by directional optical pyrometer measurements. For this test, the wafer heater was operated at 32.9 V and 10.4 A under open-loop control. The average temperature is 692 °C with a standard deviation of 3 °C.

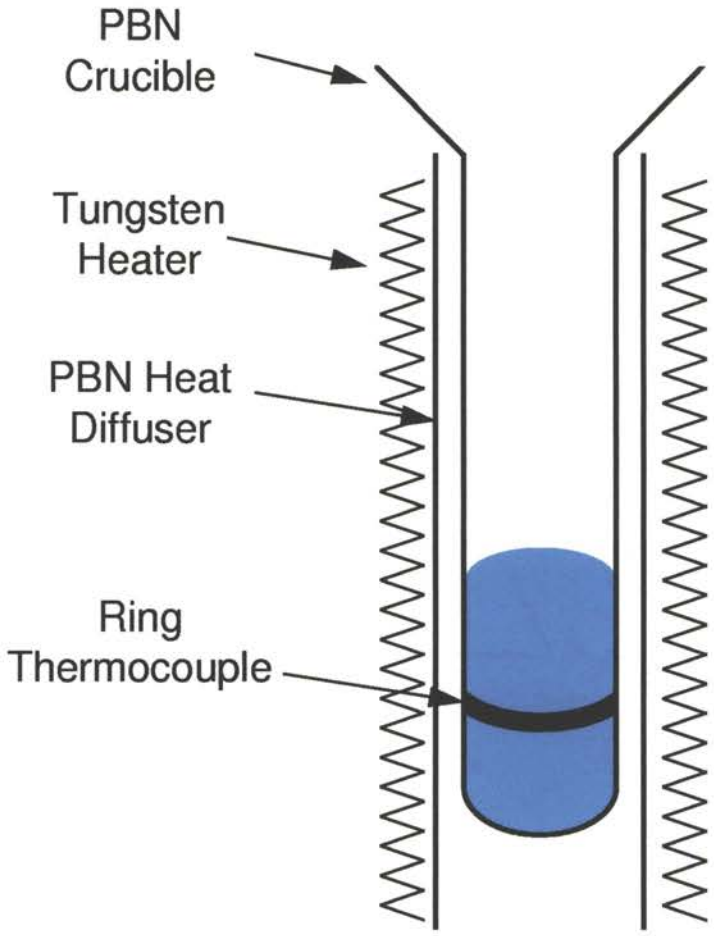

Figure 1.4. A conventional effusion cell used to generate metal fluxes. Source materials for molecular beams are evaporated from pyrolytic boron nitride (PBN) crucibles heated by a tungsten filament. A PBN heat diffuser is used for improved temperature uniformity and to reduce thermal stresses. A ring thermocouple measures crucible temperature and is used to regulate the electrical power provided to the cell.

effects, such as nonuniform heating of the source material and re-evaporation of source material from the crucible walls, limit the accuracy of such expressions. The material flux dependence on the system geometry is typically approximated by a simple cosine factor for the angular displacement from the molecular beam axis[26,27] and a simple cosine factor for the tilt of the substrate with respect the molecular beam axis.[25] Lastly, the material flux dependence on the distance from the effusion cell may be approximated by a $1/r^2$ law.[25–27]

1.3.2 Plasma-Assisted MBE Growth

The major difference in plasma-assisted MBE growth (of the nitrides) as compared to conventional solid-source MBE growth is the use of N_2 as a gas source. The N_2 triple bond is one of the most stable in nature; 9.81 eV of energy is required to disassociate a single N_2 molecule.[28] Because of the large bond strength, N_2 does not react at the growth surface at temperatures typical of MBE growth. Therefore, it is necessary to use an RF plasma source to generate a flux of active nitrogen species.

The particular RF plasma source used in this research, an SVT Associates model 4.5 RF plasma source, has several advantages and disadvantages when compared to other plasma sources. Firstly, the plasma source is very stable, relatively easy to operate, highly repeatable, and requires very few utilities. More importantly, the plasma source produces sufficient active nitrogen species for deposition at reasonable growth rates; GaN growth rates of 0.8 μm/h are readily achieved. Older generations of RF and ECR plasma sources achieved maximum growth rates of only 0.1-0.2 μm/h.[29] Lastly, the relative fraction of neutral N monomers is significantly higher than in older generations of plasma sources. Despite these advantages, there are several drawbacks to plasma sources and this source in particular. Firstly, plasma sources emit large numbers of high energy ions (50 eV or more) which can damage the growth surface.[3] Additionally, a large N_2 gas flow (approximately 1-5 sccm) is necessary to maintain a stable plasma; consequently, the plasma source has a limited dynamic range. That is, the activated nitrogen flux can be tuned only over a limited range without quenching

the plasma. Lastly, the large gas flow into the plasma source results in a high N_2 background pressure in the vacuum chamber during growth.

The high N_2 background pressure impacts the MBE growth process in several ways. Firstly, conventional ion-pumps cannot handle the high N_2 gas load. Therefore, a 2000 l/s cryo-pump was used in lieu of the standard ion-pump during deposition of the nitrides. Additionally, the high chamber pressure shortens the mean-free path of the molecular beams. In particular, the mean free path of Ga at a typical chamber pressure of 5.0×10^{-5} Torr is approximately 2 m.[30] Consequently, the molecular beam fluxes are attenuated slightly due to scattering. Additionally, the presence of N_2 gas and activated N species shortens the lifetime of filaments in the MBE growth chamber. This is particularly the case for filaments which operate at high temperatures, such as RHEED or wafer heater filaments or filaments which are directly exposed to the N* flux. In many cases, the refractory metals used for filaments can be replaced with thoriated-iridium filaments for an improved lifetime.

The RF plasma source used for the research presented in this thesis is shown in Fig. 1.5 on 15. The RF plasma source is effectively an RCL circuit. In vacuum, a PBN plasma cup is mounted within the induction coil of the circuit. External to the vacuum chamber, a variable capacitor is tuned for resonance at the 13.56 MHz fixed frequency of the RF generator. Ultrahigh purity N_2 gas enters the plasma cup through a controlled leak. The large magnetic fields in the induction coil at resonance induce eddy currents in the nitrogen gas, ionizing it and generating a plasma. A flux of activated nitrogen species escapes through a small orifice in the plasma cup. The plasma source releases a variety of nitrogen species including monomers and dimers which are both neutral and ionized (positively and negatively). Collectively, the species escaping through the orifice are referred to as the flux of active nitrogen N*.

1.3.3 Fundamental Principles and Growth Modes

Ideally in MBE growth, the laws of thermodynamics dictate the behavior of species deposited on the growth surface. The fundamental underlying physical principle of MBE growth is the energy minimization principle; that is, the free energy

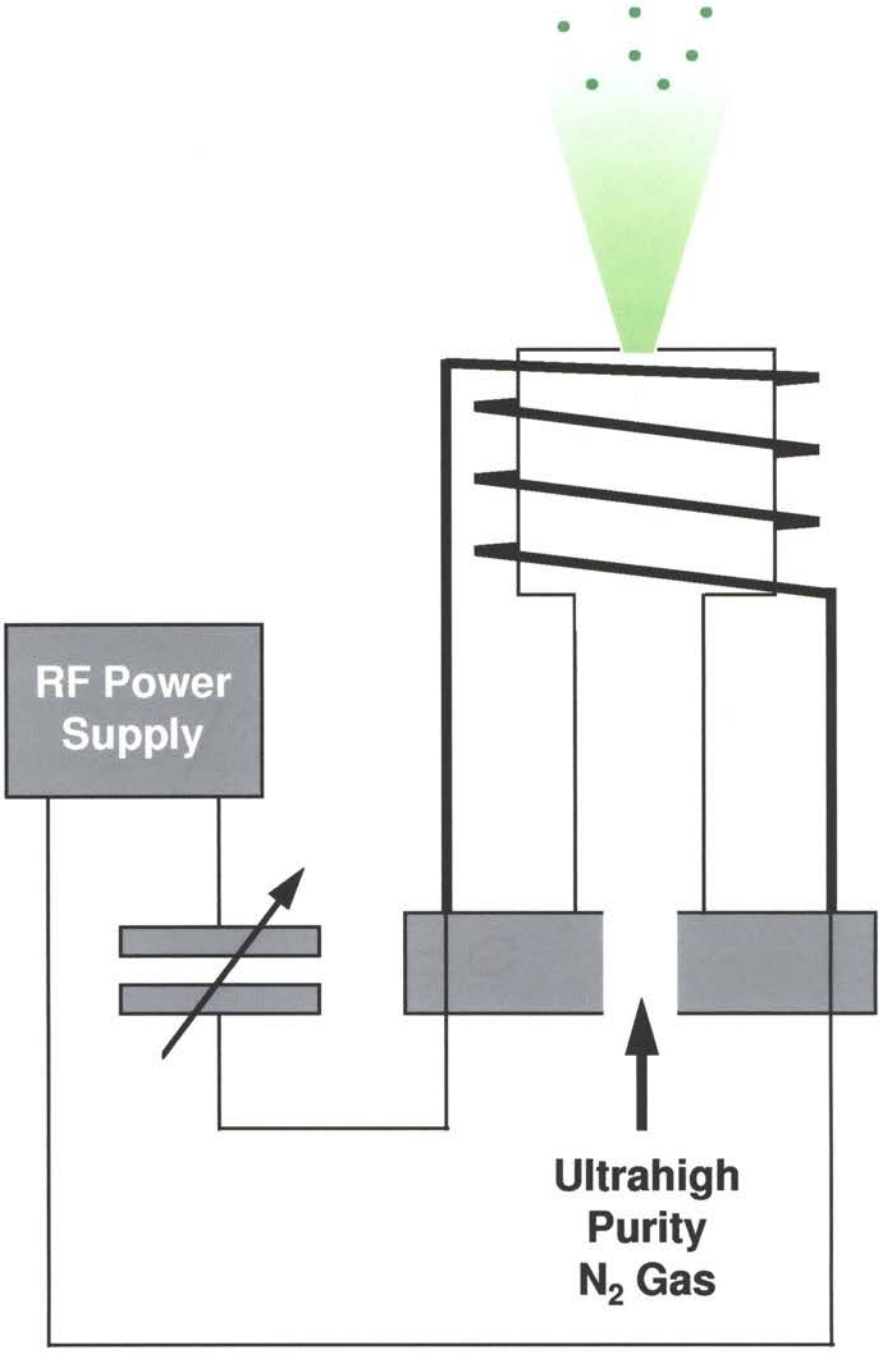

Figure 1.5. RF plasma source used to generate the N* flux. The RF plasma source is effectively the inductor in an RCL circuit. When the variable capacitor is tuned for resonance, eddy currents are induced in the nitrogen gas in the plasma cup.

of the sample is minimized. Dangling bonds at the sample surface have a greater free energy than bonds within the sample. Consequently, minimization of the free energy of sample requires minimizing the number of dangling bonds at the surface, or minimizing the area of the growth surface. Through careful control of the relevant growth conditions (flux arrival rates and substrate temperature), deposited species may migrate about the sample surface and incorporate at sites which minimizes the free energy of the sample.

This is illustrated more graphically in Fig. 1.6 on p. 17. A species (atom, ion, or molecule) deposited on the growth surface may incorporate at any of a number of sites on the surface. Three specific types of sites are considered in the figure. Let the energy associated with a species incorporating at sites A, B, and C be E_A, E_B, and E_C respectively; that is, for example E_A is the depth of the energy well that the species is trapped in when incorporating at site A. It is clear that due to the increasing number of dangling bonds that would be eliminated, it must be the case that $E_A < E_B < E_C$. Additionally, under normal growth conditions, migration of deposited species parallel to the growth surface is much greater than diffusion perpendicular to the growth surface; that is, since it is energetically favorable to remain at a step, it is unlikely that species will migrate away from step edges. Therefore, deposited species are energetically driven to accumulate at step edges. In this way, layer-by-layer growth is achieved through the coalescence of islands to form a continuous monolayer. In general, the above process for layer-by-layer growth is strongly affected by the MBE growth conditions. Indeed, it is the goal of the MBE grower to optimize material quality by controlling this process via the growth parameters. The mean diffusion time, rate, and length of species deposited on the surface are strongly affected by the substrate temperature, the arrival rate of species at the surface, and the concentrations of the species that compose the surface.

Deposition of epitaxial layers is generally described as proceeding in one of three growth modes. These growth modes are depicted in Fig. 1.7 on p. 18. The Volmer-Weber growth mode, shown in Fig. 1.7(a), is island-like growth and is commonly the result of crystalline dissimilarity, strain, or chemical incompatibility.[26] The second

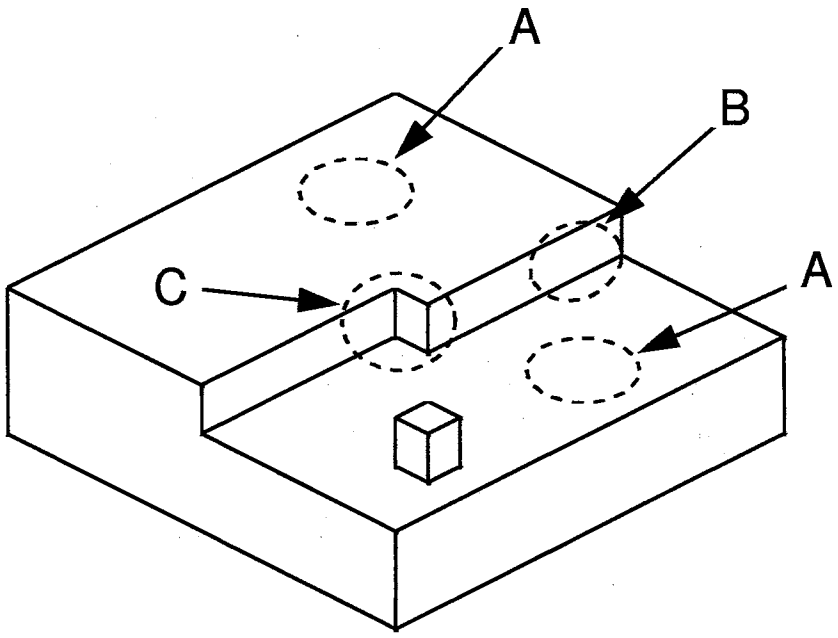

Figure 1.6. Minimization of surface free energy during growth. Material deposited on the surface during growth may migrate to many different types of incorporation sites. Deposited materials have a low probability of incorporating in open areas such as A; there is a higher probability of incorporation at step edges such as B. The surface free energy is minimized when deposited material incorporates at a site such a C, where the largest number of dangling bonds are eliminated.

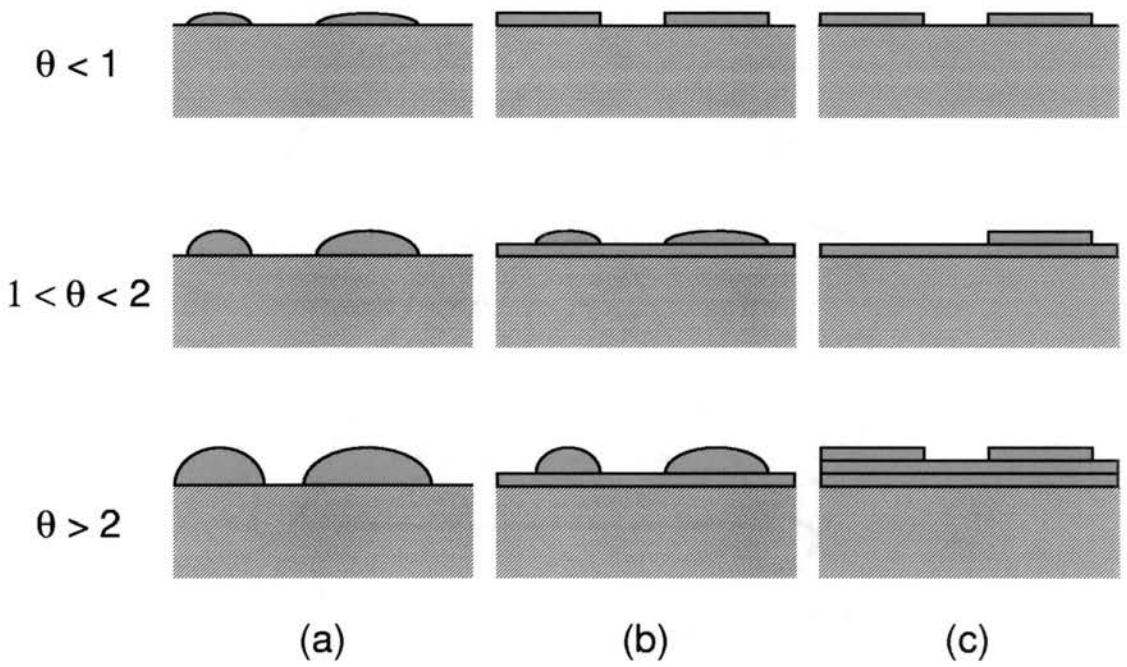

Figure 1.7. MBE growth modes in the absence of layer interdiffusion. Presented are a (a) islanded Volmer-Weber growth mode, (b) Stranski-Krastanov growth mode with layer-plus-island growth, and (c) layer-by-layer Frank-van der Merwe growth mode. The fractional monolayer coverage is represented by θ.

growth mode shown in Fig. 1.7(b), the Stranski-Krastanov growth mode, is a combination of layer and island growth. This growth mode usually occurs as the result of strain relaxation in epilayers with a large lattice mismatch.[26] The growth mode desired for MBE growth is presented in Fig. 1.7(c). Frank-van der Merwe growth proceeds as layer-by-layer growth and is observed under favorable epitaxial growth conditions.[26]

The growth mode during layer deposition can be understood simply in terms of free energy densities of the various surfaces, if one assumes effects due to chemical reactions at the interface, interdiffusion and alloying, and crystalline anisotropy may be neglected. Let S_{sub}, S_{lay}, and S_{int} be the surface free energy densities associated with the substrate surface, the epilayer surface, and the substrate-epilayer interface, respectively. In order for two-dimensional layer growth to occur, it must be the case that $S_{\text{sub}} \geq S_{\text{lay}} + S_{\text{int}}$, that is, coverage of the substrate by the epilayer must not raise the total free energy density.[31] Likewise, in the case that $S_{\text{sub}} < S_{\text{lay}} + S_{\text{int}}$, the growth will be islanded or three-dimensional.[31] Additionally, the condition for Stranski-Krastanov growth can be understood as well. Assuming that Stranski-Krastanov growth mode proceeds in order to reduce strain in the epilayer, the above condition for two-dimensional growth may be restated as $\mathrm{S_{sub}} \geq \mathrm{S_{lay}} + \mathrm{S_{int}} + Ut$, where U is the elastic energy density for an epilayer of thickness t.[31] The elastic energy density is given by $U = \frac{1}{2}\tilde{\mathbf{e}} \cdot \mathsf{C} \cdot \mathbf{e}$ where $\mathbf{e}$ and C are the usual strain and elastic stiffness tensors.[32]

1.4 Characterization of Epitaxial Materials

A number of characterization techniques have been used to study the samples discussed in this thesis. The different techniques can be separated into two broad categories: structural and optical. Each characterization technique will be briefly discussed and the underlying physics will be presented.

1.4.1 Structural Characterization Techniques

1.4.1.1 RHEED. Reflection high energy electron diffraction (RHEED) is arguably the single most important *in situ* characterization method used during MBE growth. RHEED provides non-destructive, structural characterization of the sample surface in real time. RHEED is extremely sensitive to the asperity, composition, crystalline structure, and reconstruction of the growth surface. Consequently, RHEED is extremely useful in characterizing the state of the surface during growth and the evolution of the surface as growth conditions are varied.

The experimental geometry used for RHEED is illustrated in Fig. 1.8 on p. 21. A beam of high energy electrons (7–10 keV) is incident on a crystal surface at a grazing angle (1–3°). The electron beam is diffracted by the crystal structure of the surface. The diffracted electron beam impinges upon a phosphor screen resulting in a viewable diffraction pattern.

The diffraction patterns observed in RHEED are most easily understood through use of the Ewald construction. Thus, it is first necessary to understand the reciprocal space of the sample. Since the electron beam is incident at grazing incidence, the momentum into the surface is extremely small. Consequently, the e-beam penetrates only a few monolayers into the surface.[25,33] Given this, the e-beam effectively "feels" only the surface net rather than the sample's three-dimensional crystal structure. In the case of an infinitely extended crystal with three-dimensions in real-space, the reciprocal-space, or G-space, contains a regular arrangement of points in three-dimensions. Now consider a two-dimensional surface net; for definiteness, assume that the net is contained entirely in the XY-plane. In this case, there is no periodicity along the Z direction in real-space. Consequently, the absence of periodicity along the Z direction in real space results in infinitely extended rods along the G_z direction in G-space rather than discrete points. However, the periodicity along the G_x and G_y directions in G-space is preserved.

The Ewald construction for RHEED is illustrated in Fig. 1.9 on p. 22. The wavevectors of the allowed diffractions are given by the intersection of the Ewald

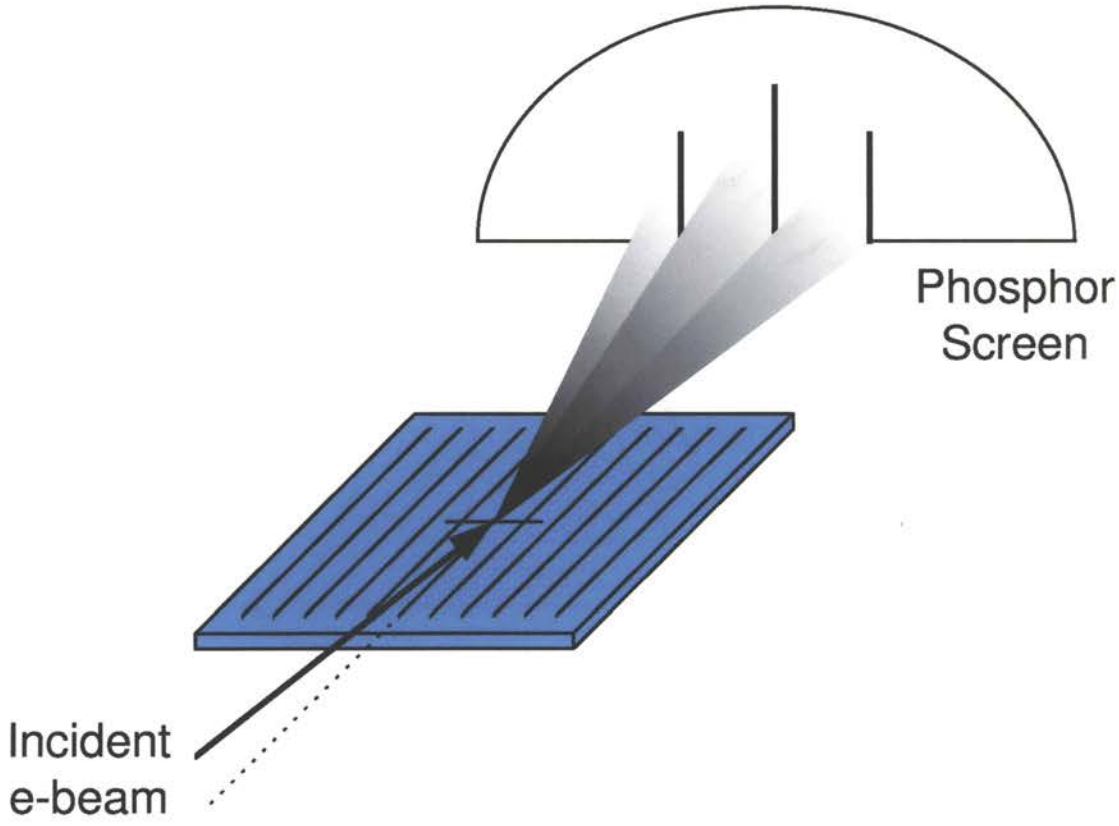

Figure 1.8. Reflection high energy electron diffraction (RHEED) geometry. A beam of high energy electrons (7-10 keV) is incident on sample surface at a grazing angle (1–3 °). The electron beam is diffracted by atomic rows in the surface lattice only when a constructive interference condition is satisfied. The diffracted beam impinges upon a phosphor screen resulting in a viewable image.

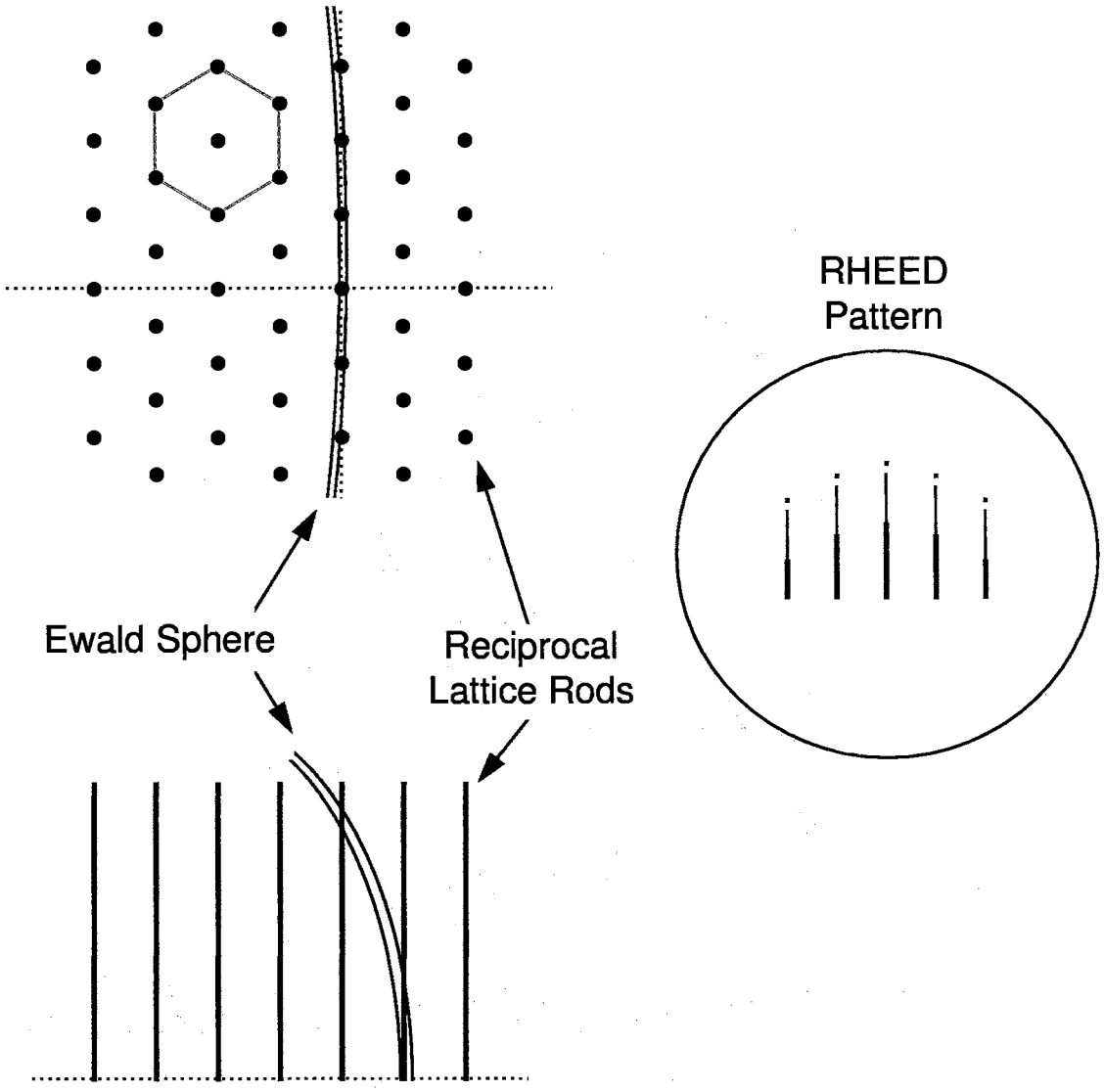

Figure 1.9. Ewald construction illustrating diffraction patterns observed in RHEED. Typically in RHEED, the radius of the Ewald sphere is many times larger than the reciprocal lattice translation vectors. The wavevectors of the allowed diffractions are given by the intersection of the Ewald sphere with the reciprocal lattice rods. The diffracted electrons impinge upon a phosphor screen resulting in a viewable image.

sphere with the reciprocal lattice rods. The G-space for a hexagonal surface net is shown in plan and side views. As a visual aid, the conventional hexagonal unit cell is shown in grey in the plan view. For the accelerating voltages used in RHEED, the radius of the Ewald sphere is large compared to the shortest reciprocal lattice translation vector.* In practice, the Ewald sphere has a finite thickness due to energy variations and divergence of the electron beam. Additionally, the reciprocal lattice rods have a finite thickness due to crystal imperfections and thermal vibrations. As a result of this, the intersection of the Ewald sphere with the reciprocal lattice rods is extended over some length of the reciprocal lattice rods. The RHEED pattern that is observed as a result of this consists of line segments that progressively shorten into spots.

Two important points need to be emphasized about RHEED patterns. Firstly, due to the diffraction geometry, the lines observed in RHEED patterns are orthogonal to the surface net (growth surface). Additionally, the degree to which RHEED patterns are "streaky" or "spotty" is a measure of the flatness of the growth surface. That is, as the growth surface begins to roughen, the diffraction becomes more like three-dimensional diffraction, and spots are observed rather than streaks in RHEED patterns.

RHEED patterns are affected by the surface reconstruction as well the surface crystal structure. Fractional order lines due to surface reconstructions are routinely observed in RHEED patterns. In fact, the grower often desires to maintain a particular surface reconstruction during epilayer deposition. In order to understand the

*The radius of the ewald sphere is equal to $2\pi/\lambda$ where λ is the de Broglie wavelength of the electrons. It is a straight-forward problem in special relativity to show:

$$\lambda = \left[\frac{h^2}{2m_e eV\left(1+\frac{eV}{2m_e c^2}\right)} \right]^{\frac{1}{2}},$$

where h, m_e, e, c, and V are Planck's constant, the rest mass of the electron, the charge of the electron, the speed of light, and accelerating voltage of the electron beam, respectively.[34] Using the above, the radius the Ewald sphere is approximately 52Å^{-1} for a typical accelerating voltage of 10 kV, whereas the shortest reciprocal lattice vector in the hexagonal surface net for GaN is $\frac{2\pi}{a} \approx 1.97\text{Å}^{-1}$.

fractional order lines observed in RHEED due to surface reconstructions, it is necessary only to consider the reciprocal space of a reconstructed surface.

As examples, the real and reciprocal spaces for cubic and hexagonal surfaces are shown in plan view in Fig. 1.10 on p.25. For definiteness, assume the cubic surface has a (2×2) surface reconstruction; that is, the reconstruction of unterminated surface bonds forms a unit that repeats once for each "2 by 2" matrix of unit cells in the surface net. Since a real structure exists on the surface with twice the periodicity of the surface net, there will exists rods in reciprocal space with *half* the periodicity of the surface net. This is illustrated schematically for a single cell in Fig. 1.10. The additional features in reciprocal space allow additional diffractions of the electron beam which are observed as half order lines in the RHEED pattern.

The situation is similar for the hexagonal surface shown in Fig 1.10. The hexagon traditionally used to represent the surface structure is not primitive; both the conventional unit cell (hexagon) and primitive unit cell (rhombus) are indicated in the figure as visual aids. As indicated, a (2×2) surface reconstruction on the hexagonal surface similarly results in additional reciprocal lattice rods with half the surface net periodicity. Again, these additional reciprocal lattice rods allow for half-order lines in the RHEED patterns.

1.4.1.2 High Resolution X-ray Diffraction. High resolution X-ray diffraction (HRXRD) is a non-destructive characterization technique that is used to assess many aspects of the crystallographic quality of an epitaxial thin film. In addition to the crystallographic quality, HRXRD measurements can be used to accurately determine the composition of superlattice structures. Two different HRXRD experiments have been performed on the samples discussed in this thesis: "rocking curve" scans and ω-2θ scans. The diffraction geometry used for both of these measurements is presented in Fig. 1.11 on p. 27. As shown in Fig. 1.11(a), a highly monochromatic beam of X-rays is made incident on the surface of a sample mounted on the HRXRD system. The angle ω is the angle between the sample surface and the incident X-ray beam. Likewise, the angle θ is the angle between the incident X-ray beam and the family of

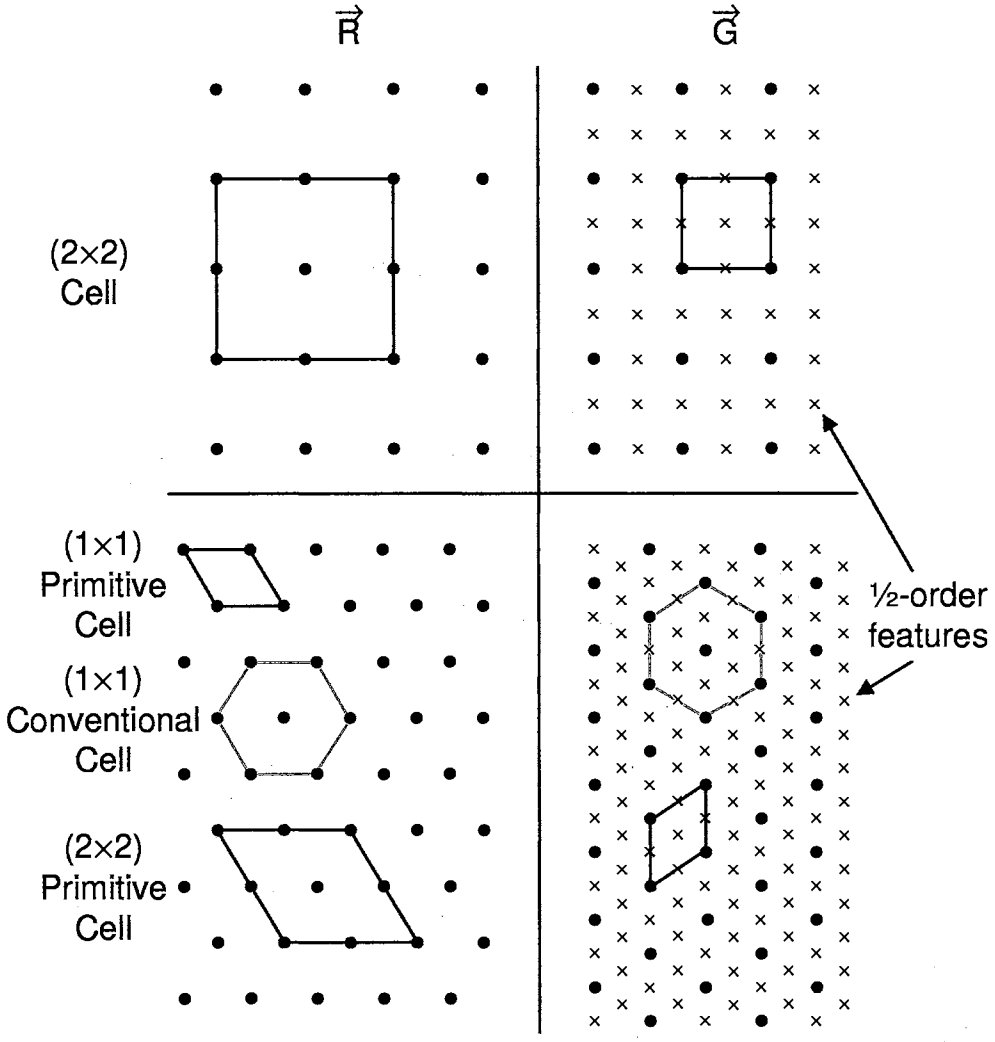

Figure 1.10. Real and reciprocal spaces for cubic and hexagonal surface nets. A real-space periodic surface reconstruction spanning a 2 by 2 matrix of cells results in reciprocal space features with *half* the periodicity of the cubic structure. The conventional unit cell (hexagon) and primitive unit cell (rhombus) for the hexagonal surface are indicated as visual aids. Again, a periodic "2 by 2" surface reconstruction feature on the hexagonal surface results in additional reciprocal lattice rods. Reciprocal space rods due to surface reconstructions allow additional lines to be observed in RHEED patterns (see text).

planes from which the incident beam is diffracted. Additionally, it must be the case that the angle between the diffracted beam and these planes is also θ.* As can be seen in the figure, it must necessarily be the case that the angle between the X-ray detector and the original line of the incident X-ray beam is 2θ. The wavevectors of the incident and diffracted X-ray beams are labeled $\vec{k}_{\text{in}}$ and $\vec{k}_{\text{out}}$, respectively.

The diffraction of X-rays from planes within the crystal may be understood using either the Bragg or von Laue formulations for X-ray diffraction. Fig. 1.11(b) shows the construction used in the Bragg formulation to explain the diffraction of X-rays. In this formulation, the X-rays are diffracted specularly from planes separated by a distance d. In order for constructive interference to occur, the path difference for X-ray reflected by different atomic planes must be equal to an integral number of X-ray wavelengths λ. By simply geometry, the path difference is $2d\sin\theta$. Consequently, the Bragg condition must be $n\lambda = 2d\sin\theta$.[34–37]

The von Laue formulation takes a more rigorous approach to determining the condition under which the diffraction of X-rays may occur. While it is too tedious to work through this formulation here, the basic elements of the model can be described. In this formulation, an array of point scatterers located on a Bravais lattice is considered. It is assumed that X-rays incident on this lattice may be treated as plane waves. Each plane wave is scattered as a spherically-symmetric electromagnetic wave. In order to determine the field amplitude that would be observed at a point outside the lattice, the amplitudes of the individual spherically-symmetric waves are integrated. From this, it is observed that in order for the amplitude to be non-zero, a diffraction condition must be satisfied. From this condition, diffracted beams of X-rays may only be observed when $\vec{K} \equiv \vec{k}_{\text{out}} - \vec{k}_{\text{in}} = \vec{G}$ where $\vec{K}$ is the scattering vector, $\vec{k}_{\text{in}}$ and $\vec{k}_{\text{out}}$ are the wavevectors of the incident and diffracted beams, respectively, and $\vec{G}$ is a reciprocal lattice vector of the crystal. For the interested reader, more detailed descriptions of this formalism exist elsewhere.[34–36,38]

*In the Bragg formulation of X-ray diffraction, it is assumed that these angles are the same. In the von Laue formulation, these angles are required to be the same as a rigorous consequence of the X-ray scattering being elastic.[34,35]

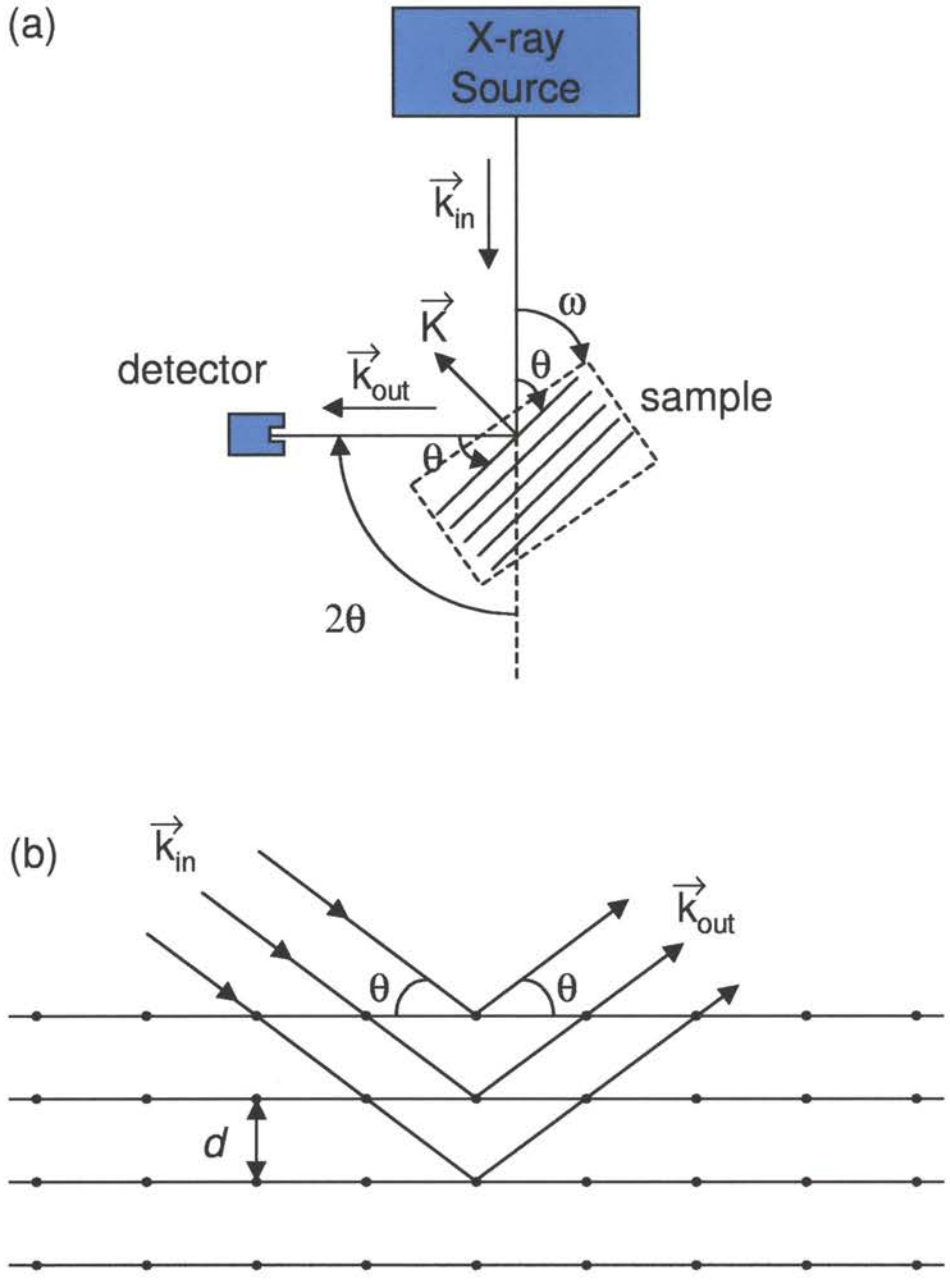

Figure 1.11. X-ray geometry for high resolution X-ray diffraction measurements. (a) Shown is a plan view of the experimental geometry. The angles ω and θ are defined in the figure. (b) Presented is the construction used to obtain the Bragg condition.

The diffraction condition stated above justifies the use of the Ewald construction for determining if diffraction of X-rays will occur. The Ewald construction for X-ray diffraction is shown in Fig. 1.12 on p. 29. In this construction, a sphere (with a radius of $2\pi/\lambda = |\vec{k}_{\text{in}}| = |\vec{k}_{\text{out}}|$), called the Ewald sphere, is superimposed on the reciprocal space of a crystal as shown in Fig. 1.12. The points in reciprocal space which intersect the Ewald sphere satisfy the diffraction condition $\vec{K} = \vec{G}$. Consequently, diffracted beam of X-rays may be observed along the direction of the wavevector $\vec{k}_{\text{out}}$.

The above formulation and constructions are extremely useful in understanding the two HRXRD measurements that are used in this thesis. The first of the HRXRD measurements to be considered is the rocking curve scan. This measurement is shown schematically in Fig. 1.13 on p. 30. In this measurement, the sample and detector are initially located so that a strong diffraction is observed from a particular family of planes. The slits on the detector are removed to deliberately create a large acceptance angle for the detector. Next, the incident beam of X-rays and the position of the detector are held fixed while the sample is rotated or rocked. The X-ray intensity is recorded as a function of the angular position of the sample. By initially setting the detector position and holding it stationary throughout the measurement, the value of the Bragg angle θ is constant. It can be seen from the Bragg condition, $n\lambda = 2d\sin\theta$, that for a particular value of θ, the instruments is configured to observe diffractions only from planes with a particular spacing d. Thus, the effect of this experiment is to test for the presence of planes with a spacing of d occuring at a angle to the normal orientation. In this way, the rocking curve tests for mosaic tilt in the sample.

It is also interesting to consider the rocking curve measurement in reciprocal space. This is shown in Fig. 1.13(b). Since the motions are relative, it is normally easier to assume a point of reference where the sample is stationary and the incident X-ray beam is rotated about the sample. Thus, in the figure, the reciprocal lattice points would remain stationary and the Ewald sphere is rotated about the origin of reciprocal space. In this way, the Ewald sphere is "rolled" through a feature in reciprocal space, revealing how extended this feature is along the scan axis indicated in Fig. 1.13(b).

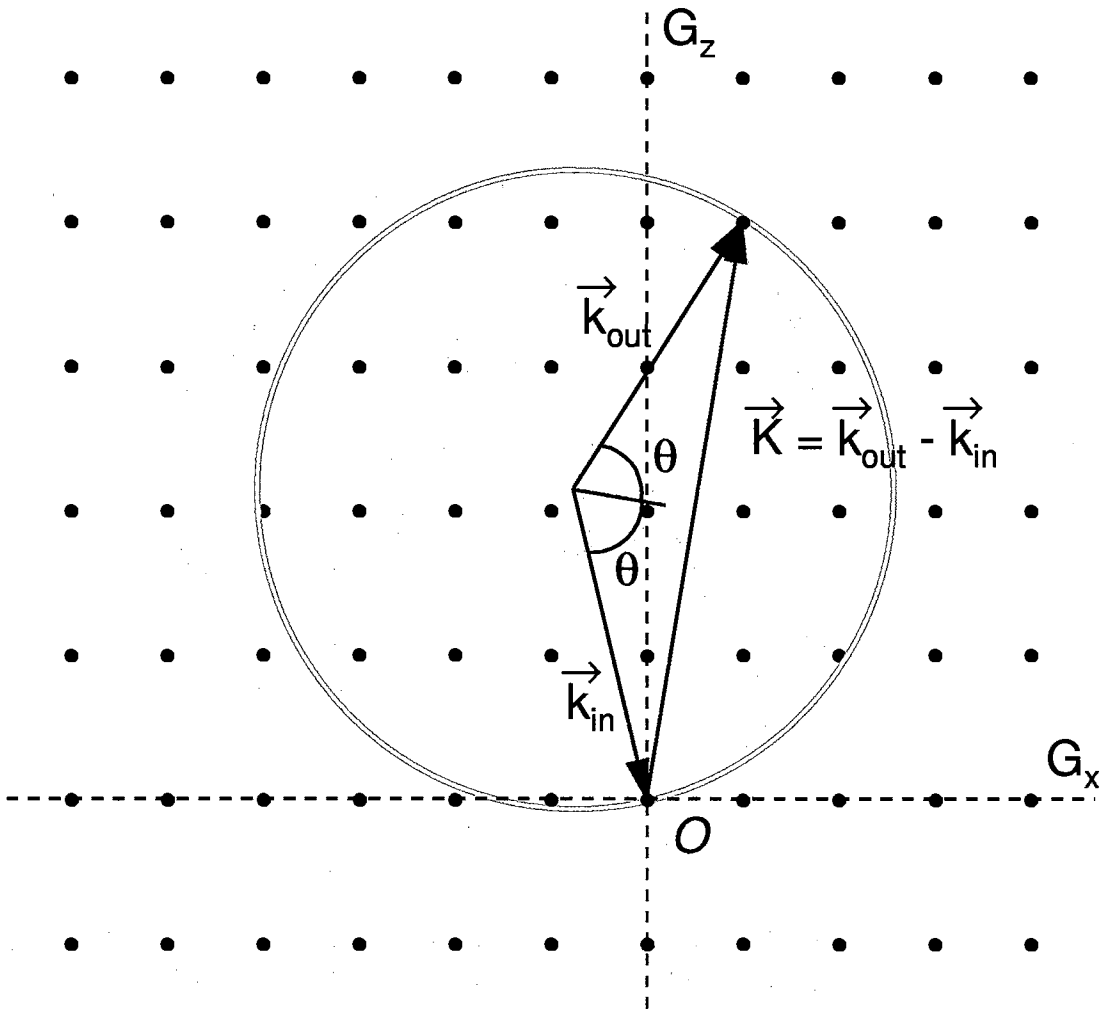

Figure 1.12. Ewald construction used in HRXRD measurements. The wave vectors $\vec{k}_{\text{in}}$ and $\vec{k}_{\text{out}}$ are associated with the incident and diffracted X-ray beams, respectively. The scattering vector $\vec{K}$ is defined as $\vec{K} \equiv \vec{k}_{\text{out}} - \vec{k}_{\text{in}}$. The condition for a diffraction to be allowed is $\vec{K} = \vec{G}$, where $\vec{G}$ is a reciprocal lattice vector.

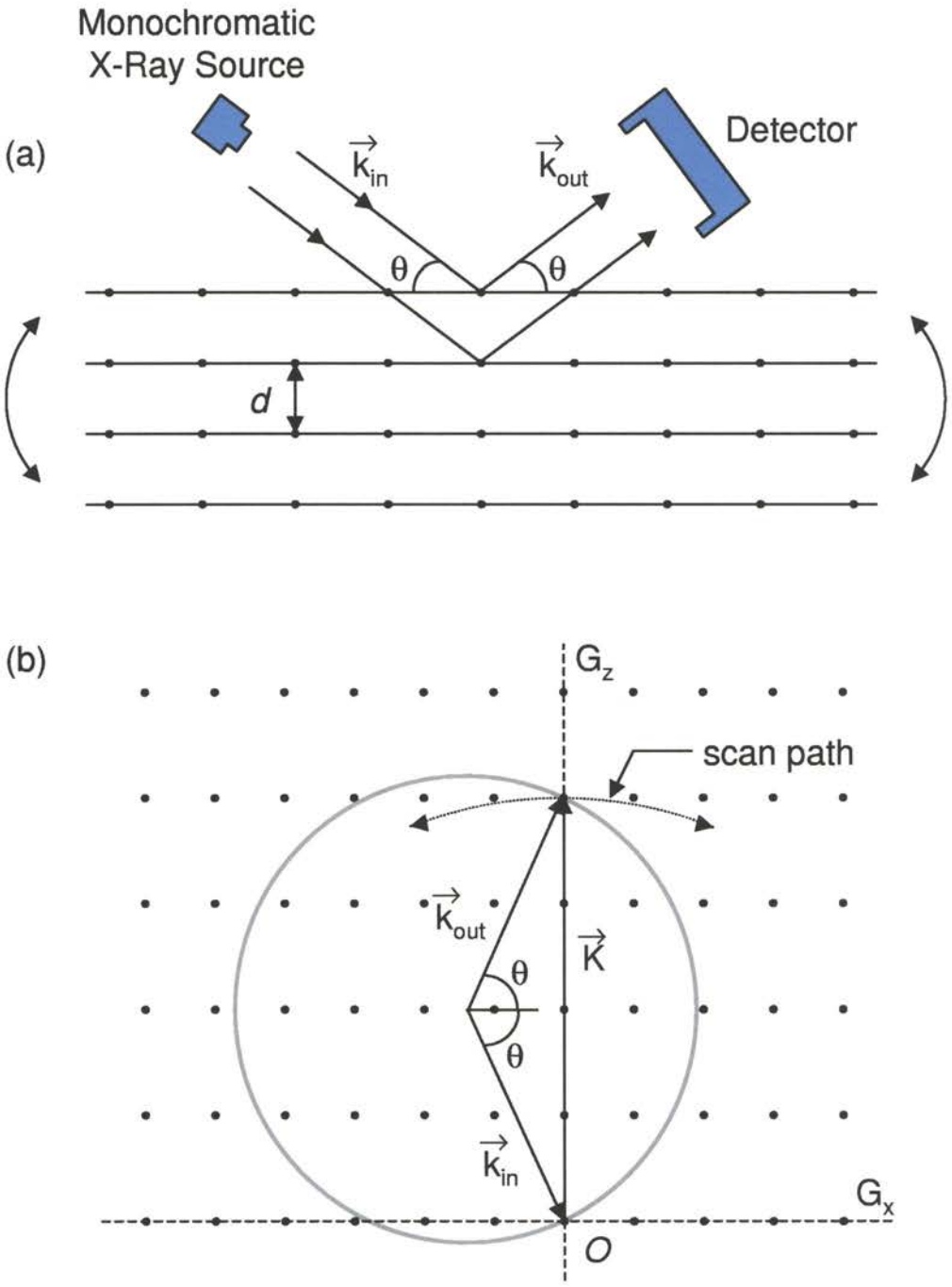

Figure 1.13. The rocking curve measurement in real and reciprocal space. (a) The incident X-ray beam and detector are held fixed while the sample is rotated. (b) In reciprocal space, the rocking-curve measurement acquires data along the indicated scan axis.

The ω-2θ scan may also be understood using the same formulations and constructions. The ω-2θ scan is illustrated in Fig. 1.14 on p. 32. In the ω-2θ scan, the sample and detector are initially positioned so that a strong diffraction is observed from a particular family of planes. In this measurement, either a slit or additional optics are installed on the detector to limit the acceptance angle. The sample and detector are then scanned simultaneously such that the detector moves at twice the angular speed of the sample. The intensity of the diffracted beam is recorded as a function of the angular position of the sample. As indicated in Fig. 1.14, the effect of scanning the detector and sample in this way is to vary the Bragg angle θ. Since the Bragg angle is varied, it can be seen from the Bragg equation, $n\lambda = 2d\sin\theta$, that the effect of this scan is to test for the presence of planes with a varying interatomic spacing. Additionally, it is also interesting to consider the ω-2θ measurement in the the reciprocal space of the sample. This is illustrated in Fig. 1.14(b). Since the angle of incidence of the X-ray beam and the angle of the detector relative to the sample are varied at the same rate, this measurement has the effect of moving the sampling volume along a ray directed from the origin of reciprocal space.

Lastly, it is interesting to consider the special case of *symmetric* rocking curve scans and ω-2θ scans. Symmetric scans are performed about diffractions from families of planes that are parallel to the sample surface. In this case, the angle ω is equal to the angle θ. Consequently, the reciprocal lattice features that may be probed using symmetric HRXRD scans must lie along the G_z-axis (assuming a (0001) growth direction). Symmetric rocking curve scans effectively measure the extent of reciprocal lattice features perpendicular to the G_z direction. As mentioned earlier, this indicates the presence of planes with mosaic tilt. Because of this, the width of rocking curve scans are an important figure of merit when considering the quality of epitaxial samples. Additionally, interesting information can be obtained from symmetric ω-2θ measurements. Since symmetric ω-2θ scans occur along the G_z direction in reciprocal space, the data obtained provides information about the interatomic plane spacings along the growth direction. This provides useful feedback concerning important aspects of samples such as the strain state of an epilayer or the composition of

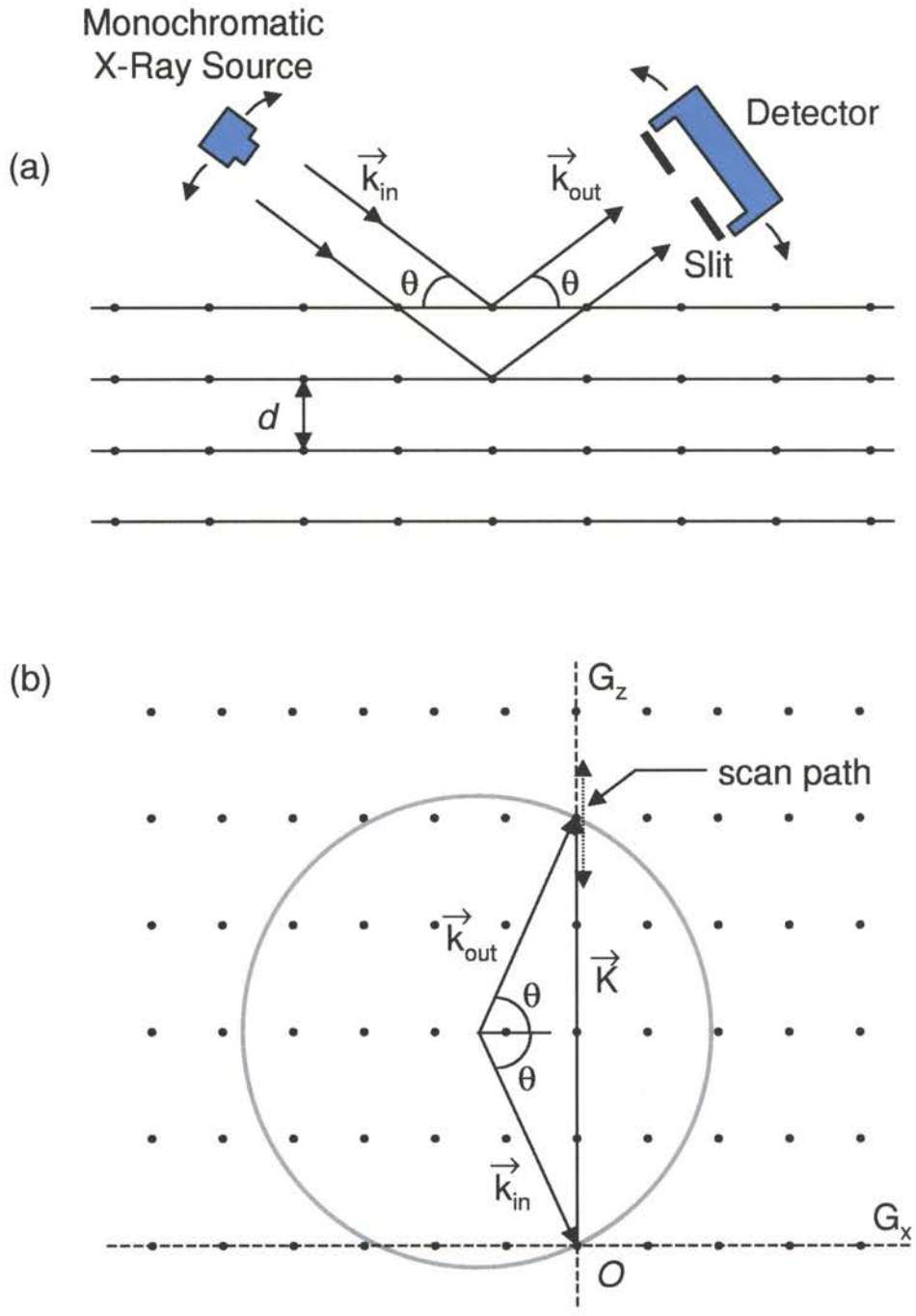

Figure 1.14. The ω-2θ in real and reciprocal space. (a) The detector and sample are moved such that the Bragg angle θ is effectively varied. (b) In reciprocal space, the ω-2θ scan acquires data along a ray oriented from the origin of reciprocal space.

an alloy layer. It will become evident in Chapter 3 that symmetric ω-2θ scans are particularly useful for samples containing a superlattice. Since a superlattice has a periodicity along the growth direction which is large compared to interatomic plane spacing, features are introduced in reciprocal space which have a periodicity which is small compared the normal reciprocal lattice points. These additional features result in satellite peaks in symmetric ω-2θ scans. The angular positions of these satellite peaks provides information about the period and average plane spacing of the superlattice structure. Assuming that θ_n is the angular position of the nth order satellite peak, the period L and average plane spacing $\bar{d}$ of a superlattice may be determined by fitting the superlattice equation[38,39]:

$$\frac{2\sin\theta_n}{\lambda} = \frac{n}{L} + \frac{1}{\bar{d}} \tag{1.1}$$

to the experimental data. This is discussed in greater detail in Chapter 3.

1.4.2 Optical Characterization

Two types of optical characterization have been performed in the research discussed in this thesis: reflectance spectroscopy and photoluminescence spectroscopy. These standard experiments will be briefly described in the following sections.

1.4.2.1 Reflectance. Reflectance spectroscopy is a straight-forward, non-destructive optical characterization that is routinely performed on the samples discussed in this thesis. The measurement utilizes Fabry-Perot resonances in the reflectance spectrum to determine the thickness of the deposited GaN epilayers. Since it is typically necessary to measure the thickness of a GaN epilayer at a number of points across the wafer surface, a novel experimental setup was devised for performing the reflectance measurements. This apparatus and the details of the reflectance measurement are discussed in detail in Appendix A beginning on p. 118.

1.4.2.2 Photoluminescence. Photoluminescence spectroscopy is a commonly used optical characterization technique used in the study of many different semiconductors. As will be discussed in Chapter 3, low-temperature photoluminescence measurements have been used to characterize InGaN/GaN superlattice samples grown under various growth conditions. The experimental setup used for these measurements (shown in Fig. 1.15 on p. 35) is typical of PL experiments used to study the group III-nitrides. In this experiment, 325 nm laser light from a HeCd laser is made incident on the sample surface. The HeCd laser generates a large number of plasma lines; therefore, it is necessary to use a prism and iris to disperse and block wavelengths other than the desired 325 nm line. As shown in Fig. 1.15, a mirror is used to redirect the laser onto the sample, which is mounted inside a cryostat. A lens is used to focus the laser to a spot less than 1 mm in diameter. Luminescence from the sample is collected and collimated by one lens and then focused onto the entrance slit of a Spex 1000M 1 m spectrometer equipped with a 1200 groove/ mm holographic grating blazed at 670 nm. The light is then detected by a Hamamatsu 1P28A photomultiplier tube.

In the photoluminescence experiment, photons with energies greater than the bandgap of the material are made incident on the surface of the sample. Absorption of these photons results in the generation of electron-hole pairs. Luminescence is observed when the radiative recombination of an electron-hole pair occurs. The total recombination rate, or total decay rate ($1/\tau_{\text{tot}}$), may be expressed as:

$$\frac{1}{\tau_{\text{tot}}} = \frac{1}{\tau_{\text{rad}}} + \frac{1}{\tau_{\text{nonrad}}} \quad , \tag{1.2}$$

where $1/\tau_{\text{rad}}$ and $1/\tau_{\text{nonrad}}$ are the radiative and nonradiative recombination rates, respectively.[1,40,41] Since nonradiative recombination tends to dominate at high temperatures,[1] samples are cooled to approximately 10 K. The energy of the observed light is characteristic of the states that were occupied by the electron hole-pair prior to recombination. Generally, there are many possible physical origins for the luminescence, including band-to-band transitions, excitons, and transitions among mid-gap states.

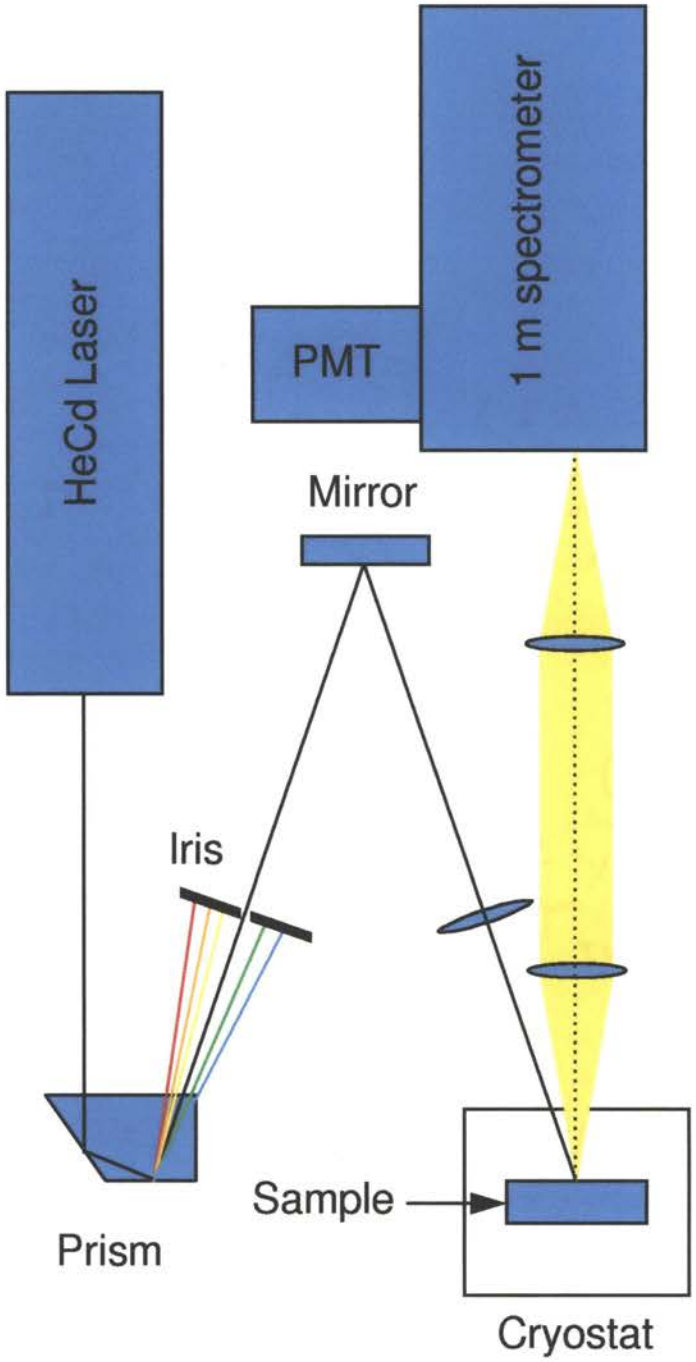

Figure 1.15. Experimental setup used for PL measurements. The 325 nm line of a HeCd laser is made incident on the sample, which is mounted in a cryostat, using a mirror and a lens. A prism and iris are used to disperse and remove unwanted plasma lines from the HeCd laser. Luminescence from the sample is collected into the spectrometer using two lenses and detected by a photomultiplier tube.

1.5 Outline of Thesis

The research presented in this thesis has been organized into two broad categories: RF-MBE growth of GaN epilayers and RF-MBE growth of InGaN/GaN superlattices. Chapter 2 will present the work on GaN epilayers. In this chapter, the effects of buffer layers and growth parameters on the growth of GaN epilayers and the quality of those epilayers is discussed. It will be shown that the most important growth parameters during the growth of GaN epitaxial films are the (1) substrate temperature, (2) N*/Ga flux rate, and (3) GaN growth rate. An interpretation of the effects of these growth parameters on the microscopic growth processes is presented. All of the observed growth results and phenomenology can be explained by the proposed microscopic growth processes.

In Chapter 3, the growth of InGaN/GaN superlattices is discussed. Several key results are obtained from these experiments. Firstly, it may be inferred from HRXRD results that InN requires a higher N*/III flux ratio than does GaN for stoichiometric growth. Secondly, it is found that the composition of the InGaN/GaN superlattices varies strongly as a function of the growth conditions. Importantly, the In composition of these superlattices will be shown to be strongly affected by the substrate temperature during growth and the incident N*/III flux ratio. Again, the results obtained from the growth of these superlattices may be understood in terms of microscopic growth processes occurring during deposition. Lastly, the results of this work will be summarized in Chapter 4.

CHAPTER 2

RF PLASMA-ASSISTED MBE GROWTH OF GaN EPITAXIAL LAYERS

2.1 Introduction

InN, GaN, and AlN are often referred to as "refractory" semiconductors because, like the refractory metals, they are thermally stable, chemically inert, and mechanically robust. Additionally, these are direct gap semiconductors with bandgaps of 1.9 eV, 3.4 eV, and 6.2 eV, respectively at room temperature. This range of bandgaps, combined with the desirable refractory properties, makes the group III-nitrides potentially useful in numerous applications as light emitting diodes (LEDs) and laser diodes (LDs) operating in the red to near-UV portion of the electromagnetic spectrum, solar-blind optical sensors, and high-temperature electronics.

GaN and its related alloys are primarily grown either by metalorganic chemical vapor deposition (MOCVD) or molecular beam epitaxy (MBE). This chapter will be concerned with research that has been performed in the growth of GaN epitaxial films on Al_2O_3 (0001) substrates by RF plasma-assisted molecular beam epitaxy (RF-MBE). The relevant RF-MBE growth phenomenology has been assessed though a variety of epitaxial growth experiments. Specifically, it has been found that the most important growth parameters are (1) the substrate temperature, (2) the incident N*/Ga flux ratio, and (3) the Ga flux rate. The effects of these parameters on the growth of GaN epitaxial films and the resultant quality of these films has been studied and will be discussed. The characterization techniques used to assess the quality of GaN epitaxial films include *in situ* reflection high energy electron diffraction (RHEED) and optical pyrometer interference measurements and *ex situ* high resolution X-ray diffraction (HRXRD), spatially-resolved reflectance measurements, and atomic force microscopy (AFM).

2.2 Experimental Details

GaN growth experiments were conducted by depositing epitaxial films on Al_2O_3 (0001) substrates by RF plasma-assisted molecular beam epitaxy. Epitaxial films were deposited using an SVT model 433R molecular beam epitaxy system. A conventional Perkin-Elmer style 20 cm^3 effusion cell was used to provide the Ga flux. In order to facilitate growth of the Nitrides, several modifications of the MBE system were necessary. Firstly, in order to pump the high N_2 gas loads during GaN growth, a CTI Cryogenics CT-8 2000 l/s cryo-pump was added to the system. Secondly, an SVTA model 4.5 RF plasma source was installed on the source flange. Ultrahigh purity (UHP) N_2 gas was flowed through particulate and chemical filters before entering the plasma source through a controlled leak. Lastly, after a number of GaN growth experiments, it was realized that higher substrate temperatures were needed than could be achieved using the original sample heater (designed for applications involving the arsenides). Consequently, the sample heater was replaced with a custom designed high-temperature wafer heater assembly. This wafer heater assembly was designed specifically to (1) allow heating to the higher temperatures needed for GaN growth, (2) provide an improved sample temperature uniformity, and (3) be more robust against the deleterious effects of the N* plasma.

The growth geometry used during the GaN epilayer deposition is shown in Fig. 2.1 on p. 39. Figure 2.1(a) shows the geometry schematically from a side view and Fig. 2.1(b) shows the geometry of the flux sources about the Al_2O_3 substrate. The Ga effusion cell and RF plasma source are located nearly diametrically opposite each other on the source flange. By locating the sources in this fashion, the variation in the N*/Ga flux ratio across the surface of the wafer is maximized. Since the Al_2O_3 substrates are normally *not* rotated during GaN deposition, growth at different points on the wafer represents growth under different N*/Ga flux ratios. As a result of this, the effects of small N*/Ga flux ratio variations can be studied by performing spatially-resolved characterizations across the sample surface. Additionally, the orientation of the Al_2O_3 unit cell relative to the wafer flat is indicated in Fig. 2.1(b).

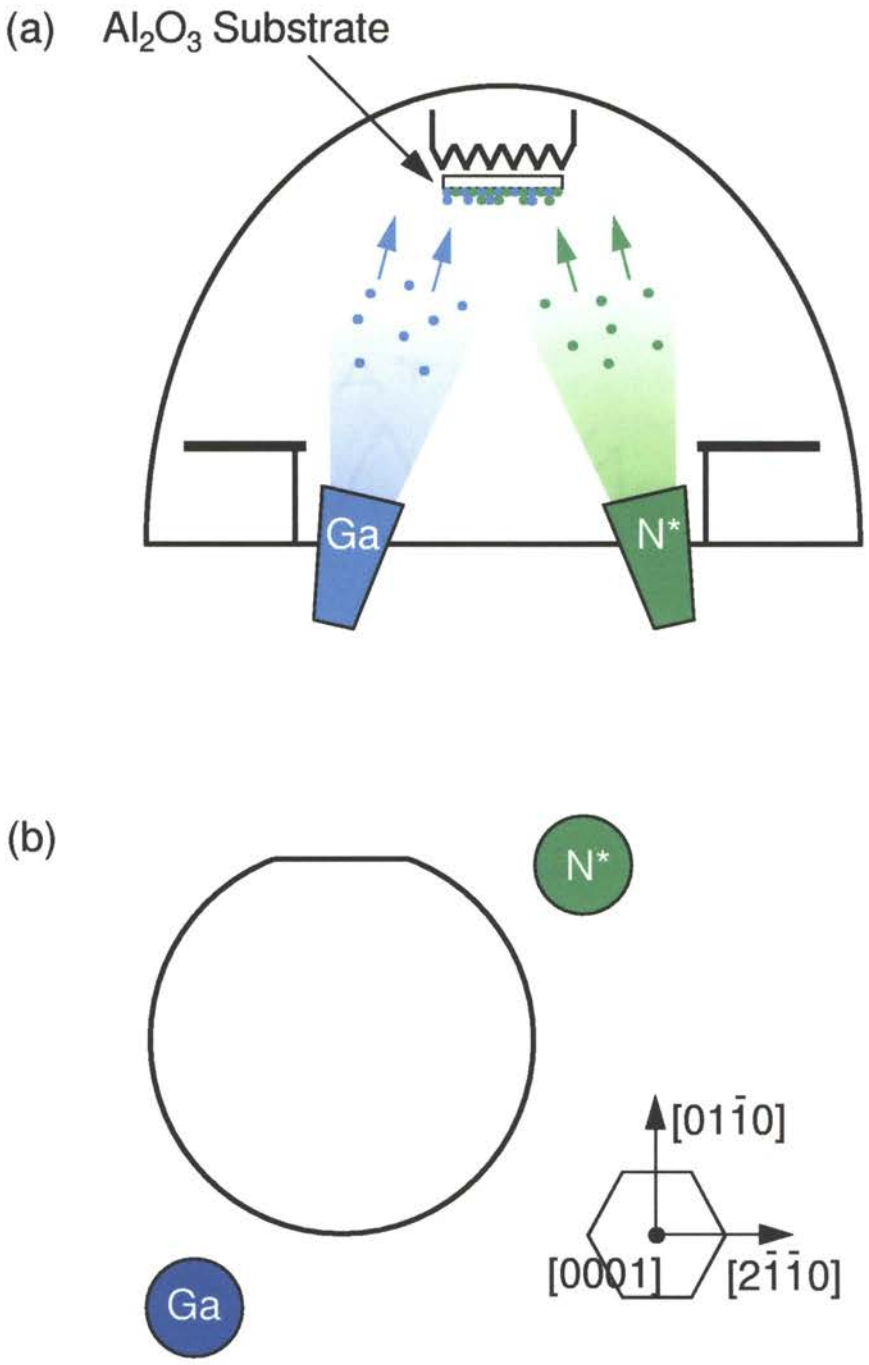

Figure 2.1. MBE system geometry used during GaN epilayer growth experiments. As shown in (a) the schematic side view and (b) a plan view about the Al_2O_3 wafer, the Ga and N* sources are located on nearly diametrically opposite sides of the wafer so as to maximize the N*/Ga flux ratio across the wafer surface. Additionally, the orientation of the Al_2O_3 unit cell relative to the wafer flat is indicated.

Two Mo holders were used to support the Al_2O_3 wafers during the GaN growth experiments. Both wafer holder designs are shown in Fig. 2.2 on p. 41. The original wafer holder, shown in Fig. 2.2(a), is similar in design to wafer holders conventionally used in GaAs growth. In this design, the wafer is supported on a lip machined into the Mo holder. The wafer is then held against this lip by three Ta wires pressing on the back of the wafer. This design had a number of limitations. Firstly, due to the large area of contact between the wafer edge and the supporting lip of the holder, there was poor temperature uniformity across the wafer. At high temperatures, this nonuniform temperature distribution could result in enough thermal stress to crack the wafer. Secondly, when mounted in the holder, the wafer is recessed slightly from the from surface of the holder; this significantly affects the angle at which the RHEED beam grazes the surface and limits the area of the surface that may be probed with the RHEED beam. Lastly, the procedure for installing and removing wafers was difficult and required significant handling of the wafer holder; this significantly increased the probability of contamination of the wafer and wafer holder.

The second Mo holder, shown in Fig. 2.2(b), was used for all GaN samples grown after the installation of the high-temperature heater assembly. This design captures the wafer between three Ta wires on each side. The advantages of this design include improving temperature uniformity by reducing the contact area with the holder, moving the wafer to the surface of the holder making the surface more accessible to the RHEED beam, and greatly simplifying the loading and unloading procedure. However, one significant drawback of this design is that the Ta support wires protrude into the growth area on the wafer.

Typically, GaN growth experiments were performed by growing one of two epitaxial structures. Both of these structures are presented in Fig. 2.3 on p. 43. The first structure, presented in Fig. 2.3(a), consists of a thin AlN layer formed by exposing the Al_2O_3 surface to the N* plasma, a thin (≈ 300 Å) GaN buffer layer grown at a low temperature, and a thick (1.0–1.5 μm) epilayer deposited at a normal epilayer deposition temperature. The second GaN sample structure, shown in Fig. 2.3(b) differs

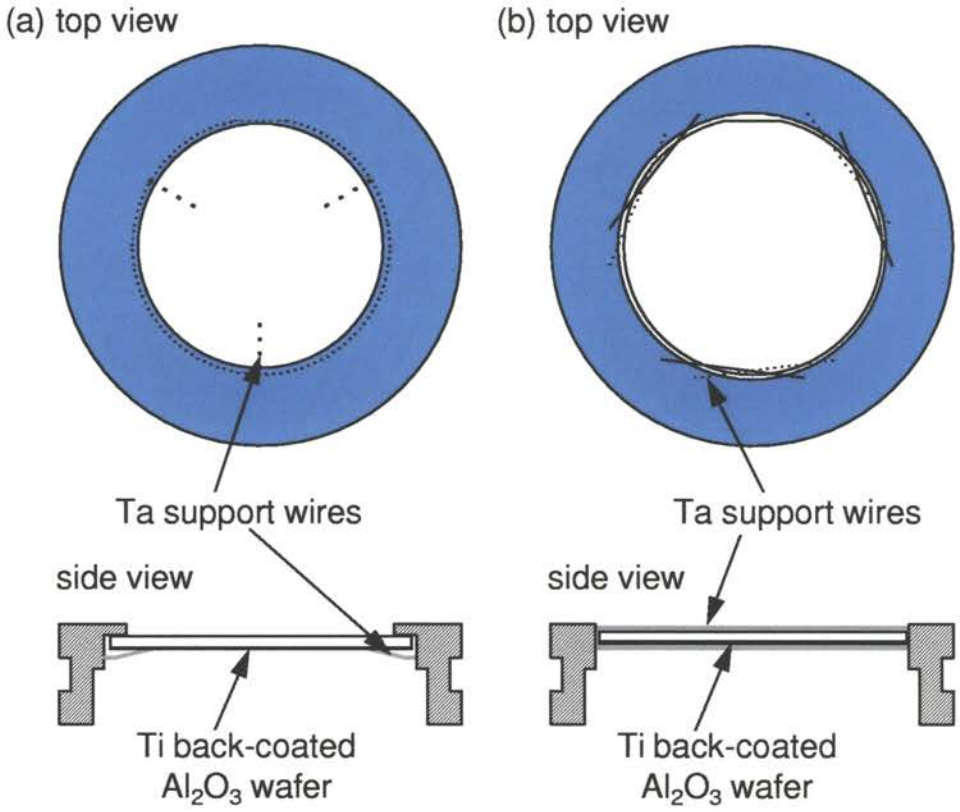

Figure 2.2. Molybdenum wafer holders used during GaN growth experiments. Top and side views are shown for each wafer holder. (a) In the conventional holder, three Ta wires press from behind to hold the wafer against a machined lip on the holder. (b) In the high temperature holder, the wafer is captured between 3 Ta wires on each side. The reduced contact area between the holder and wafer in this design provides for an improved temperature uniformity across the wafer and makes the surface more accessible to the RHEED beam.

only in that the low temperature GaN buffer layer is excluded; the reason for this will be discussed later.

A nominal procedure has been developed for growing either of the sample structures described above. Individual growth experiments typically involved some intentional deviation from this growth procedure. The nominal growth procedure is as follows. Firstly, the Al_2O_3 substrate is prepared for loading into the growth chamber. In the MBE chamber, the wafer is heated by a filament. In the regime of temperatures at which MBE samples are grown, the predominant mechanism of heat transfer is by radiation. However, Al_2O_3 is a very efficient window over a wide spectral range. Consequently, it is necessary to deposit an optically opaque Ti layer on the back surface of the wafer to act as an absorber.* The wafer is then loaded without chemical preparation into one of the Mo wafer holders described in Fig. 2.2 and the wafer holder is loaded into the growth chamber via a vacuum load-lock. The wafer is then outgassed at 300 °C to remove any water or hydrocarbon contaminants that may have settled on the wafer or holder. This outgassing is typically performed overnight prior to the day of the growth run. The outgassing time can be shortened, but should be always performed for at least 2 h.

Once this outgassing is completed, the growth experiment may begin. Prior to deposition of the first layer, the Ga cell, RF source, and wafer must be prepared for use. A carefully timed sequence of events is programmed into the electronics controlling the MBE hardware and the programs are executed. The Ga cell and wafer heater are "ramped" slowly to high temperatures to ensure that these items are thoroughly outgassed. The Ga cell is ramped to a temperature that is approximately 20 °C higher than maximum temperature needed for the growth run. The Ga cell is outgassed at this temperature for 5 min and is then ramped to an idle temperature (typically 900 °C). The wafer heater is programmed to reach its peak temperature, or "flash" temperature, simultaneous to the Ga cell beginning to ramp down. It is imperative that the wafer be at a high temperature while the Ga cell is outgassed;

*This deposition is performed in a separate metal deposition system; special care must be taken during this deposition to assure that no Ti can accumulate on the front surface of the wafer.

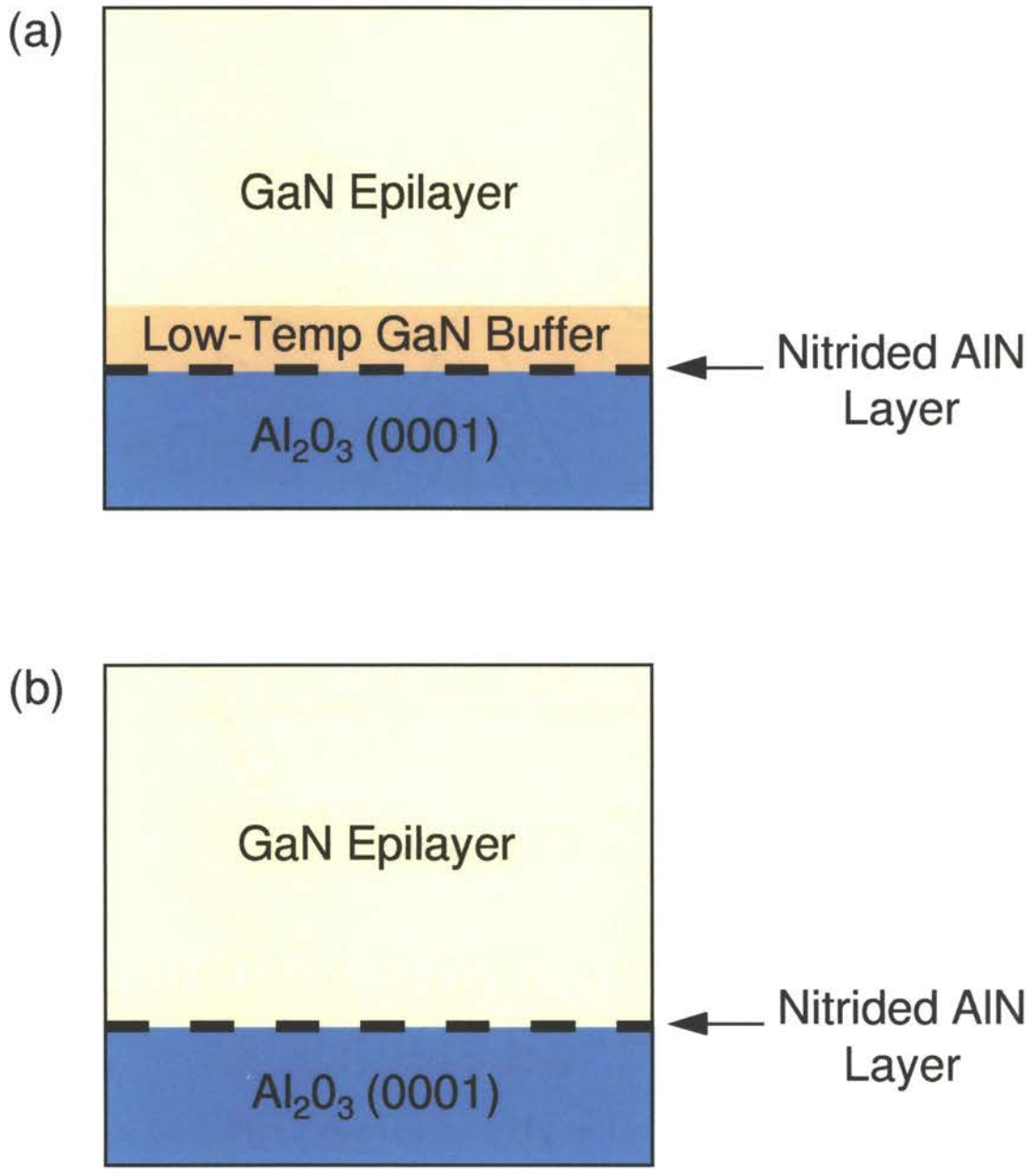

Figure 2.3. Sample structures used for GaN growth experiments. GaN epilayers were deposited on either (a) a GaN buffer layer grown at low substrate temperatures or (b) directly on the "nitrided" AlN layer.

this prevents contaminants from the Ga cell from depositing on the growth surface. After approximately 6 min, the wafer temperature is ramped to the temperature used for the surface nitridation (typically 740 °C). Simultaneous to outgassing the wafer and Ga cell, the RF plasma source is prepared manually. The RF forward power delivered to the plasma source is increased in steps of 50 W to a maximum power of 250 W. The gas manifold used to deliver N_2 gas to the RF plasma source is evacuated using a sorbtion pump and a cryo-pump.

At this point, the MBE system and wafer are ready for deposition. Prior to depositing any material, a controlled N_2 leak into the RF plasma source is established and the Al_2O_3 surface is exposed to the N* plasma (400 W forward power, 2.0×10^{-5} Torr chamber pressure) for approximately 45 min. This "nitridation" of the surface converts the Al_2O_3 surface to a thin layer of AlN which may be used for epitaxial overgrowth.

At this point, the growth procedures deviate for the two sample structures shown in Fig. 2.3. In order to deposit the low temperature buffer, the wafer temperature must be ramped to approximately 480–500 °C. The low-temperature GaN buffer is typically grown for 1 h using a Ga cell temperature $T_{Ga} \approx 900$ °C and a N* plasma condition of 400 W forward RF power at a chamber pressure of 2.0×10^{-5} Torr. This procedure deposits a GaN buffer approximately 300 Å thick.

Next, the MBE system must be prepared for deposition of the GaN epilayer. To do this, the Ga cell temperature must be increased in order to provide the Ga flux needed for deposition at a higher growth rate. The wafer temperature must also be adjusted to the level needed for the GaN epilayer (typically 735-750 °C). If a low-temperature GaN buffer has been deposited, it is necessary to ramp the wafer temperature simultaneous to the Ga cell ramp. If no low-temperature buffer is deposited, then the Ga cell temperature may be ramped simultaneously with the Al_2O_3 surface nitridation so that it is immediately ready for use once the surface nitridation is completed. Once the Ga cell temperature and substrate temperature have stabilized, the plasma may be ignited and stabilized at the operating condition for the epilayer deposition (typically 500 W forward RF power and a chamber pressure

of 5.0×10^{-5} Torr). In order to minimize damage of the growth surface due to leakage of the N* plasma around the shutter, the plasma should be stabilized and deposition initiated as quickly as possible after the plasma is struck. After the deposited GaN epilayer has attained sufficient thickness, the shutters should be closed and the plasma immediately quenched. The programs to ramp down the substrate temperature and Ga cell temperature should be executed as quickly as possible following the epilayer deposition to avoid any unintended deposition of Ga on the growth surface.

Data acquired during a typical GaN epilayer deposition is shown in Figs. 2.4–2.6 on pages 46–48. This data was collected using the automated computer logging described in Appendix A. Figure 2.4 shows the power applied to the Ga cell and the wafer heater as a function of time into the growth run. The applied power is expressed in units of "% Output", i.e. the fraction of maximum voltages that can be applied by the power supplies (80 V for the wafer heater and 25 V for the Ga cell). Figure 2.5 presents the variation of (a) the RF power applied to the plasma source and (b) the chamber pressure (an indicator or the N_2 flow rate) each versus the time into the growth run. Lastly, Fig. 2.6 reveals (a) the wafer heater temperature as measured by the optical pyrometer and (b) the power applied to the heater expressed in units of "% Output". For each of these figures, the major steps of the growth process are indicated.

2.3 Results and Discussion

The number of growth experiments that have been performed is sufficiently large to prohibit discussing them individually. Therefore, the results attained have been separated into two categories which will be discussed separately: results associated with buffers layers and results associated with growth conditions.

2.3.1 Buffers

Buffer layers are used as intermediate layers to either facilitate or improve the growth of any subsequent epilayers to be deposited. Two types of buffer layers have

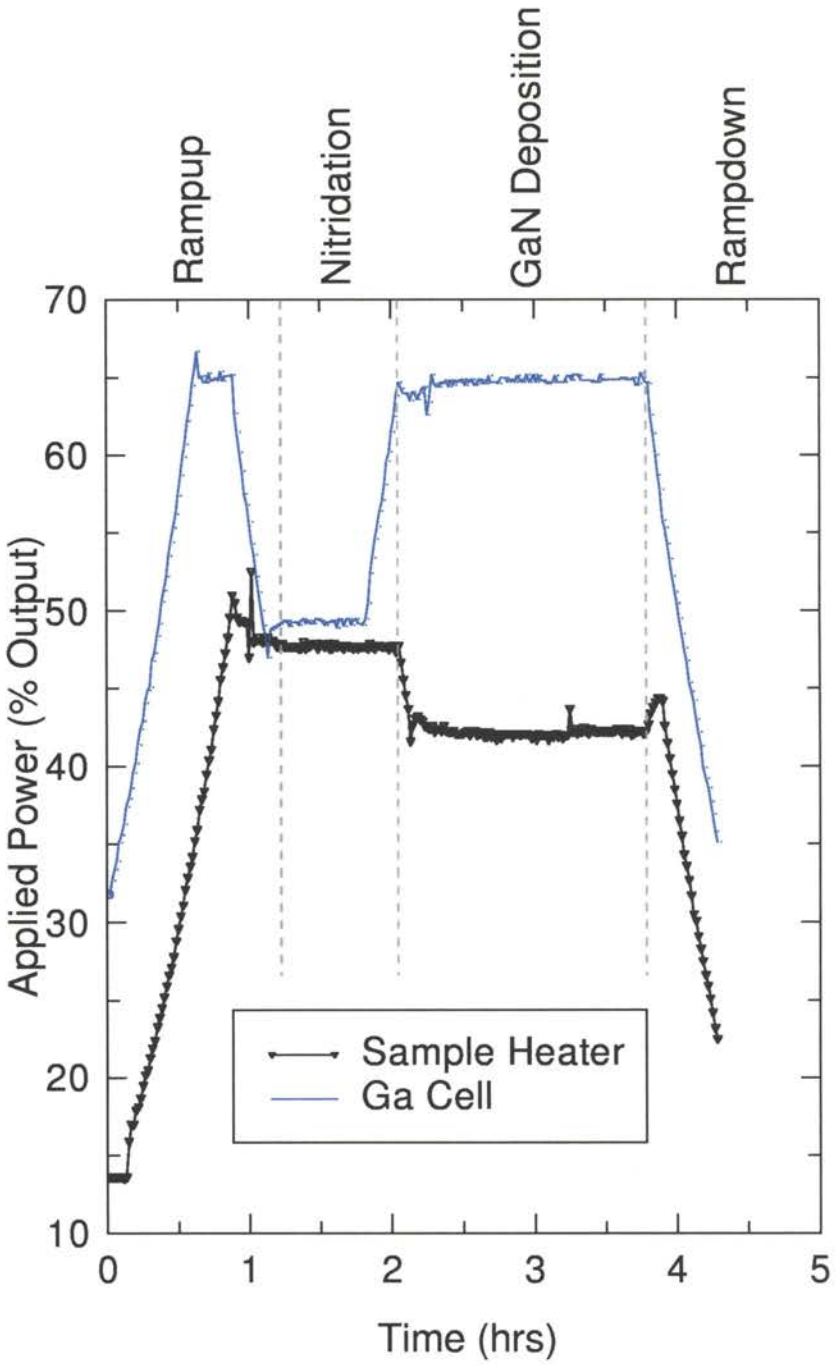

Figure 2.4. Power applied to the Ga cell and wafer heater during a typical GaN growth experiment. Powers are expressed in units of "% Output", that is, as a fraction of the maximum voltages (25 V for Ga cell and 80 V for the wafer heater) the power supplies can provide. The major steps of the growth experiment are indicated above the figure.

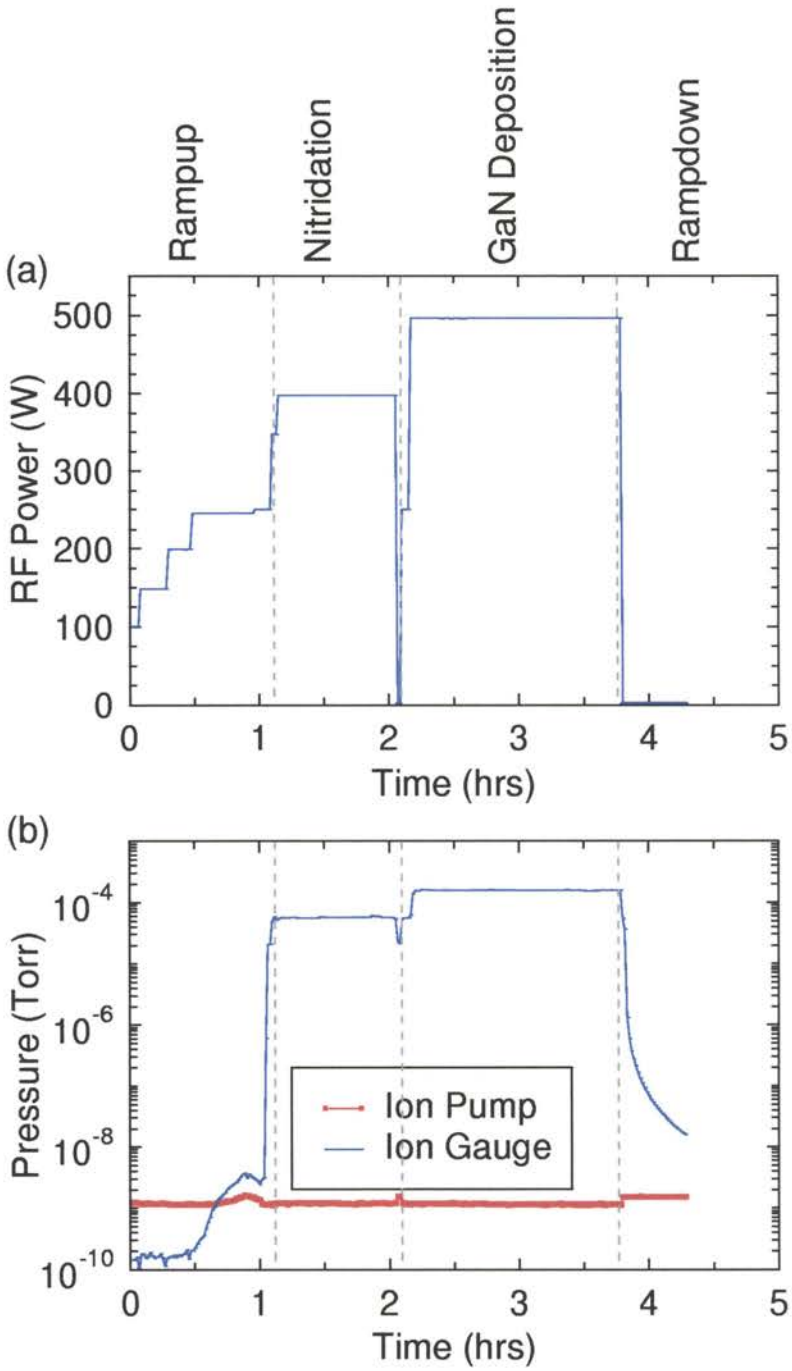

Figure 2.5. RF plasma operating conditions during a typical GaN epilayer deposition. Shown are (a) the RF forward power applied to the plasma source and (b) the chamber pressure (an indicator of N_2 flow rate) each versus the time into the growth experiment. The major steps of the growth experiment are indicated above the figure.

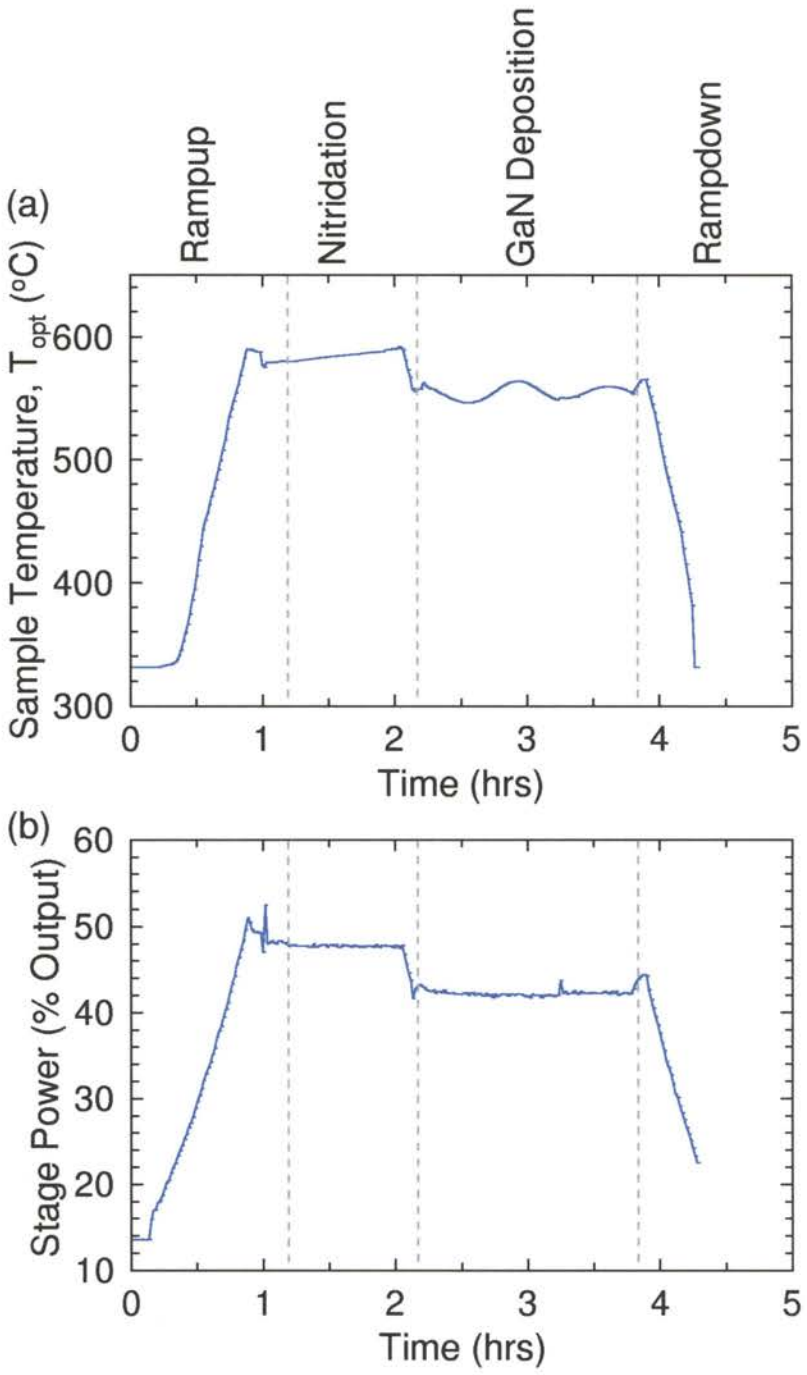

Figure 2.6. Profile of wafer heater operating conditions during a GaN growth experiment. Presented are (a) the wafer temperature as measured by the optical pyrometer and (b) the power applied to the heater expressed as a percentage of the maximum voltage the power supply can provide. The major steps of the growth experiment are indicated above the figure.

been used in the growth of GaN epitaxial films: (1) nitrided AlN layers and (2) low temperature GaN buffers.

As mentioned earlier, the AlN buffer layer is not deposited but rather is formed by exposing the Al_2O_3 surface to the N* plasma. The surface nitridation is usually performed at a high substrate temperature so that the damage to the surface by the plasma is minimized through simultaneous annealing. During the surface nitridation, the RHEED patterns are observed to gradually evolve from the Al_2O_3 $3\times$ surface reconstruction to an AlN $1\times$ surface reconstruction. It is observed experimentally that this transition is effectively complete after approximately 30–40 min of exposure to the standard RF plasma condition used for surface nitridation (400 W forward RF power and 2.0×10^{-5} Torr chamber pressure).

RHEED observations also reveal an interesting epitaxial relationship between the Al_2O_3 substrate and the AlN nitrided layer. This epitaxial relationship is as follows: AlN [0001] || Al_2O_3 [0001], AlN $[10\bar{1}0]$ || Al_2O_3 $[2\bar{1}\bar{1}0]$, and AlN $[2\bar{1}\bar{1}0]$ || Al_2O_3 $[1\bar{1}00]$. Stated more simply, the AlN unit cell is rotated 30° about the c-axis with respect to the Al_2O_3 unit cell. It is widely accepted that this rotation occurs to reduce strain in the AlN layer due to the large lattice mismatch between AlN and Al_2O_3 ($a_{AlN} = 3.112$ Å, $a_{sapp} = 4.758$ Å).

A second interesting feature associated with the AlN buffer is the evolution of the growth mode when overgrowth with GaN is initiated (assuming appropriate GaN growth conditions). The deposited GaN may be either the low-temperature buffer or the GaN epitaxial layer directly. However, the rate of this evolution is dependent on the GaN growth rate; therefore, the evolution is more easily observed during the GaN epilayer growth. This evolution of the growth mode is revealed by RHEED images observed at the onset of overgrowth with GaN. Figure 2.7 on p. 51 presents these RHEED images and corresponding schematic representations of the surface. The RHEED images from the nitrided AlN layer are generally bright and streaky, but poorly focused due to charging effects on the insulating Al_2O_3 substrate. At the onset of GaN deposition, the patterns immediately become well focused and remain streaky. After a very short period of GaN deposition (depending on growth rate),

the RHEED patterns become spotty, suggesting a transition to a three-dimensional growth surface. Finally, the spots in the RHEED patterns gradually become elongated and merge into continuous streaks over a longer period of time.

A possible physical origin for the evolution of the growth mode is high strain in the deposited GaN. At the onset of growth, it appears the GaN is highly strained. Despite this, the initial growth is two-dimensional. However, after the GaN layer exceeds the critical thickness, it becomes energetically favorable for the GaN to relieve strain by forming into islands; thus, there is a a transition to a three-dimensional, islanded growth mode. With continued deposition, the islands coalesce to form a continuous layer, resulting again in a two-dimensional or Frank-van der Merwe growth mode.

As indicated earlier, GaN buffer layers grown at low temperatures were used in a number of the early GaN growth experiments. HRXRD results for GaN epilayers grown on low temperature GaN buffers provide useful insight as to the effects of these buffers. GaN epilayers were routinely characterized using HRXRD measurements. A typical set of HRXRD curves are shown in Fig. 2.8 on p. 52. The symmetric ω-2θ and rocking curve scans presented are taken about the GaN (0002) reflection. As discussed in Chapter 1, these HRXRD measurements provide a measure of the crystalline quality of the epitaxial film. The full width at half maximum (FWHM) of the peak in each HRXRD scan can be treated as a figure of merit in quantitatively assessing different aspects of the crystallographic quality of an epilayer. The FWHM of the rocking curve peak measures the mosaic tilt present in the epilayer and is the most commonly reported HRXRD measurement.

HRXRD measurements have been used to assess the effect of the GaN buffer temperature on the crystallographic quality of the GaN epilayer. A series of GaN epitaxial samples were grown in which the buffer temperature was varied over the range 480–730 °C while all other growth parameters were held constant. A plot of the observed FWHM for the GaN (0002) diffraction peaks versus the GaN buffer temperature is presented in Fig. 2.9 on p. 54. The FWHM values for the GaN epilayers are observed to sharply decrease as the growth temperature for the GaN buffer is

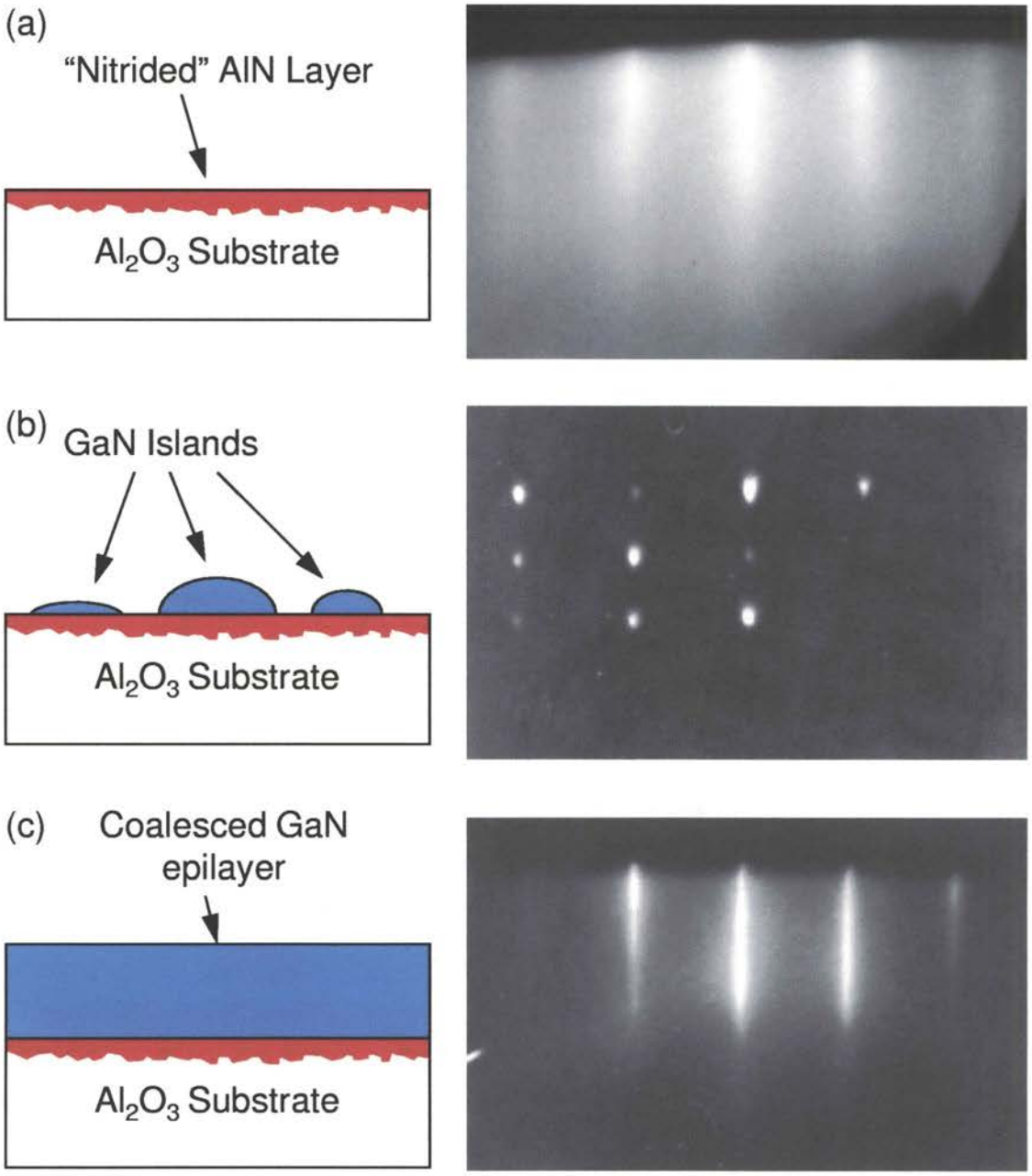

Figure 2.7. Evolution of RHEED patterns at the onset of GaN overgrowth on the nitrided AlN layer. RHEED images observed at the onset of GaN overgrowth are presented along with models representing the growth surface. RHEED images were observed along the $[11\bar{2}0]$ azimuth. (a) Presented is the AlN RHEED pattern observed after nitriding the Al_2O_3 surface. At the onset of GaN deposition, the growth mode is (b) three-dimensional after the layer thickness exceeds the critical thickness, and finally evolves to (c) a two-dimensional growth mode after coalescence of the islands.

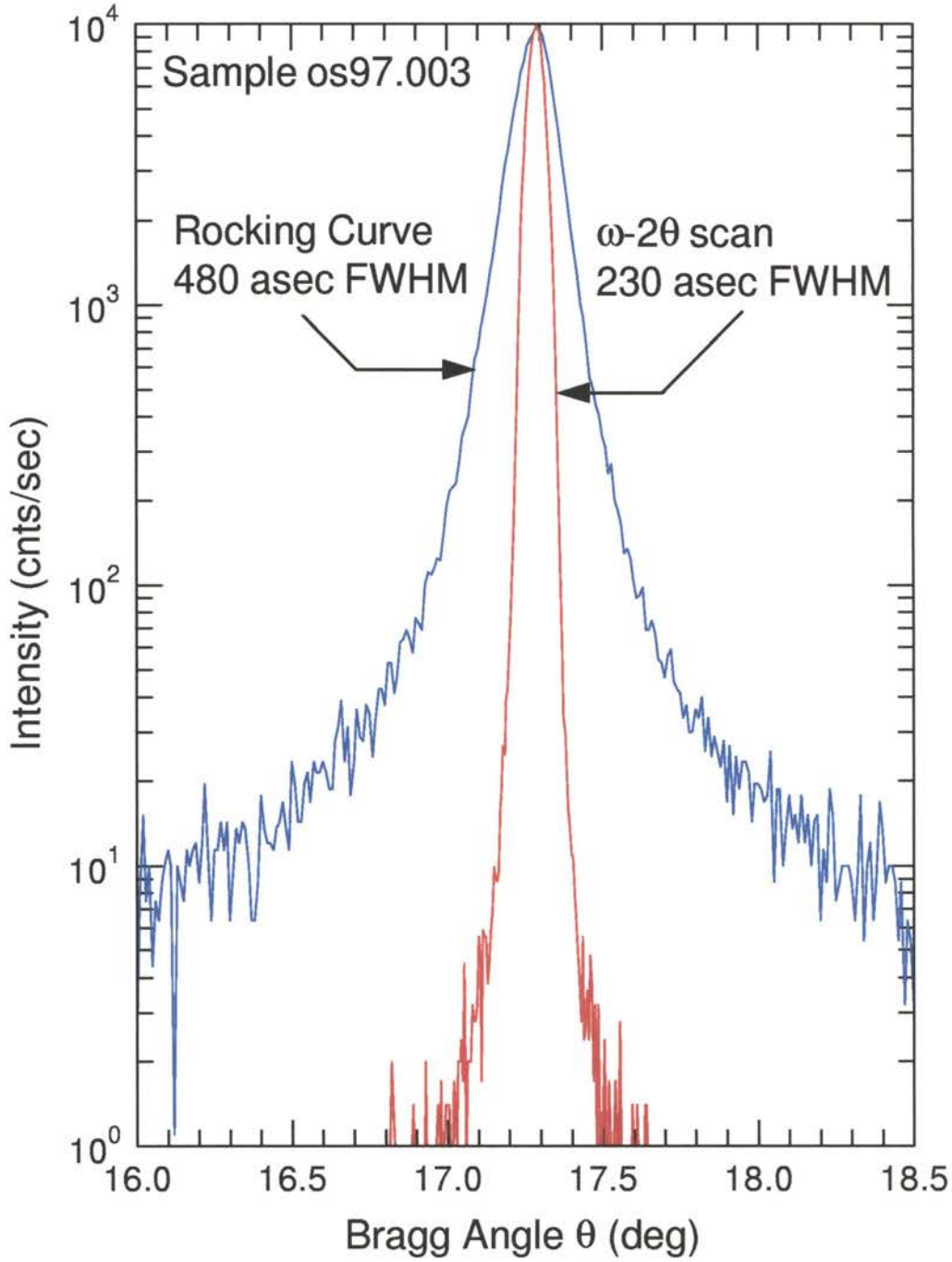

Figure 2.8. Typical ω-2θ and rocking curve scan data acquired from a GaN epilayer sample. HRXRD measurements are observed about the GaN (0002) reflection using Cu-Kα_1 radiation. The full width at half maximum (FWHM) of each peak is used as a figure of merit in assessing the crystallographic quality of GaN epitaxial samples.

increased. This is evidence that the quality of the GaN buffers is very poor at lower temperatures and that defect structures propagating from the buffer layer are significantly reducing the crystallographic quality of the GaN epilayer. Furthermore, it is worth noting that the highest buffer growth temperature used in this series of samples was identical to the growth temperature of the GaN epilayer. These results suggested a further growth experiment in which the GaN epilayer was deposited directly on the nitrided AlN layer. HRXRD results from this experiment indicated that the GaN epilayer grown directly on the nitrided AlN layer was in no way inferior to samples grown with low-temperature buffers. Consequently, the use of low-temperature GaN buffers was abandoned and all subsequent growth experiments were grown using the sample structure shown in Fig. 2.3(b).

2.3.2 Growth Parameters

While buffer layers affect the quality of epitaxial films, the growth conditions during growth of a GaN epilayer are far more important in determining the quality of the epilayer. In this section, the effects of the most important growth parameters on the growth of GaN epitaxial films and the resultant quality of these films will be discussed. Much like the growth of other III-V materials, the most important growth parameters have been found to be the (1) growth rate, (2) incident N*/Ga flux ratio, and (3) substrate temperature.

2.3.2.1 Growth Rate. The growth rate is known to be a key growth parameter in the deposition of any material grown by MBE. In many material systems, growth rates can be measured *in situ* through the observation of RHEED oscillations. Unfortunately, RHEED oscillations are only observed during GaN deposition at growth conditions that are non-optimal.[42,43] Consequently, alternative methods are needed to determine the growth rates during deposition of GaN epilayers. Two independent experimental measurements have been used to determine the GaN growth rates. The first method, based on spatially-resolved reflectance measurements, allows direct measurement of the epilayer thickness. Since the deposition time is known

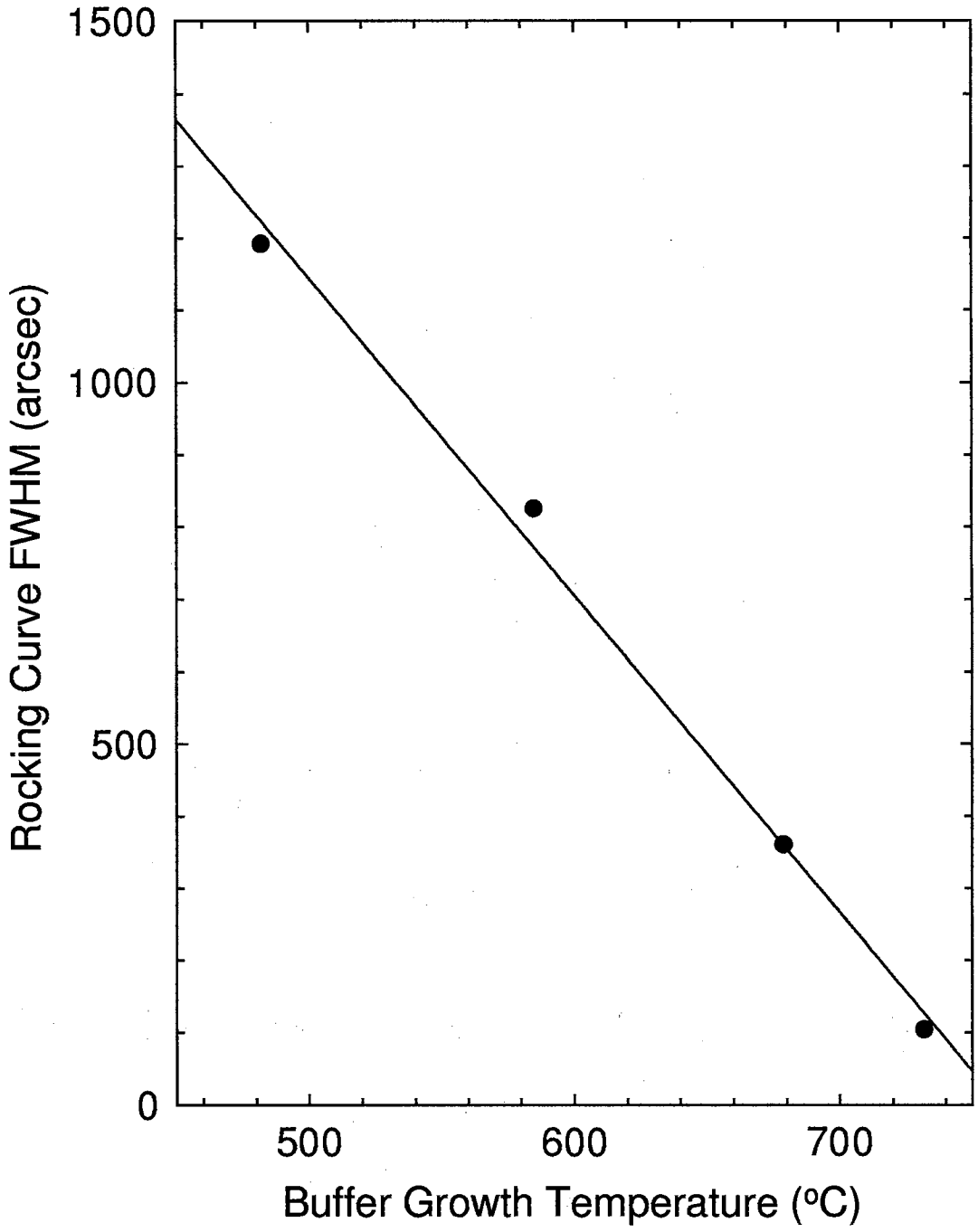

Figure 2.9. Effect of GaN buffer temperature on the full width at half maximum (FWHM) of the GaN (0002) main-layer rocking curve peak. The sharp decrease in FWHM of the rocking curve peaks indicates a dramatic improvement in the crystallographic quality of the GaN main layers with increasing GaN buffer temperature.

from the growth experiment, the growth rate may be calculated. The second method relies on oscillations observed in the optical pyrometer reading due to thin-film interference effects. This measurement gives the growth rate directly in real time during the growth experiment.

A typical set of data acquired using the spatially-resolved reflectance measurements is presented in Fig. 2.10 on p. 56. The details of this experiment are discussed in Appendix A. As will be discussed shortly, fringes can be observed with the naked eye on the surface of specular GaN epilayer samples due to variations in the film thickness across the wafer. Since the experiment yields spatially-resolved data, the film thickness may be measured at a number of points across the wafer surface. This allows the effect of small variations in the incident Ga and N* fluxes on the film thickness and growth rate to be ascertained. In the data presented in Fig. 2.10, the film thickness is determined at three points on the wafer surface. These thicknesses are (a) 1.18 μm, (b) 1.09 μm, and (c) 0.92 μm. As will be discussed shortly, the variations in thickness of this film are due to the variation in the N* flux across the wafer surface.

The second method of determining GaN growth rates utilizes oscillations in the optical pyrometer reading observed during the deposition of a GaN epilayer. The optical pyrometer estimates the sample temperature by monitoring the intensity of a single wavelength of light. As the GaN epilayer thickness increases during deposition, the intensity of this wavelength of light varies (nearly) sinusoidally due to thin film interference effects. By observing the rate at which these oscillations occur, it is possible to determine the GaN growth rate. This is illustrated in Fig. 2.11 on p. 57. As shown in the figure, a simple fitting of the oscillations in the optical pyrometer reading directly yields a real-time measurement of the GaN growth rate.*

These measurement techniques have been used to study the effects of growth conditions on GaN epilayer growth. It is interesting to consider the effect of the

*It is worth noting that growth rates determined by this method are typically 10% smaller than the growth rate determined by performing reflectance measurements at the center of the sample. Generally, the reflectance measurement is regarded as the more accurate of the two measurements since the optical pyrometer has a large sampling area and poor wavelength discrimination compared to the reflectance apparatus.

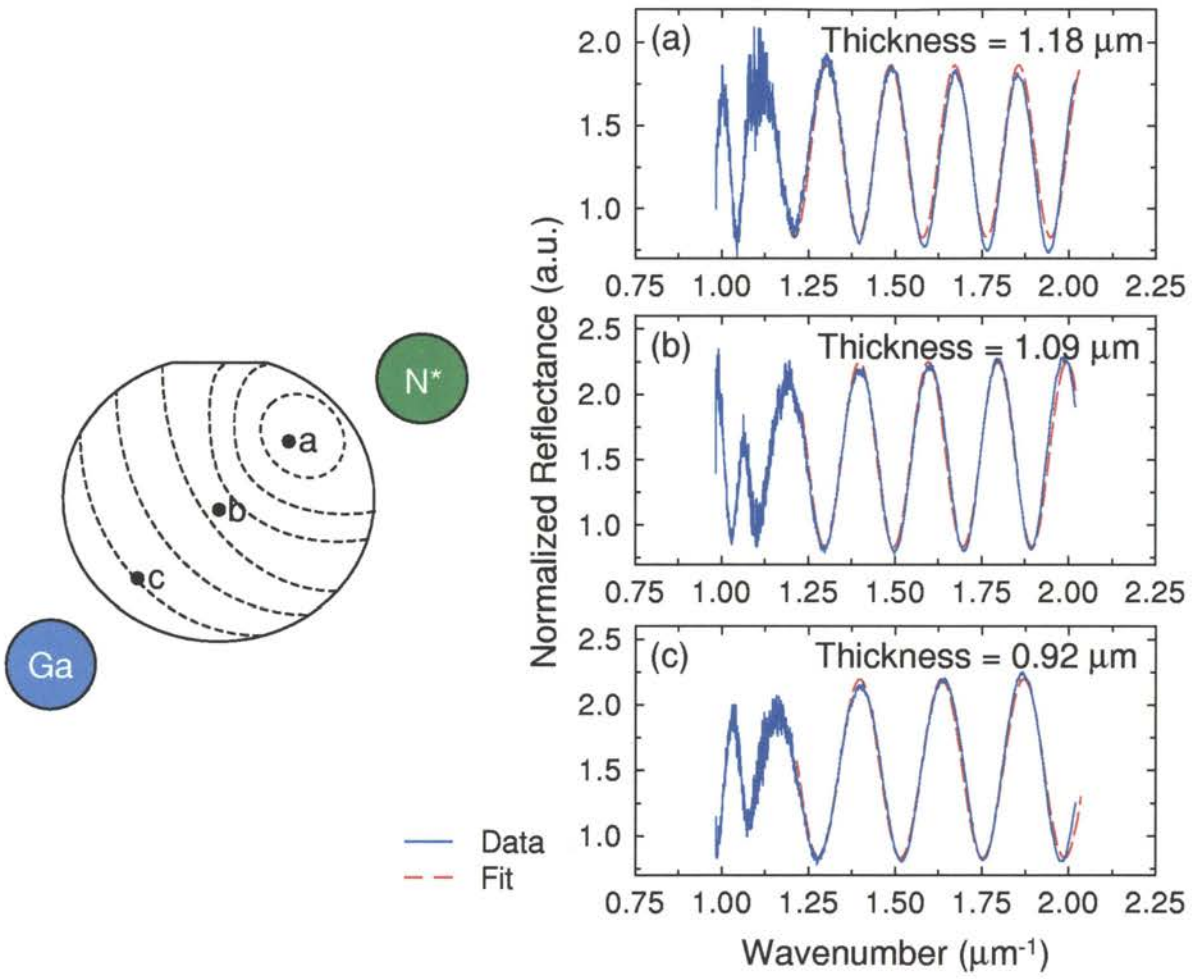

Figure 2.10. Spatially-resolved reflectance measurements for the determination of GaN epilayer thicknesses. Thickness fringe patterns are frequently observed for specular GaN epilayers. The film thickness is determined at numerous points across the wafer using spatially-resolved reflectance measurements. The film thicknesses at the points indicated on the wafer are found to be (a) 1.18 μm, (b) 1.09 μm, and (c) 0.92 μm.

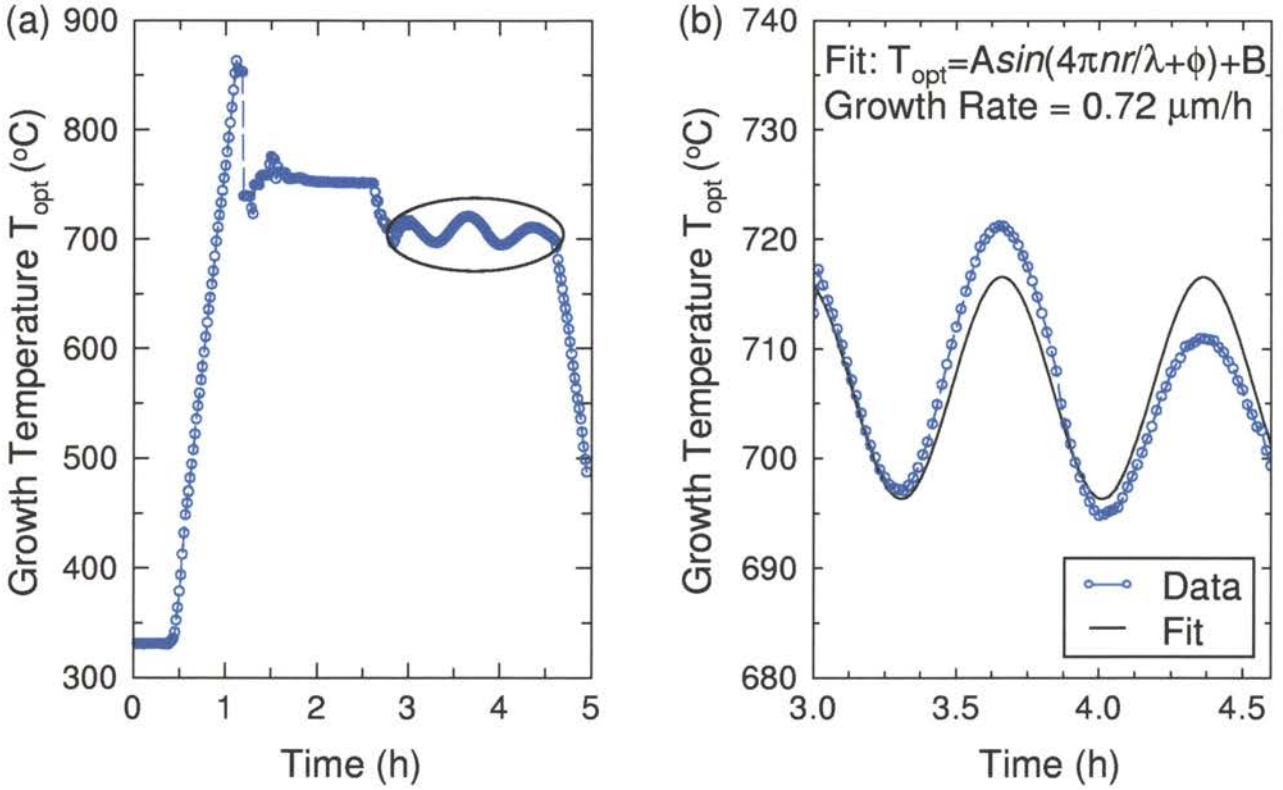

Figure 2.11. Determination of GaN growth rates using optical pyrometer readings. Oscillations in the optical pyrometer reading occur due to thin-film interference effects. The GaN growth rate may be determined by fitting the observed oscillations.

incident Ga flux on the GaN growth rate. In order to study this, a number of samples were grown in which the incident Ga flux during the GaN epilayer deposition was varied while all other growth parameters were held constant. For each sample, film thickness measurements were performed using the spatially-resolved reflectance measurement discussed earlier.

The results of these measurements are presented in Fig. 2.12 on p. 59. The figure shows an Arrhenius plot of the GaN growth rate at the center of the wafer as a function of the Ga cell temperature T_{Ga}. As T_{Ga} is increased from low temperatures, the GaN growth rate is observed to increase linearly on the Arrhenius plot. However, as T_{Ga} is increased further, the GaN growth rate is observed to saturate and remain nearly constant. A second series of GaN samples grown using a lower N* flux reveals qualitatively similar results. However, in this series of samples, the GaN growth saturates at a lower level. As is normally the case with effusion cells, calibration of the Ga flux against T_{Ga} performed using a quadrapole mass spectrometer reveals that the Ga flux is well described by a Boltzmann factor temperature dependency. This strongly suggests that below the saturation level, the GaN growth rate is limited by the rate at which Ga arrives at the growth surface; that is, the GaN growth is arrival-rate limited by the Ga flux. Additionally, the observation that the saturation level is dependent in the N* flux suggests that for higher Ga flux rates, the GaN growth is arrival-rate limited by the N* flux. Finally, it is reasonable to speculate that at the observed "knee" in the GaN growth curve shown in Fig. 2.12 the growth is stoichiometric; that is, the effective N* flux rate is equivalent to the incident Ga flux rate. Since it is very difficult to experimentally measure the flux from the plasma source, it is convenient to define the N*/Ga flux ratio to be 1 at the "knee" of the GaN growth rate curve.

Further support for this assessment of the GaN growth as being either Ga-limited or N-limited is obtained through visual inspection of the samples, inspection with an optical microscope, and through optical pyrometer observations. Samples grown with growth rates at or slightly above the knee of the curve are observed to be metallized on the edge nearest the Ga source. The size and extent of this

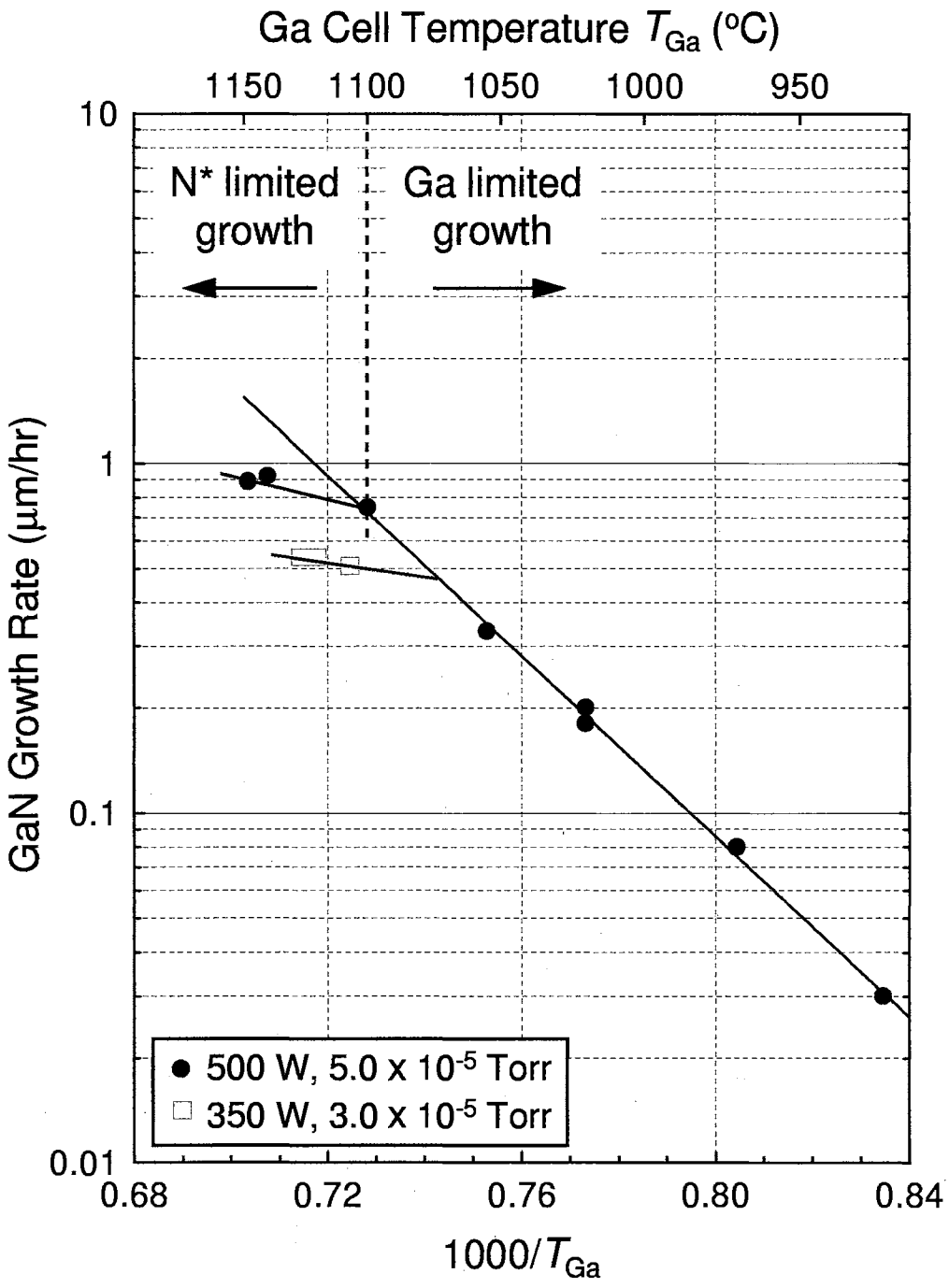

Figure 2.12. Arrhenius plot of the GaN growth rate versus Ga cell temperature. The GaN growth rate is observed to increase to a saturation level. Beyond this saturation level the GaN growth increases at a much lower rate. The saturation level is observed to be dependent on the N* flux rate. This suggests that GaN growth is Ga arrival-rate limited below the "knee" of the curve and N* arrival-rate limited above the "knee" of the curve.

metallized region is observed to increase for samples in which the Ga flux rate is increased further. Inspection of the samples under a microscope reveals a gradual transition from the specular to the metallized regions of the samples. In the specular region, small Ga droplets can be observed on the surface. The size of these droplets increases as one moves towards the metallized region of the sample. Finally, the drops are observed to coalesce into a continuous Ga metal layer. These observations suggests that the rate at which Ga is deposited on the surface exceeds the rate at which Ga can be consumed through GaN growth, eventually resulting in a metallized surface. Additionally, under N-limited growth conditions, the temperature of the surface as measured by the optical pyrometer is observed to decrease despite the heater power remaining constant. This suggests that as the surface becomes metallized, the emissivity of the surface decreases, resulting in an underestimation of the temperature by the optical pyrometer.

Lastly, the visual appearance of GaN epilayer samples suggests that the GaN growth rate varies across the wafer surface. When GaN epilayers are grown under conditions that result in a specular surface, distinct color fringes are observed across the surface. These fringes are typically arcs that appear to be centered on a point. Depending on the incident fluxes, this point may appear on the wafer, or off the wafer towards either the Ga cell or the N* sources. A schematic example of these fringes is shown in Fig. 2.10. The center of these fringes is observed to move towards the N* source under high Ga fluxes and towards the Ga source under low Ga fluxes. Spatially-resolved reflectance measurements provide further insight into the physical origin of this point and the color fringes. Spatially-resolved reflectance measurements indicate that GaN epilayers are thickest at the point on which these fringes are centered, and thinner away from this point toward either flux source. If the center of the fringes does not appear on the wafer, then the wafer is thickest on the edge nearest the center of the fringes. These observations suggest that the color fringes are due to the spatial variations in the Ga and N* fluxes across the wafer surface. It appears, the GaN growth rate at any point on the wafer will be limited by the smaller of the two source fluxes. Thus, when the center of the fringes is at the center of the wafer, the GaN

growth rate on the edge nearest the Ga cell is limited by the N* flux. Likewise, the GaN growth rate on the edge of the wafer nearest the N* source is Ga arrival-rate limited. Lastly, the center of the fringes can be interpreted as the point where the Ga and N* fluxes are equal.

2.3.2.2 N*/Ga Flux Ratio. In addition to the variations in the GaN growth rates observed in the samples discussed in the previous section, other interesting effects are observed in RHEED patterns during growth. However, it should be noted that RHEED patterns are a function of the surface composition and the surface morphology, and are only *indirectly* influenced by the fluxes incident on the growth surface. However, as the surface composition is strongly influenced by the incident fluxes, the RHEED patterns observed may be regarded as being a function of the incident N*/Ga flux ratio.

The RHEED patterns during GaN deposition are observed to be strongly affected by the incident N*/Ga flux ratio. First, the RHEED patterns observed during GaN growth are dominated by (1×1) surface reconstructions. Higher order diffraction lines are not observed on surfaces free of contamination. In addition to the normal streaks, spots and chevron features are also observed in the RHEED images under varying growth conditions. The effect of the N*/Ga flux ratio on the RHEED images observed during GaN growth are summarized in Fig. 2.13 on p. 63. As shown in the figure, for GaN growth rates that are lower than the knee of the curve, that is the N*/Ga flux ratio is greater than 1, the RHEED patterns have either spots or chevron-like facet features depending of the substrate temperature (this will be discussed later). At higher GaN growth rates (N*/Ga flux ratio approaching 1 from above), the RHEED patterns become more streaky, indicating an improved surface morphology. The RHEED patterns become smooth, continuous streaks at the knee of the curve (where the N*/Ga is *defined* to be 1). At GaN growth rates higher than the knee of the curve (N*/Ga flux ratio less than 1), there is no change in the features of the RHEED patterns; however, the intensity of the RHEED patterns begins

to decrease. The RHEED pattern intensity is observed to decrease more rapidly at higher Ga flux rates.

The RHEED observations described above suggest a number of things about the growth of GaN epilayers. First, the observation that the RHEED pattern intensity decreases when the N*/Ga flux ratio is less than 1 is in good agreement with the observation that the surface becomes metallized in the N*-limited growth regime. Accumulated metal on the growth surface would prevent diffraction of the RHEED beam by the underlying crystal surface, resulting in a decreased pattern intensity. Additionally, the observation that the RHEED patterns are streaky at the knee of the curve suggests that growth is occurring on an atomically flat surface. The observation of either spotty or faceted RHEED patterns at N*/Ga flux ratios greater than 1 are more typical of three-dimensional diffraction, suggesting the surface is roughening under these growth conditions.

The results above appear to imply that under N-rich growth conditions GaN prefers to grow in a three-dimensional growth mode. While this result is very different from other III-V materials such as GaAs, it is not unprecedented. It is well known that in the growth of zincblende GaN under N*-rich flux conditions the growth can proceed in directions other than the (001) direction.[44–46]

Further effects of the N*/Ga flux ratio are observed in spatially resolved HRXRD results. Using the automated capabilities of the HRXRD system, it is possible to acquire HRXRD scans from a large number of points on the wafer surface. An example of spatially-resolved HRXRD data is presented in Fig. 2.14 on p. 65. Rocking curve measurements have been performed near the GaN (0002) diffraction peak in a square matrix centered on the wafer in 5 mm steps. After determining the FWHM of the GaN (0002) peak in each scan, a false-color map of the rocking curve FWHM values (shown in Fig. 2.14) can be generated. Smaller values for the rocking curve FWHM occur on the portion of the sample nearest the N* plasma source. Correlating this result with the spatially-resolved reflectance measurements indicates that the smallest rocking curve FWHM values occur where the epilayer is thickest.

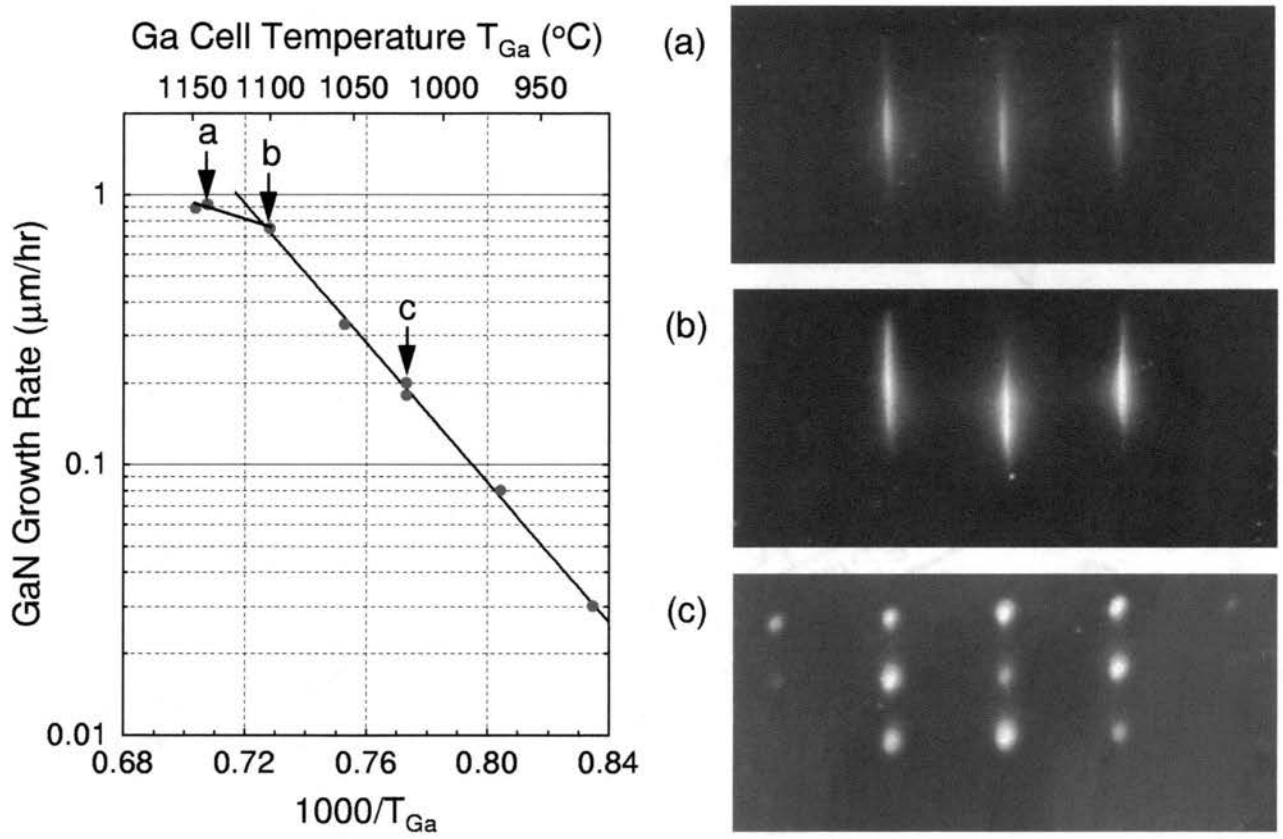

Figure 2.13. RHEED patterns observed under different N*/Ga flux ratios. RHEED patterns are observed to be (a) streaky, but weak and fading under Ga-rich flux conditions, (b) streaky under stoichiometric flux conditions, and (c) either spotty or faceted under N*-rich flux conditions.

Importantly, this result is not specific to this sample; this result is consistently observed in GaN epilayers. Due to the geometry of the flux sources, the highest GaN growth rate will occur at the point of the where the incident N*/Ga flux ratio is equal to 1 (or closest to 1). This then implies that the best crystallographic material quality is obtained when the N*/Ga flux ratio is equal to 1.

2.3.2.3 Substrate Temperature. It is known from the MBE growth of other materials that the substrate temperature T_{sub} during epilayer deposition is a critical growth parameter. In the growth of GaN epilayers, the importance of the substrate temperature is revealed by RHEED images observed during epilayer deposition. Examples of RHEED images observed under stoichiometric flux conditions and at several substrate temperatures are shown in Fig. 2.15 on p. 66. At low growth temperatures under stoichiometric flux conditions, the RHEED patterns are observed to be spotty and diffuse. If growth is continued under such conditions, the RHEED patterns become successively dimmer. At high growth temperatures, the RHEED patterns generally remain streaky but develop additional features. At successively higher substrate temperatures, the patterns first develop sharp point features which then extend into sharp well-formed chevrons or facet features. Again, prolonged growth under such conditions results in RHEED patterns which eventually fade. Samples grown at moderately high temperatures typically have a slightly hazy, specular appearance. Samples grown at very high temperatures appear very rough and non-specular. Lastly, at temperatures between these extremes, deposition may be continued without degradation of the specular RHEED patterns.

Additionally, RHEED patterns observed under N-rich growth conditions are worthy of consideration. It was alluded to in Section 2.3.2.2 that a temperature dependence is observed for RHEED patterns viewed under N-rich growth conditions. Under N*-rich flux conditions and at low substrate temperatures, the RHEED images reveal poorly formed chevron-like facet features in which the interior is completely illuminated. At successively higher substrate temperatures, the facet features become sharper and more well defined and evolve into a finite set of lines or rays at distinct

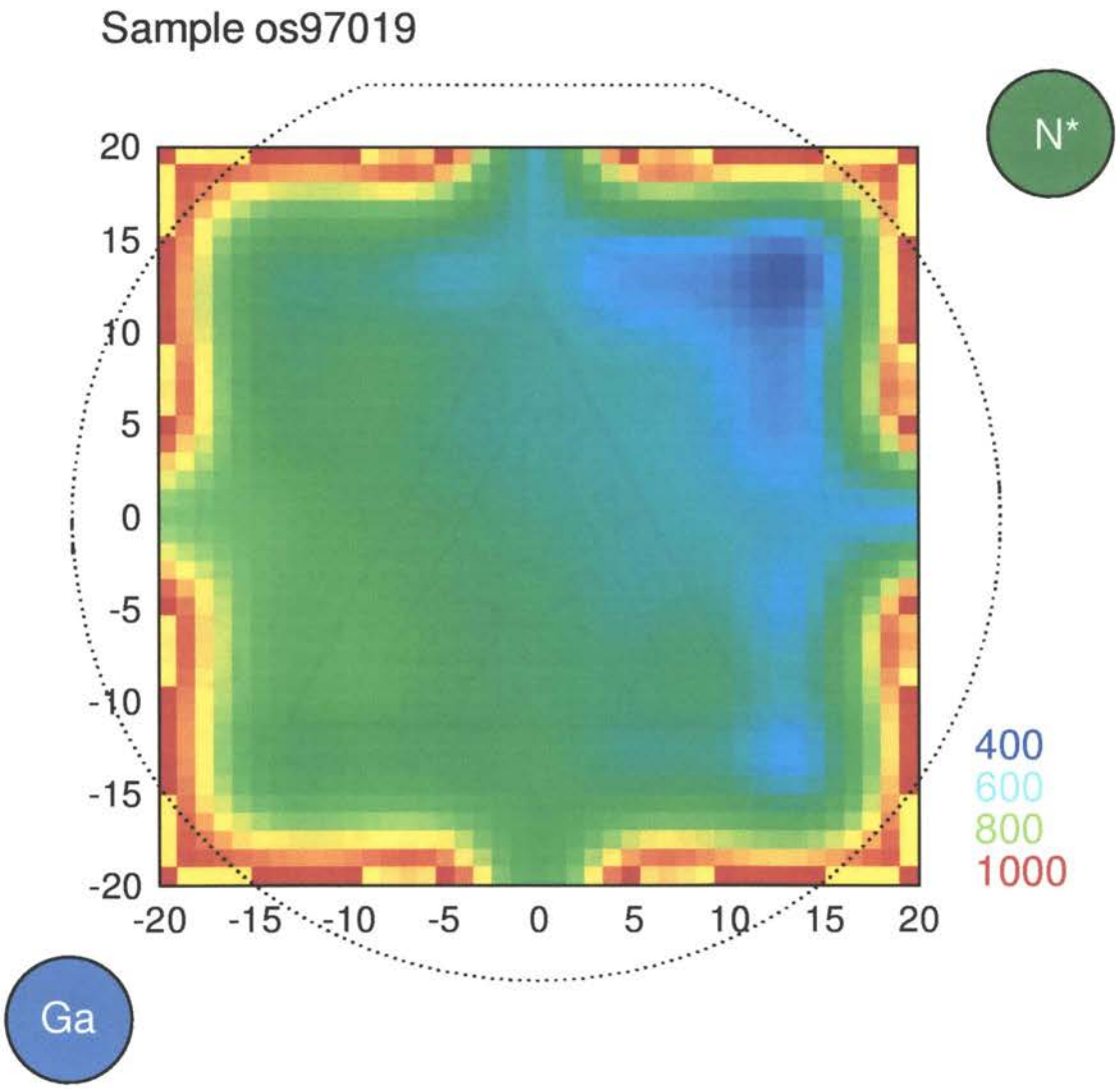

Figure 2.14. False-color map representing the full width at half maximum (FWHM) value for the GaN (0002) rocking curve peak as a function of position on the wafer. FWHM values are expressed in arcsec. and positions are expressed in millimeters. Rocking curve scans are acquired for a matrix of points on the wafer surface. The false-color map is generated by interpolating the FWHM values from the rocking curve scans.

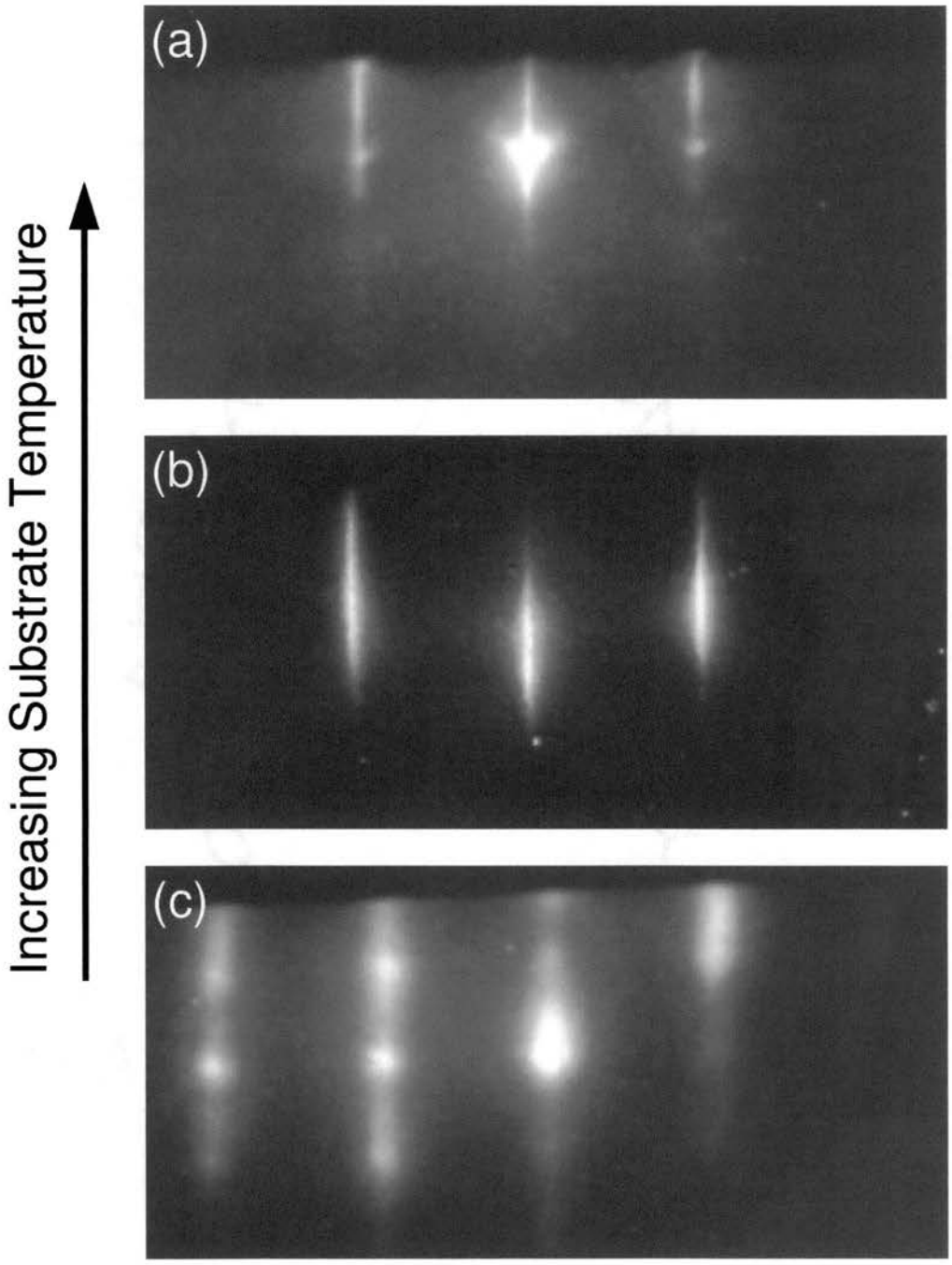

Figure 2.15. Effect of substrate temperature on RHEED patterns under stoichiometric flux condition. RHEED patterns viewed along the $[11\bar{2}0]$ azimuth are (a) specular with superimposed sharp chevron features at high substrate temperature, (b) specular at moderate substrate temperatures, and (c) spotty and diffuse at low substrate temperatures.

angles within the interior of the facet feature. Finally, at very high temperatures, only a single well defined line or ray is observed on each side of the facet feature. The evolution of these facet features is illustrated in Fig. 2.16(a) on p. 68. An example of a highly faceted RHEED pattern is presented in Fig. 2.16(b). Lastly, atomic force micrographs are shown in Fig. 2.16(c) and (d) for a GaN epilayer that was grown under similar conditions and deposited directly on the nitrided AlN layer. These micrographs provide some insight into the physical origin of the highly faceted RHEED images. As can been seen in the figure, the GaN does not form a smooth, continuous layer under these growth conditions; instead small, hexagonal pyramids are observed. The planes forming the hexagonal pyramids, which are angled with respect to the growth surface, allow diffraction streaks to appear at an angle relative to the normal streak direction. The fact that a constructive interference condition is satisfied and facet features can be observed in the RHEED patterns is clear evidence that these hexagonal pyramids are crystalline in nature and crystallographically oriented on the surface.

2.3.2.4 Summary of Growth Parameter Effects: Growth Model. In the previous sections, the effects of growth parameters on a number of aspects of GaN epilayer growth have been discussed. Particular attention has been given to the effects of these growth parameters on experimentally observed RHEED patterns, growth rates, crystallographic qualities, and surface morphologies. However, it is very important to understand how the growth parameters influence physical processes at the growth surface to yield the results that have been observed. Stated another way, it is important to understand how the macroscopic growth parameters (substrate temperature, N*/Ga flux ratio, and Ga flux), which can be controlled in the growth chamber, influence the relevant microscopic growth processes occurring on the surface during GaN deposition. As will be shown in the following discussion, it is only necessary to understand the effects of the growth parameters on a small number of microscopic processes to understand the growth phenomena that have been observed.

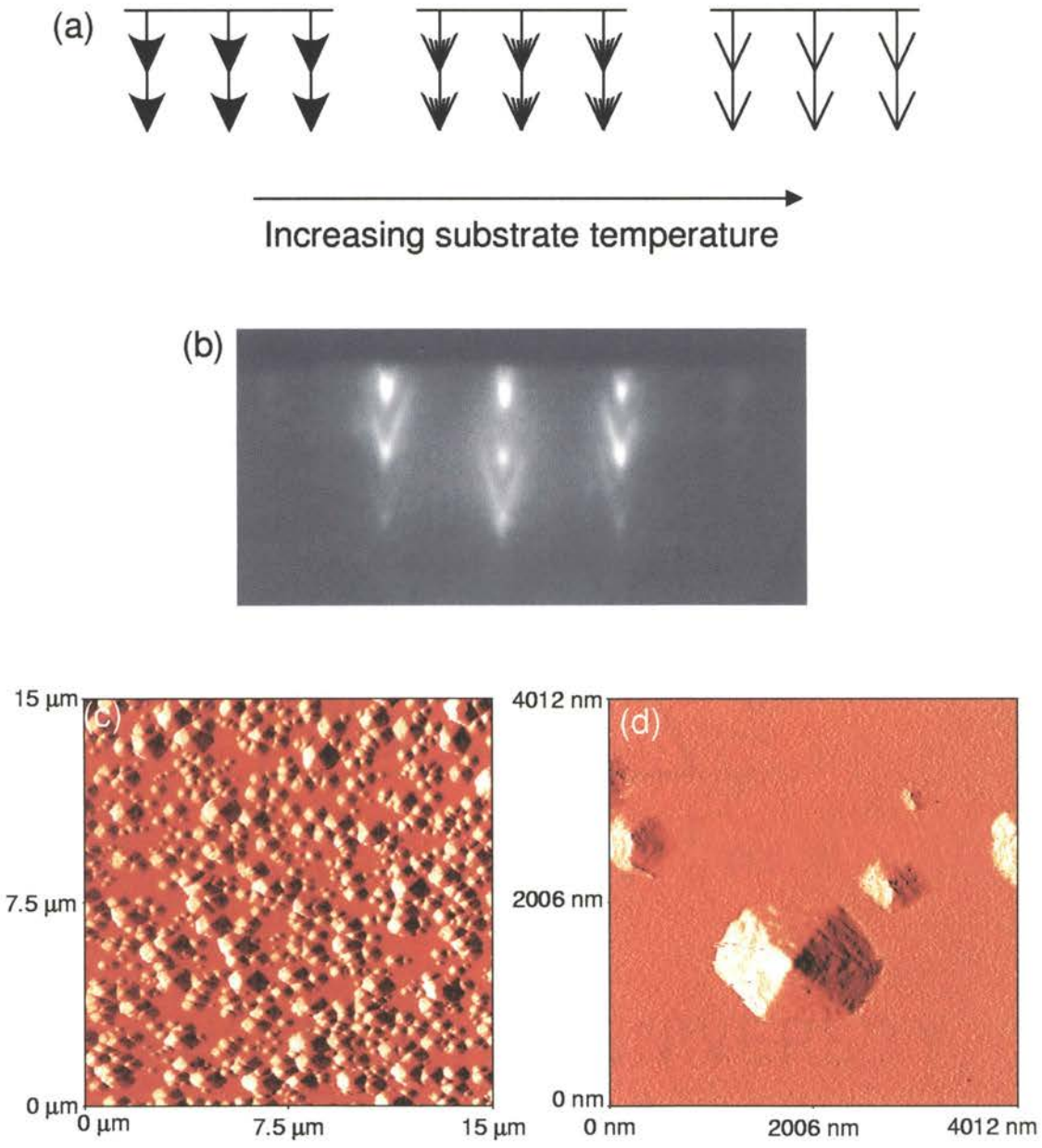

Figure 2.16. Surface features resulting in chevron patterns in RHEED images. Presented are (a) a schematic representation of the temperature dependent variations of the chevron features observed in RHEED images at high substrate temperatures and N*-rich flux conditions, (b) a typical RHEED image observed under such growth conditions, and (c) and (d) atomic force micrographs of GaN hexagonal pyramids formed during deposition of a nominally 300 Å buffer layer grown directly on a nitrided AlN layer under similar growth conditions.

Firstly, in MBE growth, one of the most important microscopic processes is (lateral) migration of deposited species on the growth surface. It is the ability of deposited atoms to migrate on the growth surface, so as to sample a large number of configurational states to find the minimum energy configuration, that allows MBE grown materials to be of high quality. Now, consider the effects of the N*/Ga flux ratio on the migration of materials deposited on the growth surface. It is normally the case in the molecular beam epitaxial growth of III-V semiconductors, that the column V metals are more mobile on the growth surface than the column III materials.* This should also be expected in the case of GaN growth; bonds involving N atoms are generally stronger (of higher energy) than bonds involving Ga atoms. Therefore, deposited atoms should have higher migration rates on surfaces that are more rich in Ga. Additionally, it is reasonable to expect the incident N*/Ga flux ratio to strongly influence the surface composition, that is, the relative surface concentrations of N and Ga. Consequently, the incident N*/Ga flux ratio should affect the migration rates of atoms deposited on the growth surface.

Secondly, the substrate temperature strongly influences several thermally activated processes at the growth surface. Of particular importance are the migration of atoms on the surface and the desorption of atoms from the surface. It is physically reasonable to expect that as the substrate temperature is increased, the mean migration rate of atoms on the surface will increase. Additionally, desorption of deposited materials from the MBE growth surface, which is observed in many material systems, should increase at higher substrate temperatures.

Thirdly, the GaN growth rate effectively limits the mean migration time of atoms deposited on the growth surface. An adatom on the growth surface is forced to incorporate when overgrown by the material that is continuously being deposited. The mean migration time must then be directly proportional to the monolayer deposition time and inversely proportional to the GaN growth rate. Consequently, the mean

*This is commonly exploited in a process called Migration Enhanced Epitaxy (MEE). In this technique, the column V flux is periodically interrupted during deposition to enhance the migration rate of the column III metals, resulting in an improved material quality.

migration time of atoms deposited on the surface is strongly affected by the Ga flux rate under N*-limited growth conditions and by the N* flux rate under Ga-limited growth conditions.

Finally, the RHEED and AFM results presented earlier indicate that under N*-rich flux conditions or high substrate temperatures (relative to the growth rate), the GaN growth mode favors the formation of a three-dimensional surface. This suggests that under these growth conditions, planes tilted with respect to the normal (0001) growth plane have a lower surface free energy than the (0001) growth plane. Hence, GaN growth prefers to occur perpendicular to these tilted planes. It is worth noting that N-rich surface concentrations appear to aggravate this three-dimensional growth more than high substrate temperatures. There are a number of possible physical explanations for the observed three-dimensional growth mode. Firstly, the presence of excess N atoms may be altering the physical chemistry of the surface. Secondly, the tilted planes may be more robust against damage from the active plasma. Lastly, under N-rich growth conditions, the growth may simply occur along a plane in which the number densities of N and Ga atoms are closer to the surface concentrations of N and Ga.

Substantial support for the assessment of the microscopic growth processes presented above is provided by agreement with the GaN growth phenomenology presented earlier. Firstly, consider the RHEED patterns observed as a function of the N*/Ga flux ratio (shown in Fig. 2.13). The faceted to streaky RHEED transition may now be understood to be a consequence of lowering the surface concentration of N, thereby reducing the tendency of the surface to grow three-dimensionally.

Secondly, the phenomenology associated with metallization of surfaces under Ga-rich growth conditions may also be understood in terms of microscopic growth processes. For a surface with a high Ga concentration, the mean migration length will be long. When the mean migration length is long, Ga atoms are able to migrate into clusters and form droplets. For portions of the sample closer to the Ga source this effect is exaggerated; the surfaces are more Ga-rich allowing the droplets to increase in size eventually forming a continuous sheet.

Thirdly, these microscopic growth processes can be used to explain the temperature dependence of the RHEED patterns observed under stoichiometric flux conditions (presented in Fig. 2.15). At low substrate temperatures, spotty and diffuse RHEED patterns are observed. These RHEED patterns appear to be a consequence of the low migration rate of surface adatoms expected at low substrate temperatures. Since the migration rate is too low, the atoms on the surface are not able to find the lowest energy configuration before being overgrown. Consequently, the growth becomes frustrated since the rate of crystal formation cannot proceed at the rate material is deposited on the surface. Additionally, the faceted RHEED patterns observed at high substrate temperatures can be explained in terms of these microscopic growth processes. Two possible effects appear to contribute to the surface roughening. Firstly, a non-negligible fraction of the surface Ga may desorb at high substrate temperatures, resulting in a N*-rich surface which is conducive to a three-dimensional growth mode. Secondly, at high substrate temperatures, the mean migration length becomes large and surface adatoms have sufficient thermal energy to segregate over step edges. This allows surface adatoms to migrate to sites where three dimensional growth along planes tilted with respect to the normal growth direction is occurring. Finally, microscopic growth processes may be used to explain the specular RHEED patterns observed at moderate substrate temperatures. Under these conditions, surface adatoms will have moderate mean migration lengths. A surface adatom should then be able to migrate at a sufficient rate to incorporate at a site which provides a local minimum, rather than an absolute minimum, in the surface free energy. That is, these atoms incorporate on the normal (0001) growth planes rather than on planes angled with respect to this surface. In this way, the growth parameters are used to control the growth kinetics to force growth to occur along the (0001) direction.

Finally, the temperature dependence of the RHEED patterns observed under N-rich growth conditions (presented in Fig. 2.16) may be explained using these microscopic growth processes. Consider growth at stoichiometric flux conditions and a moderate substrate temperature; sharp, streaky RHEED patterns should be observed. If the Ga flux were reduced, the surface composition would become N-rich.

Under these conditions, growth would prefer to occur on planes angled with respect to the normal (0001) growth plane. However, the mean migration lengths of the surface adatoms would also be reduced under these growth conditions. Under these conditions, it is plausible that the surface adatoms may incorporate on any of a number of planes for which the surface free energy is lower than the (0001) growth plane. Consequently, the interior of the chevron feature appears filled since diffraction occurs from a large number of planes each with a slightly different angle with respect to the normal (0001) growth plane. Since the migration length increases as the temperature is increased, surface adatoms become biased to incorporate only on the planes with the lowest surface free energies. Consequently, sharp diffraction lines are observed in the chevron features for only a small family of planes. Lastly, at high substrate temperatures, the atoms on the surface have a sufficiently high migration rate to ensure incorporation only along the plane with the minimum surface free energy. Consequently, a single, sharp diffraction line or ray is observed on each side of the chevron features.

It is useful to summarize the temperature dependence of GaN growth in a single figure. This provides a useful tool for expeditiously understanding and adjusting growth conditions in real-time during growth experiments. From the discussion above, it should be evident that for a given substrate temperature, there is a maximum growth rate $r_{\max} = r_{\max}(T_{\text{sub}})$ above which normal GaN growth can occur. That is, $r_{\max}$ is the maximum rate at which the crystal can form due to thermodynamic and kinetic limitations. An Arrhenius plot of $r_{\max}$ as a function of the substrate temperature is presented in Fig. 2.17 on p. 74. The $r_{\max}$ curve was extrapolated from data points obtained by using RHEED patterns to determine the minimum temperatures at which specific GaN growth rates could be sustained. The curves on either side of the $r_{\max}$ curve represent the estimated error in $r_{\max}$. The GaN growth rate r is observed to be optimal when $r \lesssim r_{\max}$. That is, when r is just below the $r_{\max}$ curve. For a GaN growth rate larger than $r_{\max}$, i.e. above the $r_{\max}$ curve, the growth becomes frustrated due to thermodynamics limitations. Continued growth at these conditions results in a metallized, polycrystalline surface. Lastly, for low GaN

growth rates ($r < r_{max}$), the RHEED patterns are observed to be faceted and become increasing faceted at successively lower growth rates.

2.4 Summary and Conclusions

GaN is a semiconductor with a direct bandgap of 3.4 eV at room temperature. Additionally, GaN and the related semiconductors InN and AlN are thermally stable, chemically inert, and mechanically robust. These properties make GaN highly desirable for potential use in light emitting diodes and laser diodes operating in the blue to UV portion of the electromagnetic spectrum, solar-blind optical sensors, and high temperature and high power electronics. Despite the numerous potential applications for GaN, techniques for growing viable GaN substrates have not yet been produced. Consequently, the preponderance of GaN is grown either by metal-organic chemical vapor deposition (MOCVD) or molecular beam epitaxy (MBE) on Al_2O_3 or SiC substrates. In this chapter, research of GaN growth on Al_2O_3 (0001) substrates by RF plasma assisted molecular beam epitaxy has been discussed. The relevant growth phenomenology has been identified and assessed through a number of characterization techniques including *in situ* reflection high energy electron diffraction (RHEED) and optical pyrometry, and *ex situ* spatially-resolved reflectance spectroscopy, high resolution X-ray diffraction (HRXRD), and atomic force microscopy.

The effects of two types of buffer layers were discussed. Firstly, AlN buffer layers formed by exposing the Al_2O_3 (0001) substrates to a N* plasma were observed to be suitable for subsequent overgrowth with GaN epilayers. Additionally, the use of GaN buffer layers grown at low substrate temperatures was investigated. It was found that the crystallographic quality of GaN epilayers deposited over these buffer layers was not improved. In fact, buffer layers grown at temperatures lower than the GaN epilayer growth temperature were found to be deleterious to the GaN epilayer.

A variety of GaN growth experiments revealed that the most important growth parameters for GaN growth are (1) the GaN growth rate, (2) the incident N*/Ga flux ratio, and (3) the substrate temperature during deposition. The effects of each of these growth parameters on the growth of GaN epilayers and the resultant quality

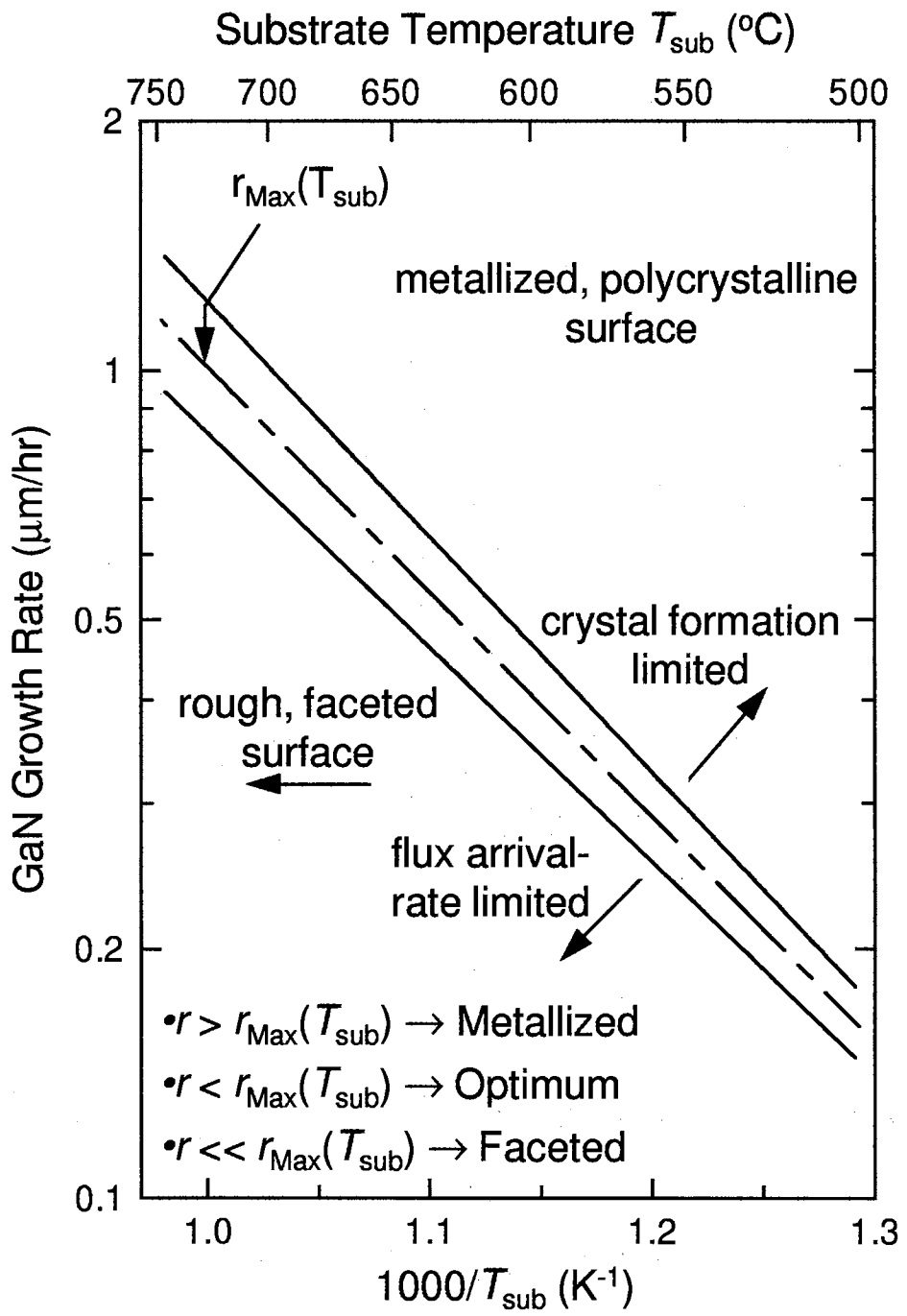

Figure 2.17. Temperature dependence of the maximum GaN growth rate. The maximum GaN growth rate $r_{max} = r_{max}(T_{sub})$ due to kinetic limitations is shown versus the substrate temperature. Lines on either side of r_{max} indicate the estimated error bar. GaN epilayers grown at a rate r are found to be metallized and polycrystalline for $r > r_{max}$, optimum for $r \lesssim r_{max}$, and faceted for $r \ll r_{max}$.

of these epilayers was discussed. Additionally, an interpretation of the effects of each of these growth parameters on the microscopic growth processes was presented. Importantly, all of the observed growth results could be understood in terms of the proposed microscopic growth processes.

Finally, the results of this research will have an impact of future work in this field. Through this work, a knowledge of the essential physics of GaN growth has been obtained. This knowledge is a prerequisite to being able to grow high quality GaN epitaxial layers for device applications. By understanding the effects of growth conditions of the microscopic growth processes, it is possible to estimate the adjustments needed in the growth conditions to be able to grow over a wide range of growth rates and substrate temperatures. Additionally, as will be shown in the next chapter, the growth of InGaN epilayers is very similar to that of GaN epilayers, and the understanding of the GaN growth that has been developed here will serve as a foundation for understanding InGaN growth. Lastly, it may be possible, in future work, to generalize the understanding of GaN growth to include growth of AlGaN alloy layers.

CHAPTER 3

RF PLASMA-ASSISTED MBE GROWTH OF InGaN/GaN SUPERLATTICES

3.1 Introduction

InN has a much narrower bandgap than GaN; the bandgaps are 1.9 eV and 3.4 eV at room temperature, respectively. Both InN and GaN are thermally stable, chemically robust, and mechanically strong. Additionally, both InN and GaN are direct gap semiconductors. As such, both InN, GaN, and alloys of the two have been pursued widely for use in numerous optoelectronic and electronic applications. However, the growth of structures containing InGaN alloys has been beset by numerous difficulties. These include a large lattice mismatch between InN and GaN, a large miscibility gap for InN in GaN, phase segregation and non-random alloy formation during growth, surface desorption of deposited In, and thermal instability of InN at the normal GaN growth temperatures.

This chapter will be concerned with a series of experiments designed to elucidate and characterize the phenomenology of InGaN alloy layer growth by RF plasma-assisted molecular beam epitaxy (RF-MBE). Since the principal techniques used to characterize the samples are RHEED and HRXRD, the samples grown were superlattice structures; the periodic superlattice structure provides for a more straightforward, more detailed, and more accurate analysis of the samples by HRXRD, and the growth of a periodic structure allows more opportunities to observe and study the RHEED transitions at layer interfaces. The effects of substrate temperature, and incident N*/III flux ratio have been studied, and will be discussed in this chapter. The effects of microscopic processes occurring at the growth surface on the In incorporation efficiency for the InGaN layers and for the overall sample quality is discussed in detail.

3.2 Experimental Details

A simple InGaN/GaN superlattice test structure was designed in order to study the In incorporation into RF-MBE grown samples. The nominal structure, shown in Fig. 3.1 on p. 78, consists of a 20 period superlattice with alternating $In_xGa_{1-x}N$ and GaN layers with thicknesses of 30 Å and 200 Å respectively.

The In mole fraction x of the $In_xGa_{1-x}N$ alloy layer was nominally intended to be approximately 30%. This structure design was tuned using a kinematical X-ray simulation to maximize the superlattice satellite diffraction peaks that could be observed in HRXRD experiments. Additionally, a small number of superlattice periods and In mole fraction for the $In_xGa_{1-x}N$ alloy layers were used in the structure to prevent strain relaxation of the superlattice structure.

Two distinct sample sets were grown in order to study the RF-MBE growth of InGaN epilayers. In the first set, systematic variations of the incident N* and metal fluxes were used to elucidate the growth phenomenology. In the second sample set, the substrate temperature during deposition of InGaN/GaN structure was varied from run-to-run while all other growth parameters where held constant. The orientation of the substrates in the growth chamber is an important detail in both sets of samples. The orientation of the Al_2O_3 substrate relative to the flux sources is shown in Fig. 3.2 on p. 79. As shown in the figure, the In and Ga cells are located adjacently on the MBE source flange. Additionally, the RF plasma source is located (nearly) diametrically opposite the two metal sources. By using this growth geometry, the axis indicated in the figure becomes very important when considering the effects of the various flux ratios. The cell geometry provides that the Ga/In flux ratio is *invariant* along this axis. Furthermore, the ratio of the N* flux to the total metal flux, that is the N*/III flux ratio, varies continuously along this axis. Consequently, by holding the substrate in a fixed orientation, i.e. *not* rotating during deposition, the effects of systematic variations in the N*/III flux ratio can be directly observed by performing *ex situ* characterizations, such as HRXRD and PL, at points along this axis.

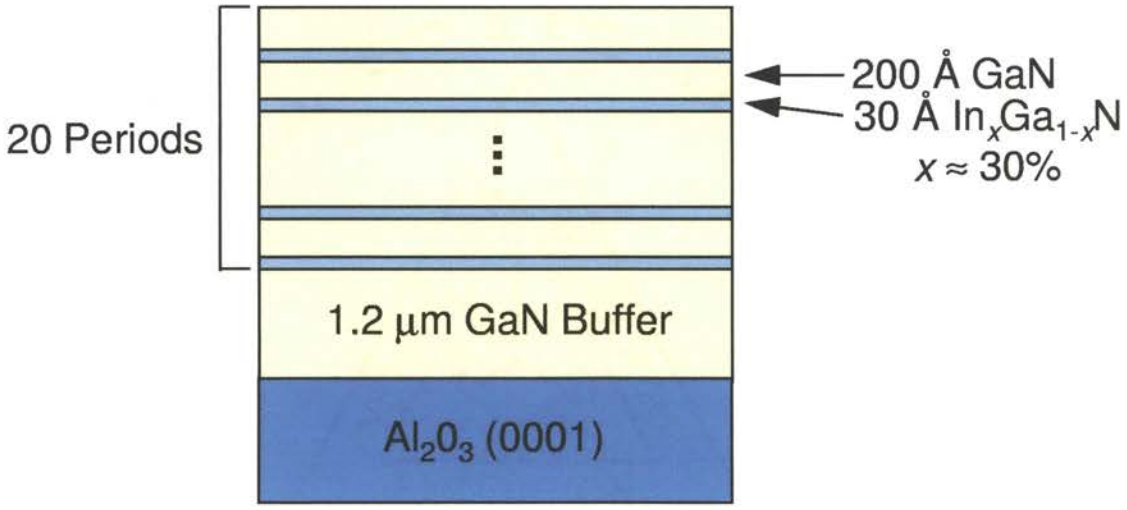

Figure 3.1. The InGaN/GaN superlattice sample structure consists of 20 periods of alternating $In_xGa_{1-x}N$ (x nominally 30%) and GaN layers with nominal thicknesses of 30 Å and 200 Å respectively. This structure is deposited on a 1.2 μm GaN buffer grown on an Al_2O_3 (0001) substrate.

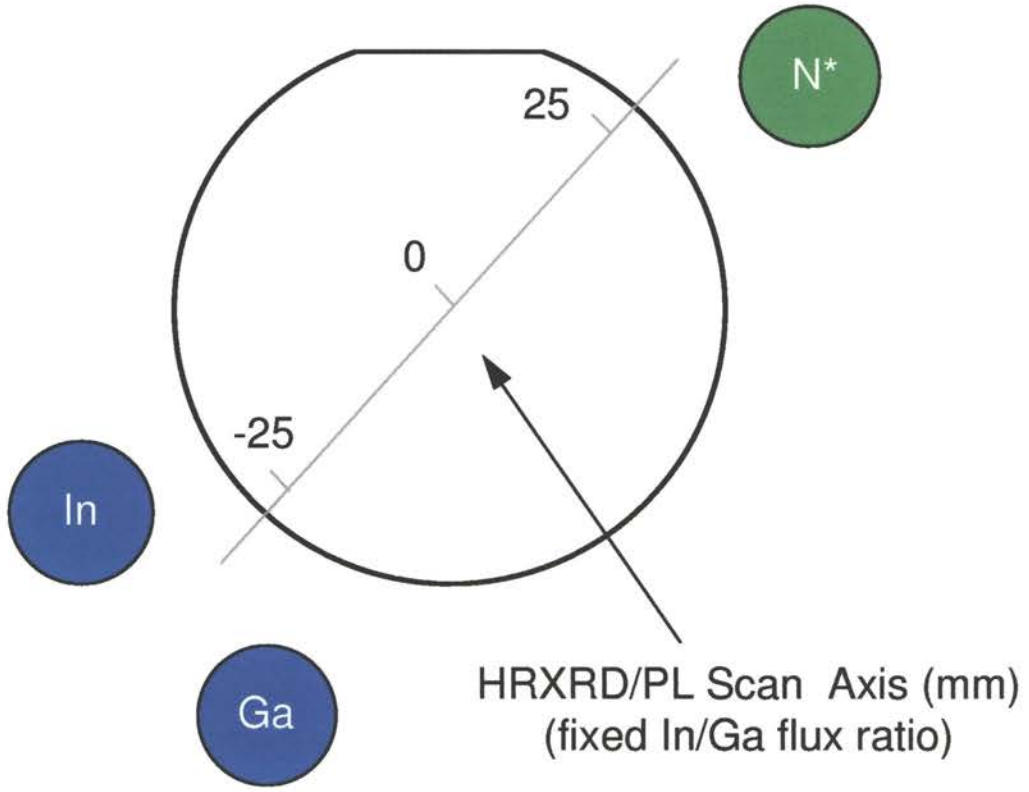

Figure 3.2. MBE growth geometry used for the deposition of InGaN/GaN superlattices. Adjacent In and Ga cells are located diametrically opposite the nitrogen source. This configuration results in a line on the wafer surface along which the In/Ga flux ratio is constant while the N*/III flux ratio varies. This line is used as the scan axis for laterally spatially resolved HRXRD and PL measurements.

All of the InGaN/GaN superlattice samples were grown using the same nominal procedure. Each superlattice sample was grown on an Al_2O_3 (0001) substrate. The back of each substrate was first coated with an opaque coating of thermally evaporated Ti. With no chemical preparation, the wafers were then mounted (using Ta wire supports) in a Mo block specifically designed for the high substrate temperatures typical of GaN growth. The Mo block and wafer were then loaded into the MBE system and outgassed at 300 °C for a minimum of 2 hours prior to growth; wafers were typically outgassed overnight prior to deposition. Outgassing of the wafers at this temperature is necessary to remove any adsorbed water or hydrocarbons captured or "gettered" by the Ti on the back surface; typically, a significant amount of hydrogen gas is evolved during this process.

Growth proceeds with a system preparation similar to that used for the deposition of GaN epilayers. Programs are executed on the computers controlling the MBE hardware to simultaneously raise the temperature of the substrate, Ga cell, and In cell under precisely controlled conditions in a particular sequence. First, the Ga cell is flashed to a high temperature (typically 20 °C higher than highest temperature needed during the growth run) for approximately 5 min. The Ga cell temperature is then gradually reduced to an idle temperature (typically 900 °C). The substrate reaches its peak temperature immediately after the Ga cell temperature begins to decrease. The substrate is heated to a peak temperature of approximately 800 °C and held at this condition for approximately 6 min. The substrate temperature is then reduced to approximately 760 °C for surface nitridation. Due to the high In vapor pressure and poor efficiency of the In cell shutter, the In cell cannot be flashed to high temperatures without significant deposition of In on the growth surface. Throughout this process, the MBE system is pumped using the ion- and cryo-pumps, as well as having the cryopanels filled with liquid nitrogen.

Using the procedure described in Chapter 2, the surface of the Al_2O_3 substrate is nitrided by exposure to the N* plasma for 45-53 min operating at 400 W forward power and a chamber pressure of 2.0×10^{-5} Torr. Following the surface nitridation, the substrate temperature is lowered to approximately 750 °C and a GaN buffer is

deposited at approximately 0.8 μm/h; typically, the RF plasma source is operated at 500 W forward power with a chamber pressure of 5.0×10^{-5} Torr for the GaN buffer deposition. Deposition continues under these conditions for approximately 90 min to produce a 1.5 μm-thick buffer.

Special care must taken in preparing the MBE system for InGaN/GaN superlattice deposition following the GaN buffer deposition. In order to prevent buildup of metals on the MBE growth surface due to shutter leakage, an intricate procedure most be followed. This nine-step procedure is illustrated in Fig. 3.3 on p. 82. Following the GaN buffer deposition, the Ga cell and substrate will be at high operational temperatures while the In cell idles at a low nominal temperature (typically 700 °C). The first step is to ramp the Ga cell temperature to an idle temperature to sufficiently reduce the Ga flux leakage around the cell shutter. Next, the wafer stage is moved from the growth position to the wafer transfer position; in this position, the wafer is no longer line-of-sight to the cells, thus eliminating direct metal fluxes from reaching the wafer. While in this position, the substrate temperature is reduced to a value near that to be used for the superlattice deposition. The wafer stage is then placed in the normal growth position, and fine adjustments are made to set the substrate temperature; it is necessary to perform these fine adjustments with the wafer in the growth position for two reasons: (1) the optical pyrometer can only observe the wafer in the growth position, and (2) minor differences in the contact of the thermocouple against the heater assembly affect the temperature control loop. The wafer stage is again placed in the transfer position, and the In and Ga cell temperatures are increased to the correct operational conditions for the superlattice deposition. The final three steps must be performed in *rapid* sequence. Once the cells have stabilized at their growth conditions, the wafer stage is tilted to the growth position and the N* plasma is ignited and stabilized at the growth condition (nominally 320 W forward power & 4.0×10^{-5} Torr). Lastly, deposition of the superlattice structure is initiated by executing a program on the MBE system control computers; these computers will then open and close the shutters on the preprogrammed duty-cycle.

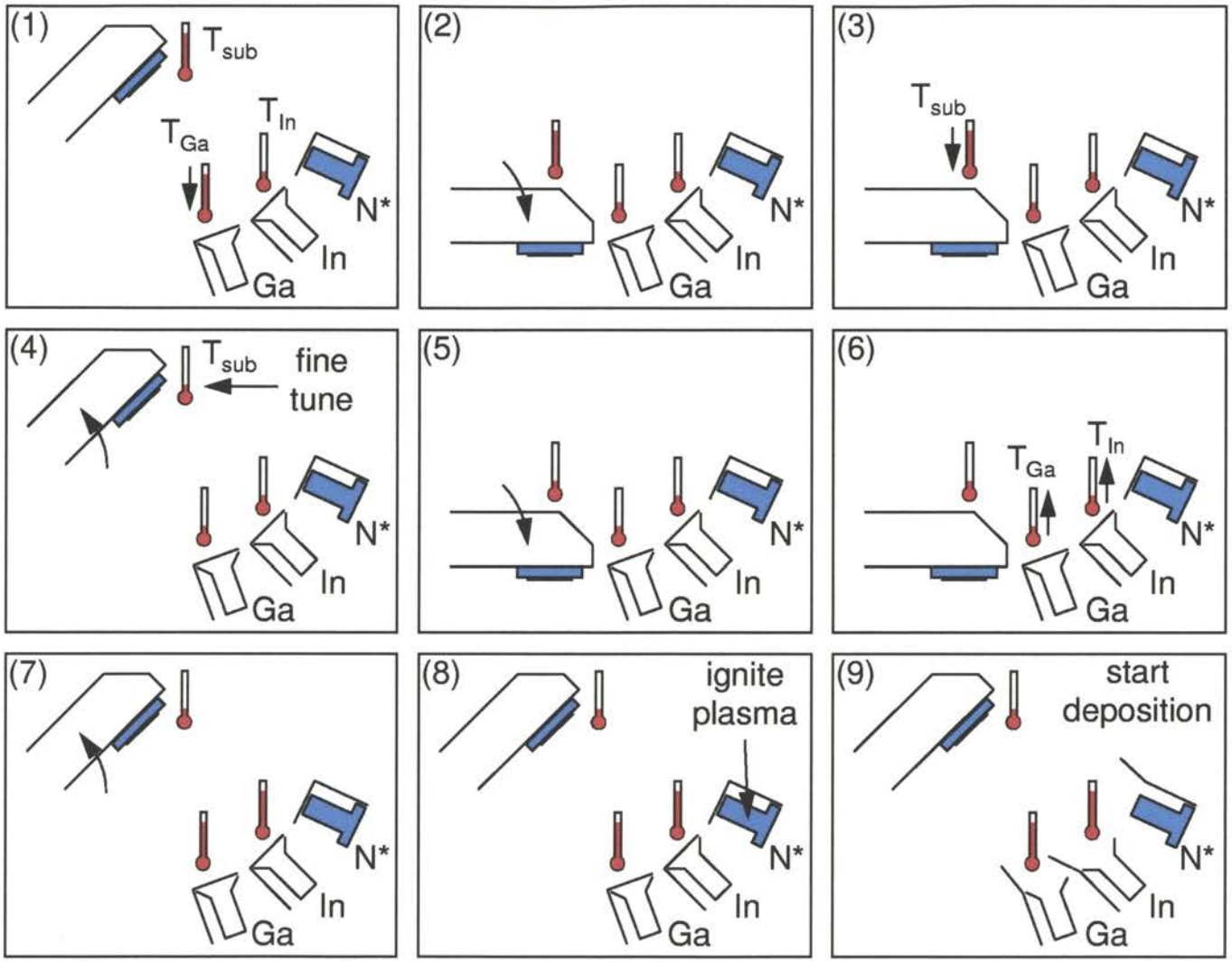

Figure 3.3. Procedural steps for preparing the MBE system for InGaN/GaN superlattice growth. Nine steps are necessary to prevent deposition of metal on the growth surface prior to superlattice deposition (see text). Thermometers are used to schematically represent temperatures or temperature changes.

The nominal deposition times for the InGaN and GaN layers are 20 s and 210 s respectively. Additionally, there is no dwell or latency time between the layer depositions. After the superlattice structure has been deposited, the plasma is quenched by reducing the applied RF power and the flow of N_2 gas into the chamber is stopped. Since the superlattice structure is always terminated with a GaN layer, it is not necessary to grow a cap layer. The wafer stage is then lowered to the transfer position so that routine calibration checks of the metal fluxes may be performed using the quadrapole mass spectrometer. Lastly, the sample temperature is ramped to room temperature and the In and Ga sources are ramped to their idle conditions.

The complete superlattice growth procedure is illustrated in Figs. 3.4-3.6 beginning on p. 84. Each of these figures shows data logged by the automated computer monitoring described in Appendix A. Figure 3.4 illustrates the changes in the power applied to the wafer heater and Ga and In effusion cells for each of the steps in the deposition of the superlattice samples. Figure 3.5(a) reveals the sample temperature (as determined by the optical pyrometer) for each step in the growth procedure. For comparison, Fig. 3.5(b) again shows the power applied to the sample heater. Lastly, Fig. 3.6 reveals the variations in operational parameters for the RF plasma source for each step in the superlattice growth. The applied RF power is shown in Fig. 3.6(a) and the MBE growth chamber pressure, an indicator of the N_2 flow rate, is shown in Fig. 3.6(b).

All superlattice samples have been characterized *in situ* using 10 kV RHEED and *ex situ* with spatially-resolved HRXRD measurements. Additionally, low-temperature PL measurements were performed for specific samples. Spatially-resolved symmetric HRXRD measurements were performed about the GaN (0002) diffraction peak in the ω-2θ geometry. The measurements were performed using Cu-Kα_1 radiation and a Philips Materials Research Diffractometer equipped with triple-axis detector optics. PL measurements were performed at 10 K using a cryogenic refrigerator and the 325 nm line of a HeCd laser as the excitation source. Luminescence was collected into a Spex 1000M single-grating (1200 groove/mm blazed at

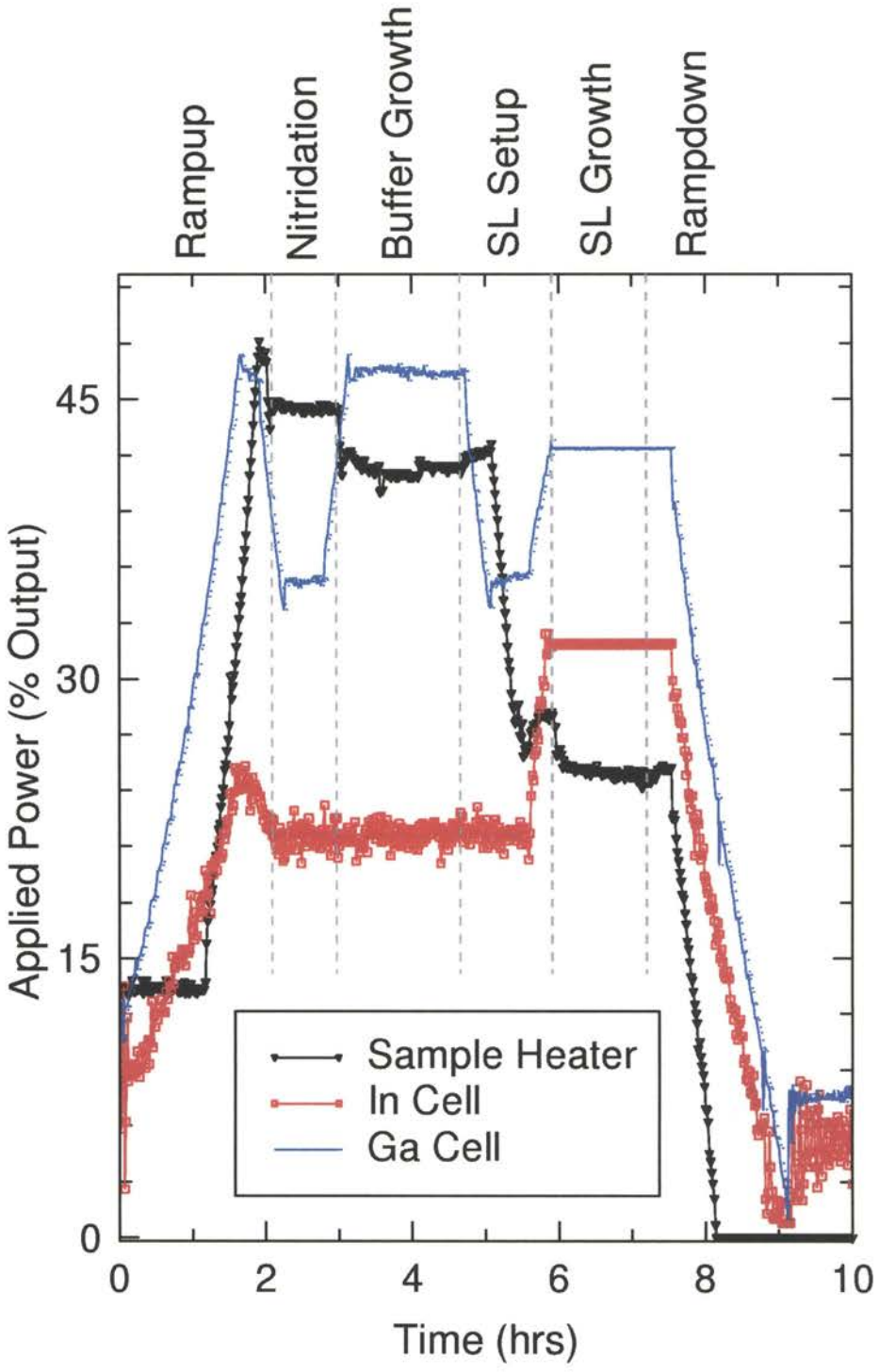

Figure 3.4. Profile of the power applied to the Ga and In effusion cells and wafer heater during the deposition of an InGaN/GaN superlattice sample. The distinct sample deposition processes are indicated. The applied power is expressed in units of "% Output," (see Fig. 2.4).

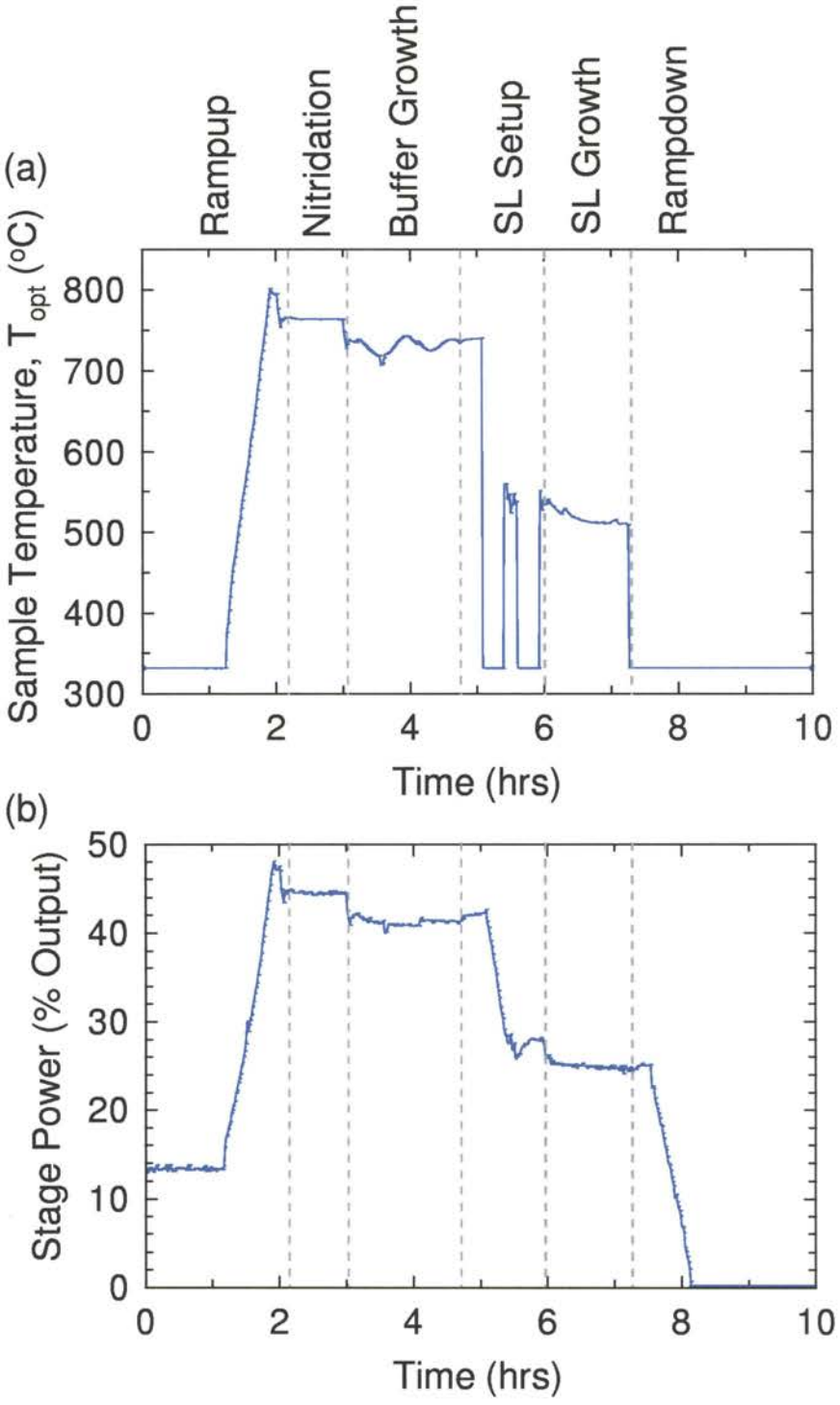

Figure 3.5. Profile of (a) the sample temperature (as determined by the optical pyrometer) and (b) applied heater power (expressed as a percentage of the maximum voltage that can be applied) during the deposition of an InGaN/GaN superlattice sample. The distinct sample deposition processes are indicated.

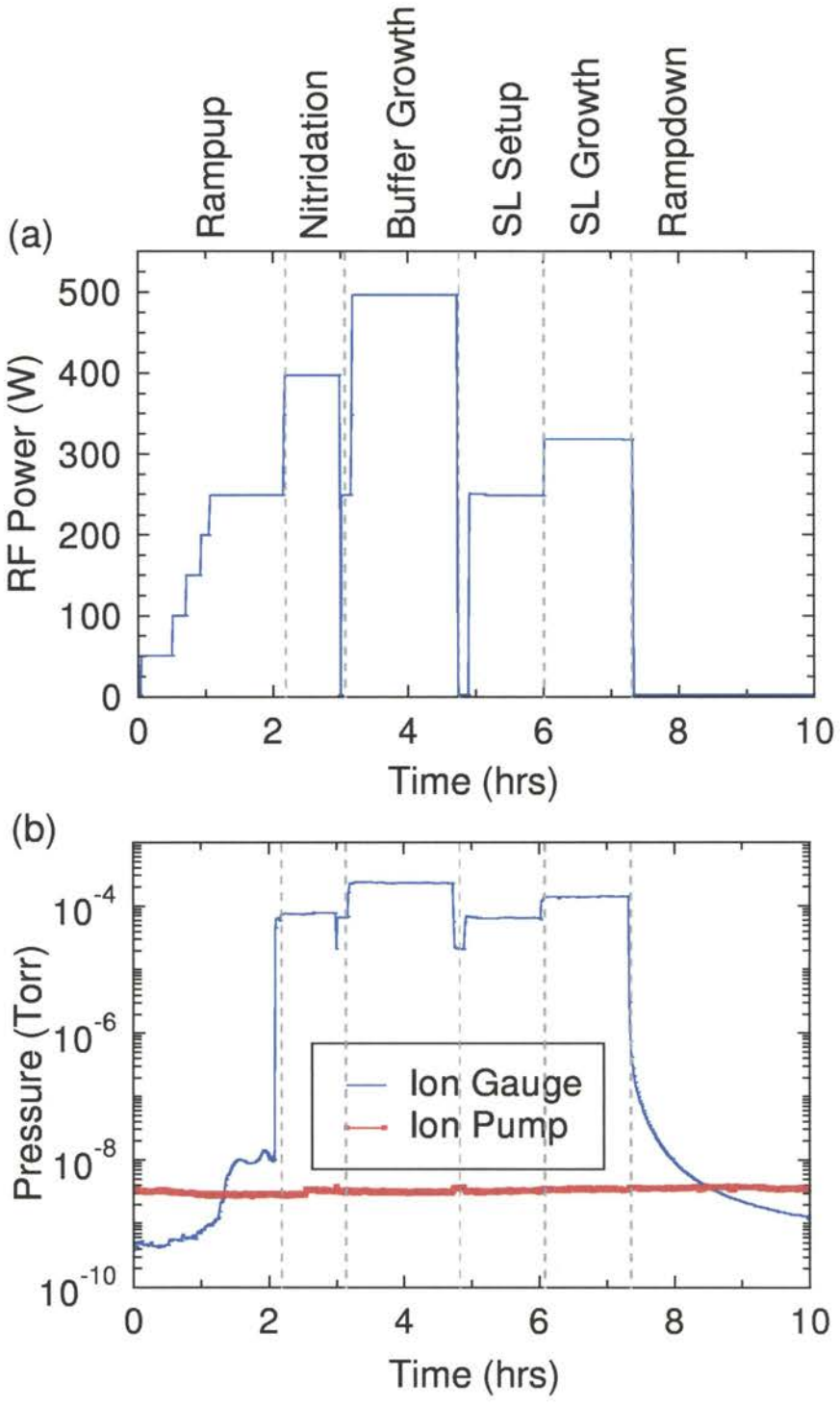

Figure 3.6. Profile of (a) the RF plasma source forward power and (b) MBE growth chamber pressure during the deposition of an InGaN/GaN superlattice sample. The distinct sample deposition processes are indicated.

670 nm) 1 m spectrometer and detected using a Hamamatsu 1P28A photomultiplier tube.

3.3 Results and Discussion

High-resolution X-Ray diffraction (HRXRD) was used to characterize each superlattice sample that was grown. Symmetric X-ray scans were acquired about the GaN (0002) diffraction peak in the ω-2θ geometry. A typical HRXRD scan is shown in Fig. 3.7(a) on p. 88. A family of InGaN/GaN superlattice peaks is clearly observable about the GaN (0002) diffraction peak. A great deal of information about the sample structure can readily be obtained by analyzing the superlattice peak positions. As indicated in Eq. 1.1 of Sec. 1.4.1.2, the superlattice period L and average atomic-plane spacing $\bar{d}$ may be determined through linear regression analysis of a plot of the quantity $2\sin\theta_n/\lambda$ versus n, where θ_n is the peak position of the nth order superlattice peak. Such a plot is shown in Fig. 3.7(b). The period L and average atomic-plane spacing $\bar{d}$ are obtained by interpreting the slope and intercept values from the linear regression. By assuming the applicability of Vegard's law, the average alloy composition of the superlattice bilayer $\bar{x}$ can be calculated. Reconciling with the layer deposition times (known from growth) and assuming (1) the structure is coherently strained (verified through asymmetric HRXRD measurements) and (2) the In is confined entirely to the InGaN alloy layers, allows further estimation of the In mole fraction of the InGaN alloy layers and the average GaN and InN growth rates; that is, the average rates at which GaN and InN are incorporated in the sample.

3.3.1 N*/III Flux Ratio

The first set of superlattice samples was grown with systematic changes in the incident N*/III flux ratio in order to understand the salient growth phenomenology. The effects of the incident N*/III flux ratio were studied by performing the X-ray measurements and calculations described above for each sample. Furthermore, to precisely understand the incident N*/III flux ratio effects, X-ray measurements were

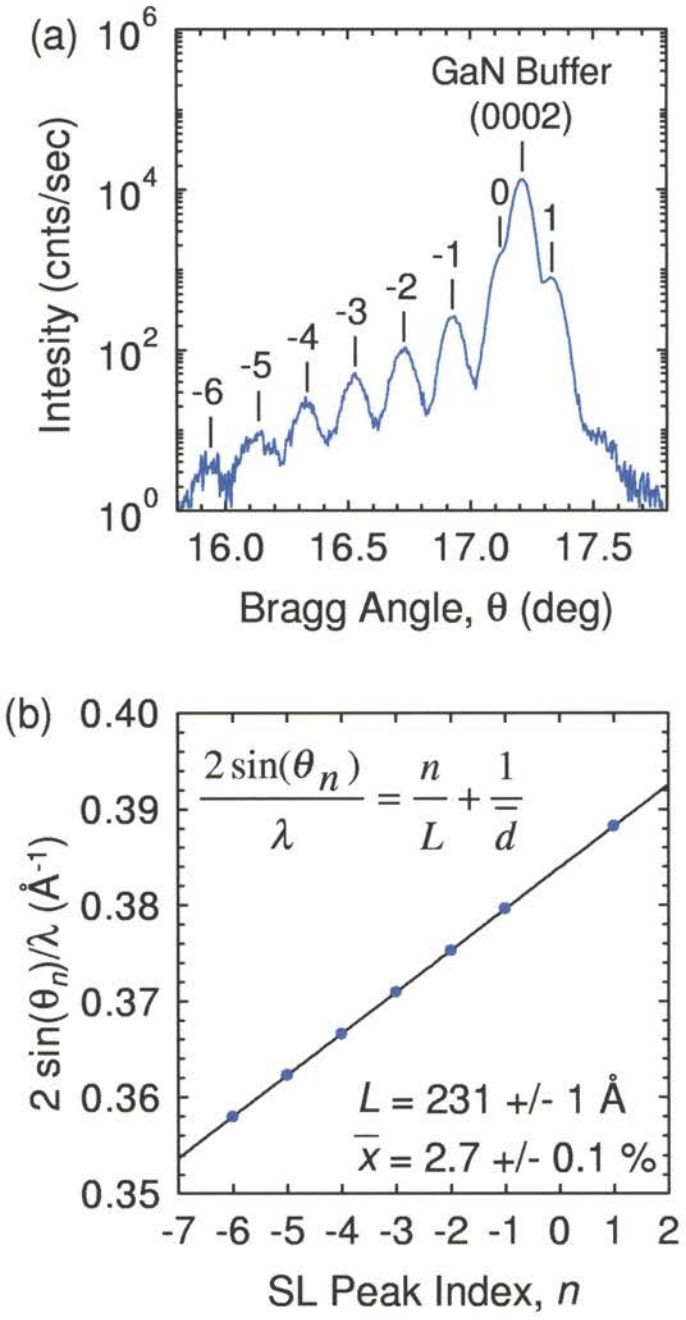

Figure 3.7. Typical HRXRD data and analysis of InGaN/GaN sample structure to determine In composition. (a) A family of superlattice peaks can be observed about the GaN (0002) peak (due to the buffer). (b) The superlattice period L and average atomic-plane spacing $\bar{d}$ are obtained by applying linear regression analysis to a plot of $2\sin\theta_n/\lambda$ vs. superlattice peak index n. This allows further estimation of the average In composition of the superlattice and the InGaN alloy layer (see text).

performed at a number of points over the wafer surface along the axis described in Fig. 3.2. Due to the geometry of the N* and metal sources, each point along this axis represents growth at a different N*/III flux ratio.

Studying the samples in this way reveals the relevant growth phenomenology. Overall trends in the growth of InGaN/GaN superlattices are observed indicating the growth may be limited by the arrival rate of either N* or metals. This is illustrated in Fig. 3.8 on p. 90. The figure shows the (a) superlattice period L, (b) superlattice average alloy composition $\bar{x}$, (c) effective GaN growth rate, and (d) effective InN growth rate each versus the position along the lateral scan axis for two different incident N* flux conditions. Negative coordinate values (positioned nearer the metal sources) represent growth under lower N*/III flux ratios, while positive coordinate values represent growth at higher N*/III flux ratios. Of particular interest are the GaN and InN effective growth rates shown in figures (c) and (d). For the data shown, the InN effective growth rate increases as one moves from lower to higher N*/III flux ratios (i.e. to the right) beginning nearest the metal sources. Likewise, the InN effective growth rate increases as one moves from higher to lower N*/III (i.e. to the left) beginning nearest the N* plasma source. The InN effective growth rate increases from both sides to a maximum value. Likewise, similar trends are observed in the GaN effective growth rate. It is worth noting that the maxima in the GaN effective growth rate *always* occurs at a lower N*/III flux ratio than the InN effective growth rate maxima. Moreover, these maxima are sufficiently different so that it is difficult to simultaneously observe both the GaN and InN growth rate maxima on a single 2 in wafer.

Comparing the nature of these curves to earlier work presented for GaN growth strongly suggests that the shape and maxima observed in the growth rate curves are attributable to a transition from metal arrival-rate limited growth to N* arrival-rate limited growth. That is, the increase in growth rate as one moves to the right is due to a larger relative flux of the N*; thus, the growth rate is N* arrival-rate limited in that regime. Likewise, the observed increase in growth rate moving to the left is due

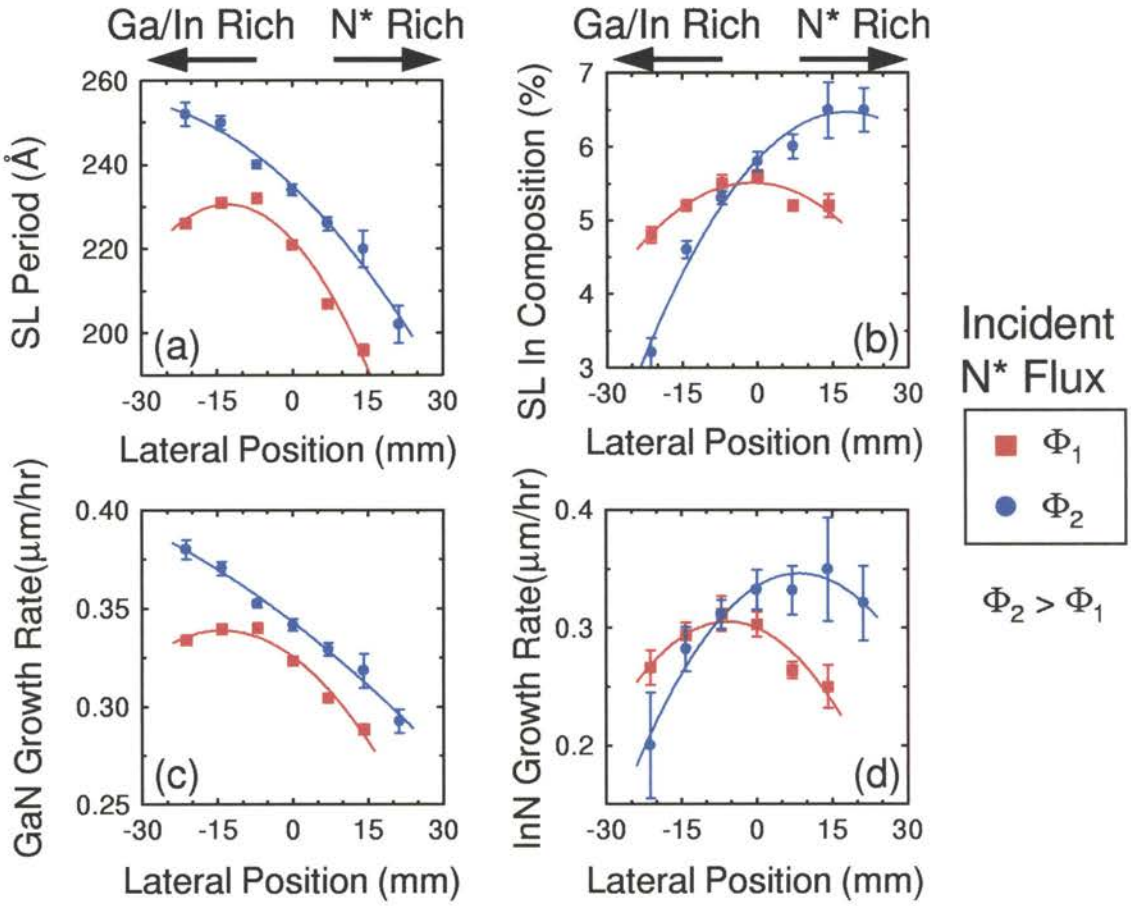

Figure 3.8. HRXRD determined (a) superlattice period, (b) In composition, (c) GaN growth rate, and (d) InN growth rate as a function of wafer position (metal/N* flux ratio). Separate distinct maxima are observed for the InN and GaN growth rates suggesting that a higher N*/III flux ratio is needed for InN growth.

to the larger relative flux of the metals; thus, the growth is limited by the arrival-rate of the metal species at the surface. The maxima that occur in these curves are then interpreted as the effective stoichiometric growth conditions for GaN and InN, respectively. The observation that the InN growth maxima always occurs at a higher N*/III flux ratio suggests that InN requires a higher N*/III flux than does GaN for stoichiometric growth at the same temperature. This is consistent with reports by other groups working with β-InGaN.[47]

A simple visual inspection of the samples supports the interpretation presented above. For samples that are grown with a relatively low N* flux, the edge of the sample nearest the metal sources is observed to be coated with metals. In such a metallized region, no useful HRXRD data can be extracted. The size and extent of this region is observed to increase for samples grown at lower N* fluxes and decrease for samples grown at higher N* fluxes. The metallized region can be eliminated entirely with sufficiently high N* fluxes. However, at high N* fluxes, the edge of the sample nearest the plasma source is degraded; the samples are observed to appear rough or less specular near this edge. All of these observations are consistent with the phenomenology observed in GaN growth associated with growth at extremely N*-deficient (metallized surface) and N*-rich (rough, degraded surface) conditions.

3.3.2 Substrate Temperature

The effects of the substrate temperature on the InGaN/GaN superlattices were studied through a second set of superlattice samples grown according to the nominal procedure described earlier. For each sample in this set, the substrate temperature during superlattice deposition was varied from run to run while all other growth parameters were held fixed. The substrate temperatures for the samples in this set were varied in the range 540–670 °C; the specific temperature used for each sample is listed in Table 3.1 on p. 93. Following from the discussion in the previous paragraph, the RF plasma source operating condition for InGaN/GaN superlattice deposition was chosen as 320 W forward power and a chamber pressure of 4.0×10^{-4} Torr; this condition was chosen to maximize the sample area from which useful XRD data

could be obtained. As a consequence, the N* flux was higher than that normally used for pure GaN growth to avoid metalization of the samples during the InGaN layer deposition.

Each sample in this second set has been characterized using *in situ* RHEED, and *ex situ* spatially-resolved HRXRD and low-temperature PL measurements. The HRXRD characterizations performed on this sample set are identical to those described earlier. The results of these HRXRD measurements reveal a strong and unusual dependence of the average alloy composition $\bar{x}$ (i.e. In incorporation efficiency) on the substrate temperature T_{sub}. This temperature dependence is revealed in Fig. 3.9 on p. 94. The figure shows a plot of the average In composition $\bar{x}$ versus the quantity $1000/T_{\text{sub}}$. All the data for this plot was taken from the same position on each wafer (the center of the useful data range) and therefore represents growth at a fixed incident N*/III flux ratio.

Figure 3.9 suggests there are two distinct temperature regimes in the growth of the InGaN/GaN superlattices. Firstly, at temperatures lower than a critical temperature ($T_C \approx 590\,^{\circ}\text{C}$) the average In composition of the superlattices is approximately constant and near the intended nominal composition ($x \approx 30\%$). At temperatures above T_C, $\bar{x}$ decreases by more than an *order of magnitude* in the temperature range 590–670 °C. At growth temperatures above 680 °C there was insufficient In in the samples for characterization by HRXRD. HRXRD measurements confirm, however, that the Ga incorporation rate is indeed *constant* throughout this temperature range. Lastly, in this high temperature regime, $\bar{x}$ is well described by a Boltzmann-factor temperature dependence with some effective activation energy.

The temperature dependence of $\bar{x}$ described above suggests a physical origin for the observed effects. In the low-temperature regime, it appears that the In composition is determined by the incident In/Ga flux ratio. That is, the sticking coefficients for both metals are effectively unity in this temperature range. However, at higher temperatures, the Boltzmann temperature dependence of $\bar{x}$ strongly suggests that a thermally-activated kinetic process (or processes) is limiting the In incorporation.

Sample ID	Growth Temperature (°C)	Heater Power (% Output)
os98.037	537 ± 5	24.9
os98.035	580 ± 5	27.6
os98.034	588 ± 5	28.2
os98.036	620 ± 5	30.3
os98.040	648 ± 5	32.3
os98.039	672 ± 5	34.0

TABLE 3.1. Table of the superlattice growth temperatures and heater powers used in the substrate growth temperature study. Substrate temperatures are measured using the optical pyrometer. Heater power is expressed as a percentage of the maximum voltage available from the heater power supply as explained earlier (see Fig. 2.4).

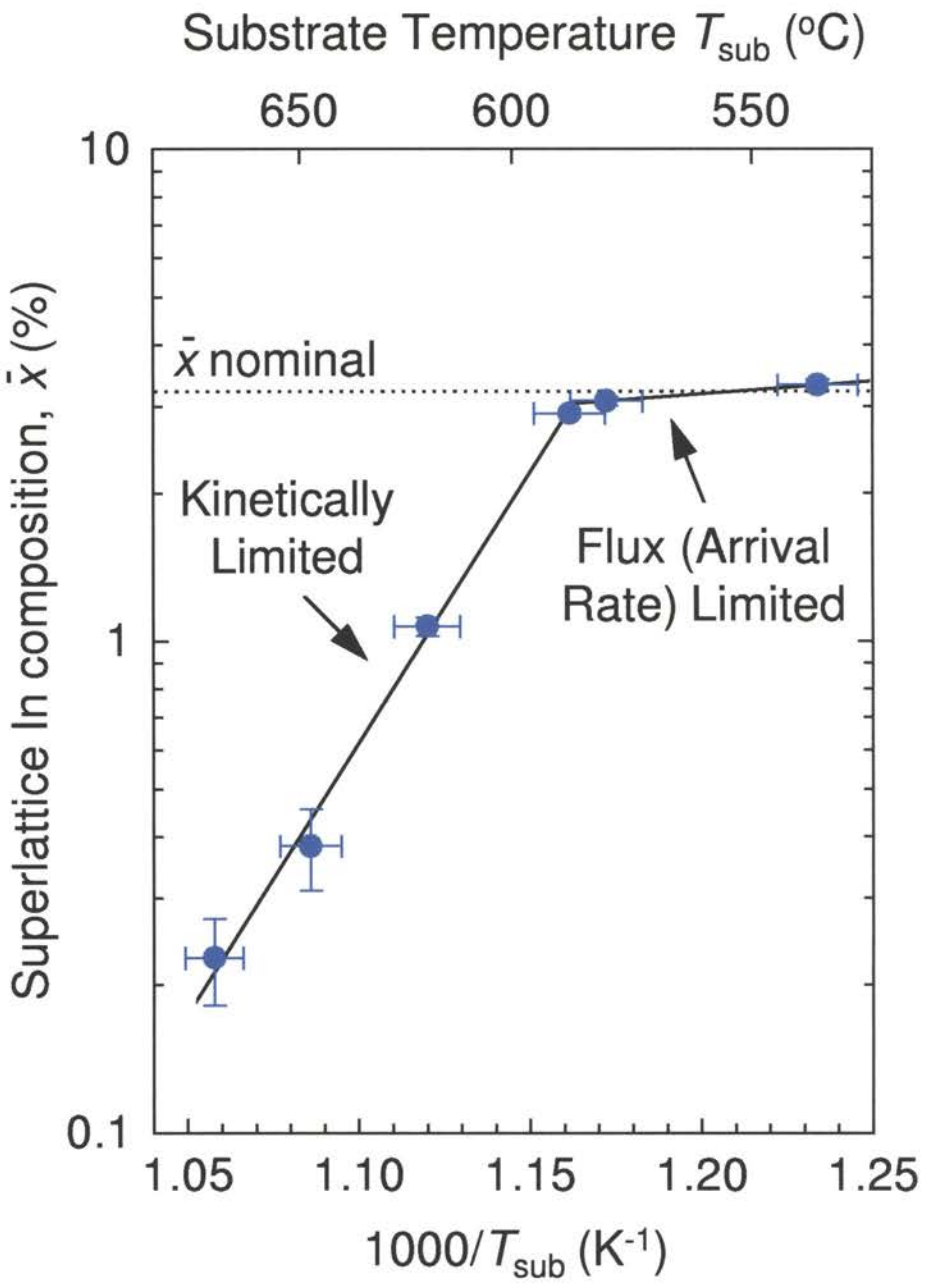

Figure 3.9. Arrhenius plot of superlattice In composition as a function of substrate temperature for a fixed incident N*/III flux ratio. Below approximately 590 °C the In composition is nominally constant. Above this temperature, the In composition sharply decreases, falling by more than an order of magnitude in the temperature range 590–670 °C.

3.3.3 Combined Effect of Substrate Temperature and N*/III Flux Ratio

Careful examination of spatially-resolved HRXRD measurements reveals that the N*/III flux ratio also strongly affects the In incorporation efficiency for the superlattice samples grown above the critical temperature ($T_C \approx 590\,^{\circ}\mathrm{C}$). That is, a strong increase in the In incorporation efficiency is observed for even a slight increase in the N*/III flux ratio. This effect of the N*/III flux ratio to increase the In incorporation efficiency is shown in Fig. 3.10 on p. 96. The figure shows Arrhenius plots of the average In composition as a function of substrate temperature similar to that shown in Fig. 3.9 for several different N*/III flux ratios. Several features of the figure are immediately obvious. Firstly, at low temperatures, the In composition is essentially constant at the nominally intended In composition. Secondly, at higher temperatures, the In composition is reduced by more than an order-of-magnitude from the nominal level at the lowest N*/III flux ratio. However, at higher N*/III flux ratios, significantly more In is incorporated into the samples. Nearly an order-of-magnitude increase in the incorporated In is observed for only a 20% increase in the incident N*/III flux ratio. Lastly, at each N*/III flux ratio, the temperature dependence of the In composition is well described by a Boltzmann factor temperature dependency. For each N*/III flux ratio, a separate *effective* activation energy is observed. These effective activation energies are found to decrease monotonically in the range 0.8–2.7 eV as the N*/III flux is increased.

The observations above clearly suggest a number of things about the growth of the InGaN/GaN superlattices. First, the observation that at temperatures below T_C the superlattice In compositions are effectively independent of minor variations in the N*/III flux ratio supports the assessment of the growth in this regime as being limited by the arrival-rate of the incident fluxes. Additionally, as stated earlier, the temperature dependence of the In composition at temperatures above T_C strongly suggests that a thermally-activated process (or processes) is responsible for the observed decrease in incorporated In. However, the absence of a single activation energy

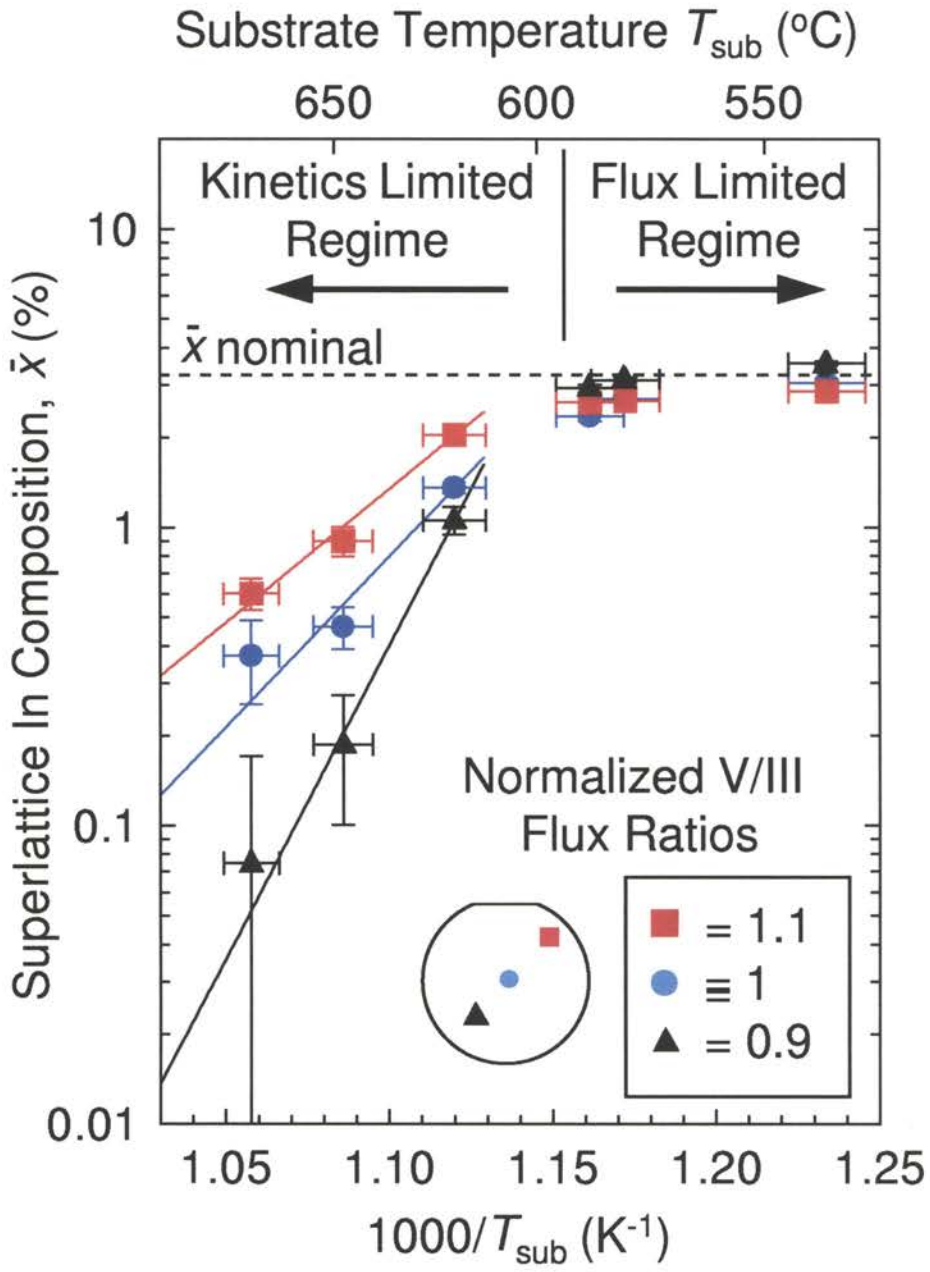

Figure 3.10. Effect of N*/III flux ratio on superlattice In composition. Shown is an Arrhenius plot of superlattice In composition vs. substrate temperature for several N*/III flux ratios. At low substrate temperatures, the average In composition is effectively independent of the N*/III flux ratio. In the temperature range 590–670 °C, the average In composition decreases rapidly and is strongly influenced by the N*/III flux ratio; more than an order-of-magnitude decrease in In composition is observed over the temperature range shown. Nearly an order-of-magnitude increase in In composition is observed at the highest temperature of this study.

is evidence that more than one thermally-activated process is responsible for the decrease in incorporated In. Furthermore, the N*/III flux ratio must affect one or more of these processes.

The physical processes responsible for the observed decrease in In incorporation efficiency at high growth temperatures may be In surface-segregation in combination with In surface-desorption. It is physically reasonably to expect such thermally-activated processes in the growth of InGaN/GaN superlattices. Firstly, desorption of In from the growth surface and segregation of In to the growth surface have been reported by other research groups. Additionally, it is well known that the InGaN material system suffers from serious fundamental difficulties including a large miscibility gap, poor thermal stability of InN compared to GaN, and a large lattice mismatch between GaN and InN. Each of these difficulties would suggest that In does not readily incorporate into GaN layers; consequently, it is reasonable to expect that that In adatoms will have a high mobility (both laterally and perpendicularly) on the growth surface. Lastly, thermally-activated surface-segregation and surface-desorption are known problems in other material systems; previous research by this group has shown that the incorporation of N in GaNAs/GaN superlattice structures was significantly reduced due to a kinetic mechanism involving surface-segregation in combination with surface-desorption.

A surface-segregation and surface-desorption interpretation can readily explain the temperature dependency observed in the growth of the InGaN/GaN samples. At low temperatures, these In loss mechanisms are effectively kinetically frozen out. Thus, nearly all In deposited on the surface is incorporated in the sample. At higher temperatures, the same kinetic processes become active, introducing two possible pathways for the removal of In from the sample. In the first pathway, In may directly desorb or evaporate from the growth surface during the deposition of the InGaN layer. In the second pathway, either during or immediately following the InGaN layer deposition, In may segregate to the (advancing) growth surface and subsequently desorb. As both segregation and desorption are thermally-activated processes, it it reasonable to expect that at very high temperatures, these mechanisms will dominate,

resulting in negligible In incorporation into the sample. This prediction is in good agreement with the experimental observation that no In could be detected in samples grown at temperatures higher than 680 °C.

The effect of the incident N*/III flux ratio on the In incorporation efficiency can also be understood to be consistent with a surface-segregation/surface-desorption model. The local N*/III flux ratio at any point of the sample surface will determine the surface concentration of N for that local region of the sample. The effect of a higher or lower incident N*/III flux ratio will be to either raise or lower the surface concentration of N atoms, respectively. Physically, a higher surface concentration of N may act through several pathways to result in a higher fraction of the deposited In to be incorporated. Firstly, the energy of the intermediate bonds that are formed between adatoms and the growth surface is dependent on the particular species involved. The intermediate bonds between In adatoms and surface (or subsurface) N atoms will be stronger, i.e. of higher energy, than those between In adatoms and In or Ga surface atoms. Therefore, one possible effect of the higher surface concentration of N is to increase the average residence time of the In adatoms on the surface (prior to desorption), resulting in a higher In incorporation efficiency. Secondly, a possible pathway for In surface-segregation to occur is through a Ga-for-In exchange between adlayer and surface (or subsurface) atoms. Such an exchange would be energetically favorable as this would reduce the strain in the epilayer. A higher N surface concentration would result in a lower Ga surface concentration; consequently, the Ga-for-In cation exchange rate would be reduced. This would reduce the rate of In atoms segregating to the growth surface and a greater fraction of the In would be incorporated. Lastly, it is generally the case in III-V MBE that a higher concentration of the group V species results in a reduced surface mobility of species at the surface.* This is in good agreement with the growth results presented in Chapter 2 for the growth of GaN, where it was necessary to use a sufficiently large Ga flux to enhance the Ga

*This is the underlying principle behind migration-enhanced epitaxy (MEE). In this technique, codeposition of the group V element is periodically interrupted to enhance the mobility of group III elements at the surface; thus, allowing for an improved growth surface.

surface migration, resulting in a flatter, improved growth surface. In the case of a higher N surface-concentration, the mobility of Ga (and In) atoms in the adlayer will be reduced. As a second-order effect, this will reduce the probability of Ga atoms migrating to the site of an incorporated In atom and allowing a Ga-for-In cation exchange. Consequently, the In surface-segregation rate would be further reduced, resulting in a higher In incorporation efficiency.

Additional support for a surface-segregation/surface-desorption interpretation is provided by the RHEED patterns observed during the growth of the InGaN/GaN superlattice samples. The RHEED patterns observed during deposition of the superlattice samples are dominated by (1×1) RHEED patterns throughout the deposition cycle. However, details of the RHEED patterns vary as a function of the incident flux conditions and the substrate temperature T_{sub}. Representative RHEED patterns observed during superlattice growth are presented in Fig. 3.11 on p. 100. These RHEED patterns were observed with the electron beam directed along the $[11\bar{2}0]$ azimuth. In the figure, pairs of RHEED patterns observed during GaN and InGaN deposition are shown for growth temperatures of (a) 670 °C, (b) 580 °C, and (c) 540 °C. It should be noted that, because of the arrangement of the RHEED patterns in this figure, the effect of increasing substrate temperature can be seen by comparing RHEED patterns stacked in columns (higher temperatures appearing higher in the column). Additionally, the effect of the In flux can be observed by comparing RHEED images in rows (higher total metal flux appearing to the right).

In general, the RHEED patterns are always spotty or faceted to some degree. RHEED images observed near the critical temperature ($T_C \approx 580\,°\text{C}$) tend to have the most specular appearance. The RHEED images are observed to become more spotty and somewhat diffuse at successively lower substrate temperatures. However, at temperatures above T_C, the RHEED patterns are observed to have well defined chevron-like facet features which become more prominent at higher growth temperatures. Additionally, the RHEED patterns were always observed to become more specular upon the onset of In codeposition for the InGaN layer growth. After the

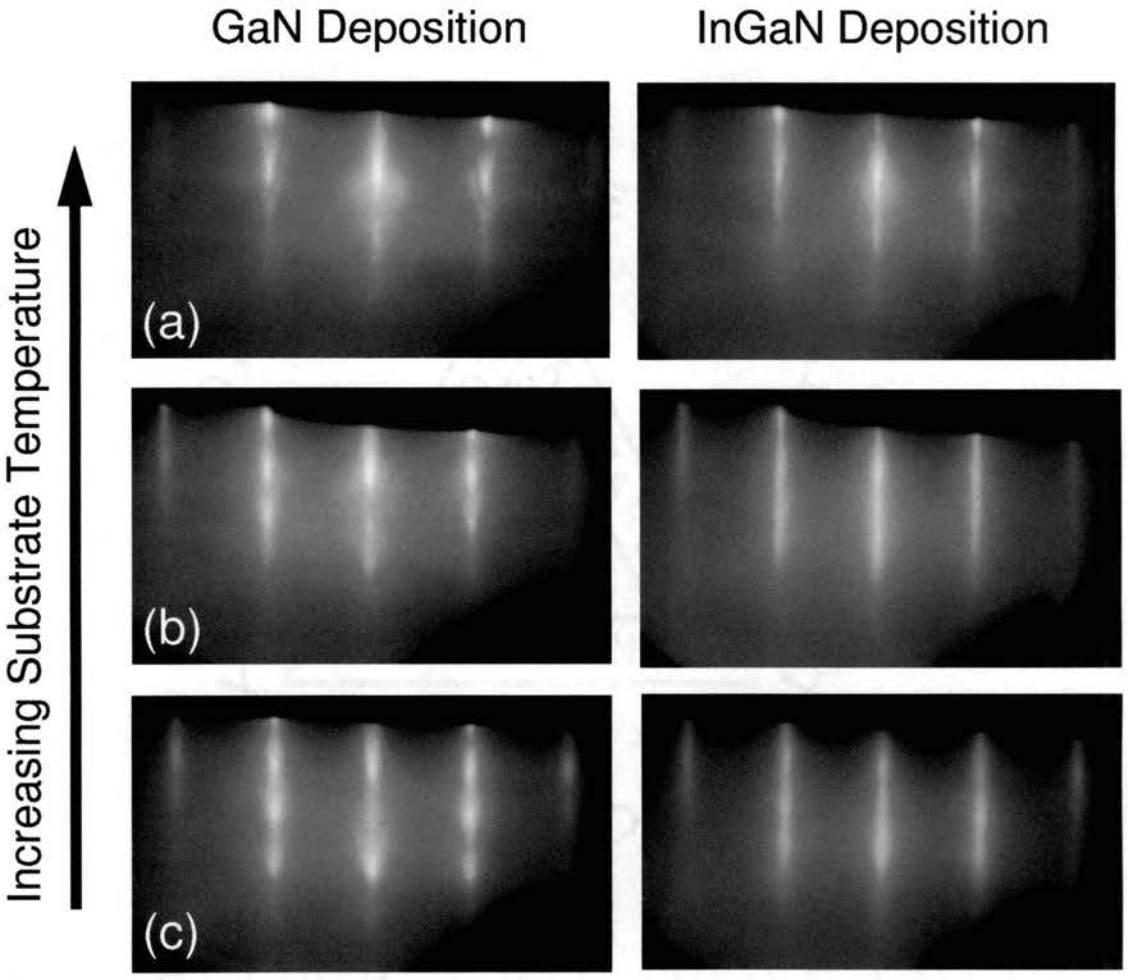

Figure 3.11. RHEED images observed along the [11$\bar{2}$0] azimuth during the deposition of GaN and InGaN superlattice layers. RHEED patterns are observed to be (a) faceted at high temperatures (670 °C), (b) comparatively specular at moderate temperatures (580 °C), and (c) poorly formed and spotty at low temperature (540 °C). All patterns are observed to be more specular during the deposition of InGaN.

In shutter closed at the end of the InGaN layer deposition, the patterns always returned to the original state (either more faceted or more spotty) after some period of time. It is important to note that the time for the transition to more specular RHEED patterns (at the onset of InGaN deposition) always occurred more expeditiously than the reverse transition (after completion of the InGaN layer deposition). Furthermore, the time necessary for the reverse transition (from specular to spotty or faceted) significantly increased at growth temperatures above T_C. At lower temperatures, the reverse transition occurred in approximately 15 seconds; however, at the highest temperature of this study ($T_{\text{sub}} \approx 670\,^{\circ}\text{C}$) the time for the reverse transition was approximately 45–60 s.

In order to understand the RHEED patterns described above, it is useful to touch again upon some relevant phenomenology from the growth of pure GaN. Firstly, it was observed that the N*/Ga flux ratio is a critical parameter in the growth of pure GaN. For growth under N*-rich conditions, the surfaces were observed to roughen; the RHEED patterns were observed to develop chevron-like features at high temperatures and more spotty features at low temperatures. Likewise, GaN surfaces were observed to be specular under flux condition that were either stoichiometric or slightly Ga rich. Secondly, it was observed that RHEED patterns appeared most specular when $r \lesssim r_{\text{max}}$ where r is the growth rate and $r_{\text{max}} = r_{\text{max}}(T_{\text{sub}})$ is the maximum possible growth rate at a given substrate temperature (limited thermodynamically by the rate of crystal formation). RHEED patterns are observed to gradually become spotty and diffuse as the substrate temperature is lowered, or alternatively, as r_{max} is lowered while r is held constant. Likewise, RHEED patterns are observed to become increasingly more faceted as the substrate temperature is increased, or alternatively, as r_{max} is increased while r is held constant. At high growth temperature, i.e. when $r \ll r_{\text{max}}$, the RHEED patterns are dominated by strong chevron-like facet features.

In view of these results, the variation of the RHEED patterns observed during InGaN/GaN superlattice growth may easily be understood. Firstly, the observation of more specular RHEED patterns with the addition of the In flux is closely related

to the N*/Ga flux ratio in pure GaN growth. In the case of the InGaN/GaN superlattice growth, the rough RHEED patterns during GaN deposition may be understood to be due to an incident N*/Ga flux ratio that is N-rich. Recall that the N*/Ga flux ratio is higher than that used in pure GaN growth to avoid metallizing the surface during InGaN deposition. Once In codeposition begins, the N*/III flux ratio is lowered, resulting in a greater mobility of In and Ga on the growth surface and consequently, a flatter, more specular surface. Secondly, the temperature dependence of the InGaN/GaN RHEED patterns is again very similar to the GaN growth phenomenology. Faceted RHEED patterns are observed at higher growth temperatures; that is, at temperatures where $r \ll r_{\max}$. Additionally, spotty and diffuse RHEED patterns are observed at low growth temperatures; that is, where $r \gtrsim r_{\max}$.

More significantly, the rate of transition of the RHEED patterns described above provides further support for the surface-segregation/surface-desorption assessment for the In loss mechanism at high temperatures. The persistence of more specular RHEED patterns after the In shutter has closed following InGaN layer deposition is clear evidence that In is present on the growth surface and causes a modification of the surface morphology (due to the higher mobility of In compared to Ga). Additionally, the observation that the transition time (from specular to rough RHEED patterns) *increases* with increasing growth temperature strongly suggests that In is present on the surface due to thermally-activated segregation of In from subsurface layers to the growth surface.

PL results further support the surface-segregation/surface-desorption assessment of the In loss mechanism and provide insight into the effects of both the substrate temperature and N*/III flux ratio on the optical quality of the second set of samples. The PL spectra observed for these samples consist of single, broad luminescence peaks which often show Fabry-Perot fringes. Additionally, the luminescence peaks vary greatly in intensity and spectral position (i.e. energy) as a function of the growth conditions.

Figure 3.12 on p. 104 shows PL spectra observed at a number of positions along the scan axis defined in Fig. 3.2 for the sample grown at $T_{\text{sub}} \approx 650\,^{\circ}\text{C}$. Again, each

position along this axis represents growth under a different N*/III flux ratio. The figure clearly reveals that the PL spectra are strongly affected by the incident N*/III flux ratio. First, the PL peak positions are successively more red-shifted for growth at successively higher N*/III flux ratios. The observed red-shifting of the PL peak is consistent with a higher In alloy composition, in good agreement with HRXRD measurements and the previous discussion of surface-segregation/surface-desorption as the mechanism for the reduced In incorporation.

Additionally, Fig. 3.12 shows the PL peak intensity increases as the incident N*/III flux ratio is increased (over the narrow range of flux ratios used in this study). Furthermore, strong Fabry-Perot resonance fringes are present at high N*/III flux ratios, but become successively weaker at lower N*/III flux ratios. The increased luminescence intensity (i.e. luminescence efficiency) suggests an improved optical quality of the superlattice samples. Lastly, more prominent Fabry-Perot fringes suggest the presence of sharper, more homogeneous interfaces between the InGaN and GaN layers.

Further insight into the effects of growth conditions on the optical quality of these samples can be gained by considering the effects of growth temperature as well as incident N*/III flux ratio. Figure 3.13 on p. 105 presents a perspective of the optical quality of these superlattice samples as a function of both substrate temperature and incident N*/III flux ratio. The figure shows a matrix of PL spectra with columns representing variations in substrate temperature (increasing to the left) and rows representing incident N*/III flux ratio (increasing towards higher rows). From this figure, it is clear that the PL spectra rapidly degrade (i.e. the optical quality degrades) for samples grown below the critical temperature T_C regardless of the incident N*/III flux ratio. This strongly suggests that in this temperature regime there is insufficient mobility of species on the surface for the necessary self-ordering to occur; hence, the optical quality of this material is very poor. Furthermore, the figure indicates that for growth temperatures above T_C, the luminescence efficiency improves, suggesting that higher mobilities of species at the surface provides for improved long-range ordering and a higher optical quality.

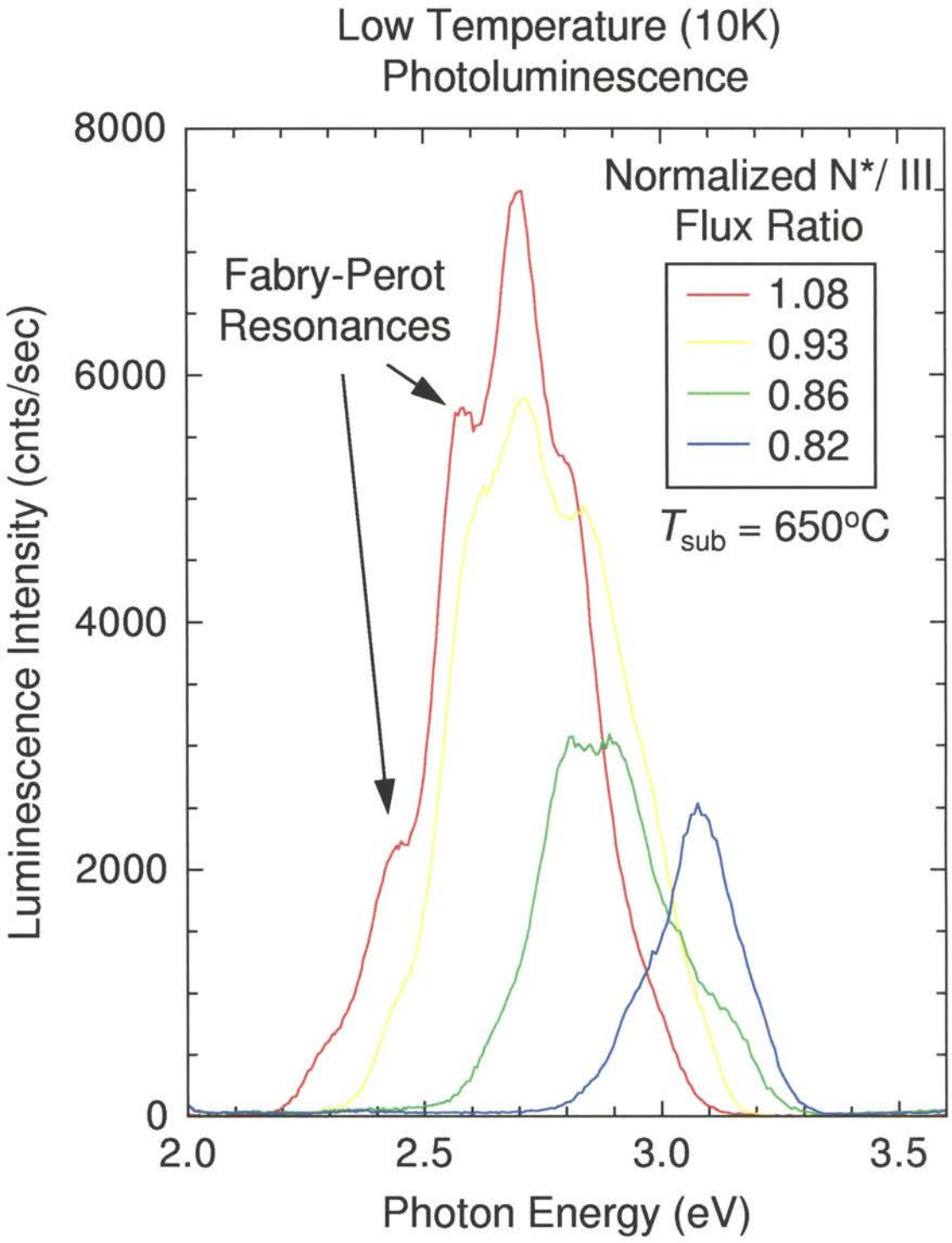

Figure 3.12. Effect of N*/III flux ratio on low temperature PL spectra. Peak positions red-shift when grown with increasing N*/III flux ratio. Additionally, there is an overall loss of PL intensity and decay of Fabry-Perot resonances at lower N*/III flux ratios.

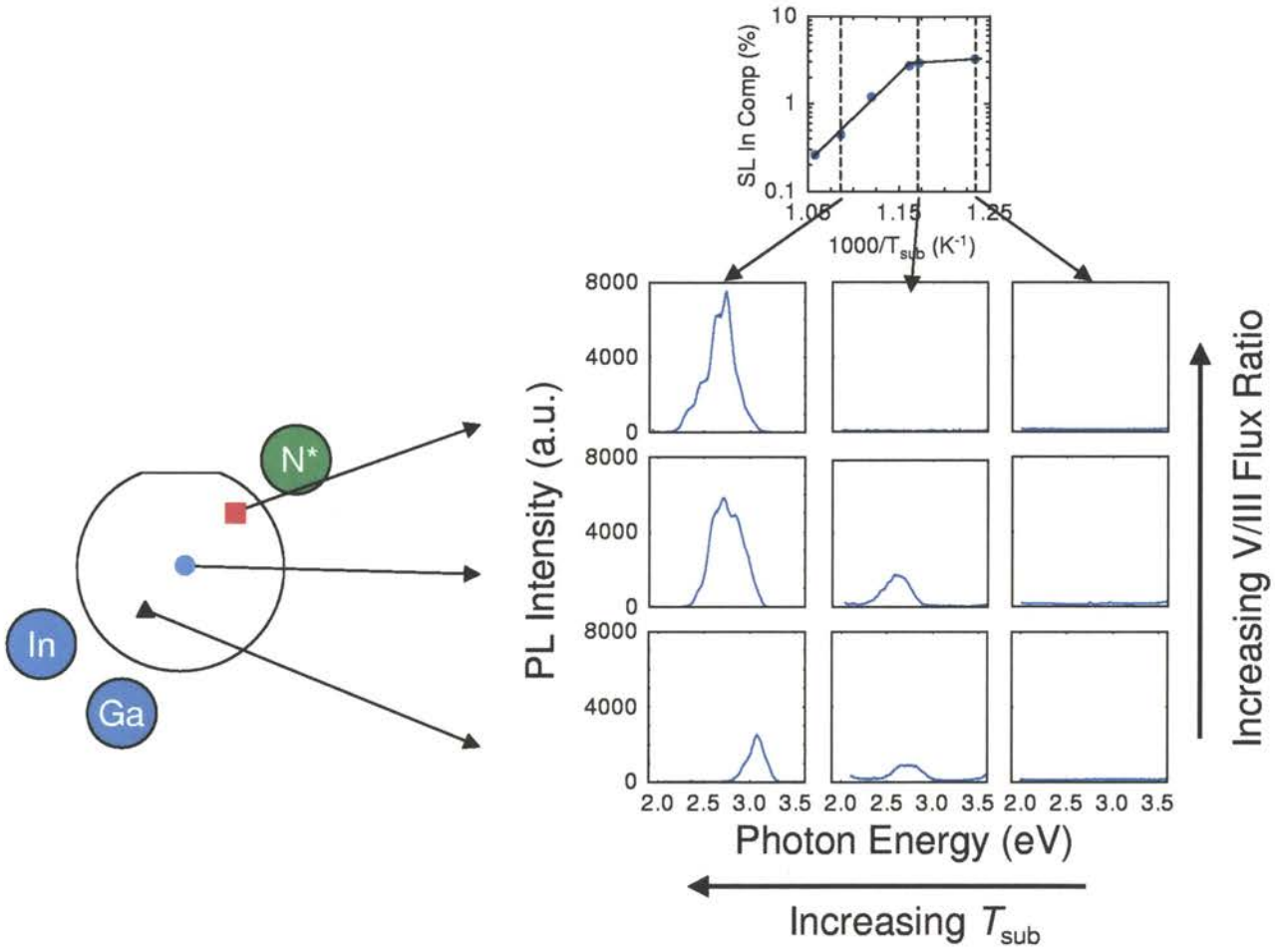

Figure 3.13. Matrix of PL spectra as a function of substrate temperature and incident N*/III flux ratio. Spectra are observed to improve with increasing substrate temperature and incident N*/III flux ratio (see text). Additionally, PL peak positions are observed to red-shift with increasing N*/III flux ratio or decreasing substrate temperature.

In addition to the variation in PL peak position as a function of incident N*/III flux ratio, Fig. 3.13 also reveals a variation in PL peak position as a function of substrate temperature. Rows of spectra in the figure (i.e. for growth at a constant N*/III flux ratio) reveal that the PL peak positions are blue-shifted with increasing substrate temperature. This is again consistent with HRXRD measurements and the results expected from the proposed surface-segregation/surface-desorption mechanism for In reduction at high temperatures.

To more clearly illustrate the dependence of the PL peak position on the growth conditions, Figs. 3.14(a)–(b) on p. 107 show plots of the PL peak position as a function of (a) the substrate temperature and (b) the incident N*/III flux ratio. As can be seen in the figure, the functional dependence of the PL peak position is not simple, and a quantitative model would be required to describe it. It is worth noting that while the trends in the PL peak positions are in excellent agreement with the other results and expectations, the observed PL peaks typically appear at lower energies than expected based on calculations using the known band-bowing parameters[48] and In compositions determined from HRXRD measurements. This suggests that there are significant compositional fluctuations within the InGaN layers.

3.4 Summary and Conclusions

This chapter began with a discussion of the importance of InN and the InGaN material system. Briefly, InN has a wide, direct bandgap, and like GaN, is thermally, mechanically, and chemically robust. The bandgaps of GaN and InN are 3.4 eV and 1.9 eV, respectively at room temperature. In principle, InGaN alloys could be grown with bandgaps that span the entire visible range of wavelengths. Because of this, InGaN alloys are currently being heavily pursued for potential applications as LEDs, laser diodes, and optical sensors.

In the research presented in this chapter, InGaN/GaN heterostructures were grown by RF plasma-assisted molecular beam epitaxy. The purpose of this study was to understand and quantitatively assess the relevant growth phenomenology and to

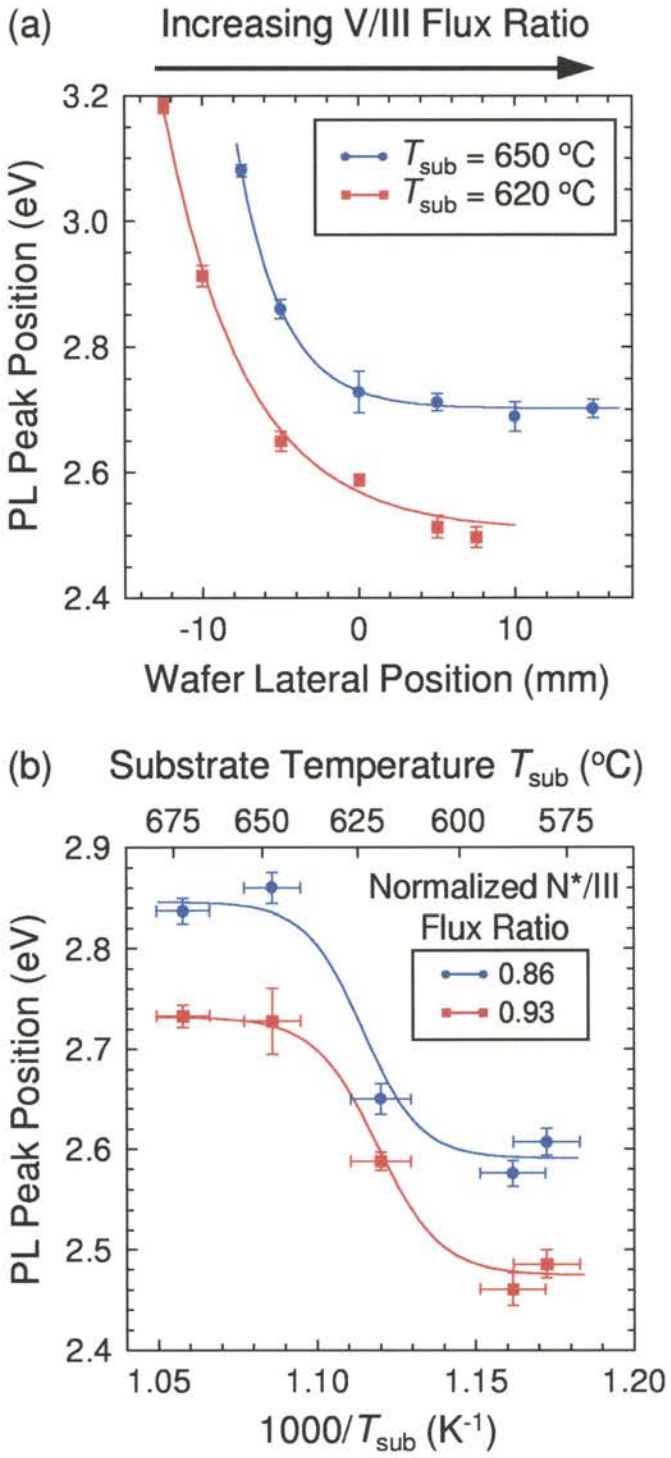

Figure 3.14. Effect of (a) substrate temperature and (b) N*/III flux ratio on PL peak position. The trends of the PL peak position to red-shift with decreasing substrate temperature or increasing N*/III flux ratio are in agreement with HRXRD results and that which would be expected from the surface-segregation/surface-desorption interpretation.

determine the effects of the relevant growth parameters on the resultant quality of the material.

Incident-flux-dependent studies revealed the relevant growth phenomenology. In particular, it was observed that the growth of the superlattices could be limited either by the arrival-rate of the incident metal flux or by the arrival-rate of the incident N* flux. Furthermore, it was observed that a higher N*/III flux ratio was needed to grow the InGaN/GaN superlattices than to grow a GaN epilayer. Lastly, it was observed that the maximum in the InN effective growth rate always occurred at a higher N*/III flux ratio that the GaN effective growth rate, implying that InN requires a higher N*/III flux ratio than GaN for stoichiometric growth.

Temperature-dependent studies demonstrated that the rate of In incorporation into the samples is strongly affected by both the growth temperature and the incident N*/III flux ratio. At a fixed incident N*/III flux ratio, two temperature regimes were identified in the growth of the superlattices. Firstly, at temperatures lower than some critical temperature T_C, the average In composition is effectively constant, suggesting that the average In composition was determined by the arrival-rate of the incident metal fluxes at these temperatures. Secondly, at temperatures above T_C, the average In composition decreased by more than an order-of-magnitude in the temperature range 590–670 °C. Furthermore, for samples grown at temperatures above T_C, the average In composition was strongly affected by the incident N*/III flux ratio. An order-of-magnitude increase in the average In composition was observed at the highest temperatures of this study despite only a 20% increase in the N*/III flux ratio.

The physical mechanism for the reduced In incorporation observed at high growth temperatures was attributed to In surface-segregation in combination with In surface-desorption. It was proposed that the dependence on the incident N*/III flux ratio was due to changes in the surface concentration of N. It was suggested that an increased N surface concentration could increase the In incorporation by (1) increasing the surface residency time of In adatoms, and (2) reducing the rate of In surface-segregation (i.e. reducing the rate of Ga-for-In cation exchanges through (*i*)

a reduced Ga surface concentration and (*ii*) a reduced mobility of Ga adatoms). Further support for the In surface-segregation/surface-desorption assessment of the In reduction mechanism was provided by the RHEED patterns. In this case, the more specular RHEED patterns observed during the InGaN layer deposition were observed to persist longer following the InGaN layer deposition at higher growth temperatures.

Lastly, low temperature PL results were consistent with the proposed In surface-segregation/surface-desorption mechanism and provided insight into the effect of the growth conditions on the optical quality of the InGaN/GaN superlattices. First, the observed changes in the PL peak positions associated with changes in either substrate temperature or incident N*/III flux ratio are consistent with HRXRD results and the surface-segregation/surface-desorption interpretation. At temperatures below T_C, the optical quality of these samples (as assessed by PL intensity) was poor regardless of the incident N*/III flux ratio. At growth temperatures above T_C, the optical quality of the samples were observed to systematically improve with increases in either substrate temperature or incident N*/III flux ratio (over the ranges used in this study).

The above results may have possible implications for the growth of InGaN alloy layers for device applications. One approach to obtaining InGaN alloy layers has been to use a low substrate temperature during growth. Alternatively, it may be possible to obtain InGaN alloy layers of the same In composition through the use of both higher growth temperatures and incident N*/III flux ratios. The PL results suggest this could result in an improved optical quality. Additionally, a higher N*/III flux ratio could be utilized to control In segregation and facilitate sharper interfaces at heterojunctions.

CHAPTER 4

SUMMARY AND CONCLUSIONS

In summary, InN, GaN, and AlN are wide, direct bandgap semiconductors with prospects in a multitude of optical, optoelectronic, and electronic applications. Commercially viable light emitting diodes (LEDs) and laser diodes based on these materials have already been realized. Most of the early successes in the growth of devices based on the nitrides have come from materials grown by metalorganic chemical vapor deposition (MOCVD) rather than by molecular beam epitaxy (MBE). While MOCVD has demonstrated early success in growing materials of sufficient quality for some device applications, the MOCVD growth technique cannot control layer thicknesses and alloy layer compositions with the same precision as the MBE growth technique. In order to grow devices that are highly sensitive to epilayer thicknesses, it is necessary to develop suitable techniques and methodologies for MBE growth of these materials. The work presented in this thesis represents significant progress towards this goal. Through the research presented in this thesis, an understanding of the growth of GaN epilayers and InGaN/GaN superlattice structures has been attained.

The growth of GaN by RF plasma-assisted molecular beam epitaxy (RF-MBE) was discussed in Chapter 2. In this chapter, the growth phenomenology was discussed in detail. For the growth of GaN on Al_2O_3 substrates, two different buffer layers were discussed. It was found that nitriding the Al_2O_3 surface to form an AlN layer resulted in a sufficient template for epitaxial overgrowth with GaN epilayers. Additionally, it was found that GaN buffer layers grown at low substrate temperatures did not improve the crystallographic quality of subsequently deposited GaN epilayers; in fact, it was found that these buffers can be extremely deleterious to the crystallographic quality of the GaN epilayers. For the growth of GaN epilayers, it was found that the most important growth parameters are the (1) substrate temperature, (2) incident N*/Ga

flux ratio, and (3) GaN growth rate. The effects of these growth conditions on the growth phenomenology were discussed in detail. In particular, it was found that the incident N*/Ga flux ratio must be used to maintain stoichiometric growth conditions to (1) prevent the onset of three-dimensional growth, (2) prevent saturation of the growth surface with excess Ga metal, and (3) optimize the crystallographic quality the GaN epilayers. Additionally, it was shown that the substrate temperatures used during growth must be sufficiently high to facilitate the formation of the GaN crystal, but must also be kept sufficiently low to prevent three-dimensional growth. Lastly, an interpretation was presented for the effects of these growth parameters on the microscopic growth processes occurring during GaN deposition. It was found that all of the observed growth results could be interpreted in terms of the proposed microscopic growth processes. This interpretation of the surface growth physics was then later useful in understanding the growth of InGaN/GaN superlattices.

The growth of InGaN/GaN superlattices was discussed in Chapter 3. A study of the effect of the incident fluxes suggested that InN requires a higher N*/III flux ratio ratio than does GaN for stoichiometric growth. Additionally, the effects of both the substrate temperature and incident N*/III flux ratio on the In incorporation efficiency of the superlattice samples were studied. High resolution X-ray diffraction measurements revealed two regimes in the substrate temperature dependence of the average superlattice In compositions. At temperatures below approximately 590 °C, the average In composition of the superlattices is nominally constant and is determined by the incident In/Ga flux ratio. However, in the narrow temperature range 590–670 °C, more than an order-of-magnitude decrease in the In incorporation efficiency was observed (at the lowest N*/Ga flux ratio of this study). Additionally, the incident N*/III flux ratio was observed to strongly influence the In incorporation of the superlattice samples. Nearly an order-of-magnitude increase in the In composition was observed at the highest temperature of this study despite only an approximately 20% increase in the N*/III flux ratio. The reduction of incorporated In at high growth

temperatures was attributed to thermally-activated surface-segregation and surface-desorption of In. Lastly, the RHEED patterns observed during growth and the low temperature PL measurements both were in good agreement with this assessment.

The research presented in this thesis has implications for GaN and InGaN epilayers grown by RF-MBE for device applications. Firstly, the identification of the most important growth parameters and the effects of these growth parameters on epilayer quality is a key step in growing high quality GaN epilayers for devices. Secondly, understanding the InGaN growth phenomenology is critical in optimizing the growth process to obtain high quality InGaN epilayers and InGaN/GaN superlattices. Additionally, a detailed understanding of the underlying microscopic growth processes, and the effects of growth parameter variations on these processes, will greatly simplify the optimization of epitaxial films. Lastly, as discussed in Chapter 3, the low-temperature PL results for the InGaN/GaN superlattice samples suggest new strategies for attaining InGaN/GaN superlattices with an improved optical quality. Specifically, it was suggested that InGaN/GaN superlattices be grown at higher substrates temperatures using a higher N*/III flux ratio to improve the optical quality, incorporation of In, and interface sharpness.

BIBLIOGRAPHY

1. Gil, B., *Group III Nitride Semiconductor Compounds*, (Clarendon Press, Oxford, 1998).

2. Pankove, J. I., and Moustakas, T. D., *Gallium Nitride (GaN) I: Semiconductors and Semimetals*, Vol. 50, (Academic Press, San Diego, 1998).

3. R. J. Hauenstein, in *Thin Films: Heteroepitaxial Systems*, edited by W. K. Liu and M. B. Santos (World Scientific Publishing, Singapore, 1999), Chap. 11, and references therein.

4. S. Nakamura, M. Senoh, S. Nagahama, N. Iwasa, T. Yamada, T. Matsushita, H. Kiyoku, and Y. Sugimoto, Jpn. J. Appl. Phys. **35**, L74 (1996).

5. S. Nakamura, M. Senoh, S. Nagahama, N. Iwasa, T. Yamada, T. Matsushita, H. Kiyoku, and Y. Sugimoto, Jpn. J. Appl. Phys. **35** L217, (1996).

6. S. Nakamura, M. Senoh, S. Nagahama, N. Iwasa, T. Yamada, T. Matsushita, H. Kiyoku, and Y. Sugimoto, Appl. Phys. Lett. **68**, 2105 (1996).

7. S. Nakamura, M. Senoh, S. Nagahama, N. Iwasa, T. Yamada, T. Matsushita, H. Kiyoku, and Y. Sugimoto, Appl. Phys. Lett. **68**, 3269 (1996).

8. S. Nakamura, M. Senoh, S. Nagahama, N. Iwasa, T. Yamada, T. Matsushita, Y. Sugimoto, and H. Kiyoku, Appl. Phys. Lett. **69**, 1568 (1996).

9. I. Akasaki, S. Sota, H. Sakai, T. Tanaka, M. Koike, and H. Amano, Electron. Lett. **32**, 1105 (1996).

10. S. Nakamura, M. Senoh, S. Nagahama, N. Iwasa, T. Yamada, T. Matsushita, Y. Sugimoto, and H. Kiyoku, Appl. Phys. Lett. **69**, 3034 (1996).

11. K. Itaya, M. Onomura, J. Hishio, L. Sugiura, S. Saito, M. Suzuki, J. Rennie, S. Nunoue, M. Yamamoto, H. Fujimoto, Y. Kokubun, Y. Ohba, G. Hatakoshi, and M. Ishikawa, Jpn. J. Appl. Phys. **35**, L1315 (1996).

12. S. Nakamura, M. Senoh, S. Nagahama, N. Iwasa, T. Yamada, T. Matsushita, Y. Sugimoto, and H. Kiyoku, Appl. Phys. Lett. **69**, 4056 (1996).

13. S. Nakamura, M. Senoh, S. Nagahama, N. Iwasa, T. Yamada, T. Matsushita, Y. Sugimoto, and H. Kiyoku, Appl. Phys. Lett. **70**, 868 (1997).

14. S. Nakamura, M. Senoh, S. Nagahama, N. Iwasa, T. Yamada, T. Matsushita, Y. Sugimoto, and H. Kiyoku, Appl. Phys. Lett. **70**, 1417 (1997).

15. S. Nakamura, M. Senoh, S. Nagahama, N. Iwasa, T. Yamada, T. Matsushita, Y. Sugimoto, and H. Kiyoku, Appl. Phys. Lett. **70**, 2753 (1997).

16. S. Nakamura, MRS Internet J. Nitride Semicond. Res. **2**, 5 (1997).

17. G. E. Bulman, K. Doverspike, S. T. Sheppard, T. W. Weeks, H. S. Kong, H. M. Dieringer, J. A. Edmond, J. D. Brown, J. T. Swindell, and J. F. Schetzina, Electron. Lett. **33**, 1556 (1997).

18. Cree Inc, Press release from PR Newswire on July 29 (1997).

19. S. Nakamura, M. Senoh, S. Nagahama, N. Iwasa, T. Yamada, T. Matsushita, H. Kiyoku, Y. Sugimoto, T. Kozaki, H. Umemoto, M. Sano, and K. Chocho, Appl. Phys. Lett. **72**, 211 (1998).

20. M. P. Mack, A. Abare, M. Aizcorbe, P. Kozodoy, S. Keller, U. K. Mishra, L Coldren, and S. DenBaars, MRS Internet J. Nitride Semicond. Res. **2**, 41 (1997).

21. A. Kuramata, K. Domen, and T. Tanahashi, Appl. Phys. Lett. **72**, 1359 (1998); oral presentation at ICNS, Tokushima, Japan (1997).

22. F. Nakamura, oral presentation at ICNS, Tokushima, Japan (1997).

23. S. Nakamura, oral presentation at MRS Fall Meeting, Boston, USA (1997).

24. S. Bidnyk, Ph.D. Thesis, Oklahoma State University, 1998.

25. Parker, E. H. C., *The Technology and Physics of Molecular Beam Epitaxy*, (Plenum Press, London, 1985).

26. Böer, K. W., *Survey of Semiconductor Physics*, Vol. 2, (Van Nostrand Reinhold, New York, 1992).

27. Rutner, E., Goldfinger, P., Hirth, J. P., *Condensation and Evaporation of Solids*, (Gordon and Breach, New York, 1964).

28. Petrucci, R., H., *General Chemistry, Principles and Modern Applications*, (Macmillan Publishing, New york, fifth edition, 1985).

29. M. L. O'Steen, M.S. Thesis, Oklahoma State University, 1995.

30. *Product and Vacuum Technology Reference Book*, (Leybold-Inficon, 1995).

31. R. J. Hauenstein, (private communication).

32. Kittel, C; *Introduction to Solid State Physics*, (John Wiley & Sons, Inc., New York, third edition, 1966).

33. Wang, Z. L., *Reflection Electron Microscopy and Spectroscopy for Surface Analysis*, (Cambridge, New York, 1996).

34. M. L. O'Steen, "X-Ray Diffraction Characterization of Epitaxial Thin Films", unpublished, and references therein.

35. Ashcroft, N. W., Mermin, N. D., *Solid State Physics*, (Holt, Rinehart, and Winston, New York, 1976).

36. Kittel, C; *Introduction to Solid State Physics*, (John Wiley & Sons, Inc., New York, sixth edition 1986).

37. Cullity, B. D.; *Elements of X-Ray Diffraction*, (Addison- Wesley, Reading, Mass., Second Edition, 1956).

38. F. Fedler, M.S. Thesis, Oklahoma State University, 1998.

39. A. Krost, G. Bauer, J. Woitok, in *Optical Characterization of Epitaxial Semiconductor Layers*, edited by G. Bauer and W. Richter (Springer-Verlag, Berlin, 1996), Chap. 6.

40. Pankove, J. I., *Optical Processes in Semiconductors*, (Dover, New York, 1971).

41. Yu, P. Y., Cardona, M., *Fundamentals of Semiconductors*, (Springer-Verlag, New York, 1995).

42. N. Grandjean, and Massies, J., Appl. Phys. Lett. **71**, 13 (1997).

43. Y. Moriyaso, H. Goto, N. Kuze, and M. Matsui, J. Cryst. Growth. 150, 916 (1995).

44. D. Schikora, M. Hankeln, D. J. As, K. Lischka, T. Litz, A. Waag, T. Buhrow, and F. Henneburger, Phys. Rev. B **54**, R8381 (1996).

45. O. Brandt, H. Yang, B. Jenichen, Y. Suzuki, L. Däweritz, and K. H. Ploog, Phys. Rev. B **52**, R2253 (1995).

46. H. Yang, O. Brandt, M. Wassermeier, J. Behrend,H. P. Schönherr and K. H. Ploog, Appl. Phys. Lett. **68**, 244 (1996).

47. J. R. Müllhäuser, O. Brandt, A. Trampert, B. Jenichen, and K. H. Ploog, Appl. Phys. Lett. **73**, 1230 (1998).

48. M. D. McCluskey, C. G. Van de Walle, C. P. Master, L. T. Romano, and N. M. Johnson, Appl. Phys. Lett. **72**, 2725 (1998).

49. Kernighan, B. W., Ritchie, D. M., *The C Programming Language*, (Prentice Hall Inc., New Jersey, second edition, 1988).

APPENDICES

APPENDIX A

CONSTRUCTION AND MODIFICATION OF EXPERIMENTAL SYSTEMS

This appendix will discuss experimental systems that were either constructed or modified and for which there is no documentation elsewhere. Specifically, a spatially-resolved reflectance spectroscopy system was constructed to measure layer thicknesses of simple epilayer samples. Additionally, extensive modifications have been made to implement computerized monitoring of the MBE system.

A.1 Spatially-Resolved Reflectance Measurement

In MBE growth, it is essential to know the rate at which material is deposited under varying growth conditions. For many material systems, MBE growth rates can be measured directly through the study of RHEED oscillations.[25] In the case of plasma-assisted MBE growth of GaN, RHEED oscillations are only observed under growth conditions that are far from optimal. Consequently, alternative methods are necessary to correlate growth rates with growth conditions. As an alternative, if the epilayer thickness can be measured separately, then the growth rate may be determined by dividing the epilayer thickness by the known deposition time.

Reflectance spectroscopy measurements are commonly used to measure epitaxial layer thicknesses. The advantages of the reflectance measurement include being non-destructive, accurate, and simple enough to measure numerous points on a sample expeditiously. Because of the MBE growth geometry used in GaN epilayer growth (shown in Fig. 2.1(b) on p. 39), it is useful to make multiple thickness measurements

across the wafer surface. By doing so, the effects of small variations in the incident N*/Ga flux ratio can be studied.

In the reflectance measurement, an incident beam of light is partially reflected from the front and back surfaces of the epilayer. Partial destructive interference occurs due to the path difference of the two beams. The reflectance measurement geometry is shown in Fig. A.1 on p. 120. The epilayer thickness may be determined by considering the intensity variation of the reflected beam as a function of wavelength. To treat this more rigorously, assume that a plane wave with electric field $\vec{E_1}$ is incident on the sample. The electric field for the wave reflected from the surface will again be $\vec{E_1}$. Let the field reflected from the back surface of the sample be $\vec{E_2}$. Now, $\vec{E_2}$ may be expressed as $\vec{E_2} = b\vec{E_1}e^{-i\delta}$, where b is a constant accounting for the effect of the transmission and reflection coefficients at the GaN front and back surfaces, respectively, and δ is the phase difference between $\vec{E_1}$ and $\vec{E_2}$. The phase difference δ may be expressed as $\delta = k\Delta + \frac{\pi}{2} = \frac{2\pi}{\lambda}(2nt) + \frac{\pi}{2}$, where k is the wave vector, Δ is the optical thickness, λ is the wavelength, n is the GaN index of refraction, and t is the GaN layer thickness; the $\frac{\pi}{2}$ term in δ is due to a phase change at the GaN/sapphire interface. Finally, the intensity of the reflected beam is proportional to the square of the net electric field; it is straightforward to show that:

$$I_{\text{refl}} \propto [1 + b^2 + 2b\cos(\frac{4\pi}{\lambda}nt + \frac{\pi}{2})]E_1^2 \quad . \tag{A.1}$$

In order to facilitate acquiring reflectance data from multiple positions on a sample, the reflectance experiment was constructed using a microscope with an XY translation stage, as shown in Fig. A.2 on p. 121. The microscope camera port has been adapted to allow an optical fiber to illuminate the sample. The microscope objective lens serves to focus the incident light on the sample and to collect the reflected light. A second fiber collects light reflected from the sample via a small lens incorporated into the SMA termination. This second fiber then delivers the collected

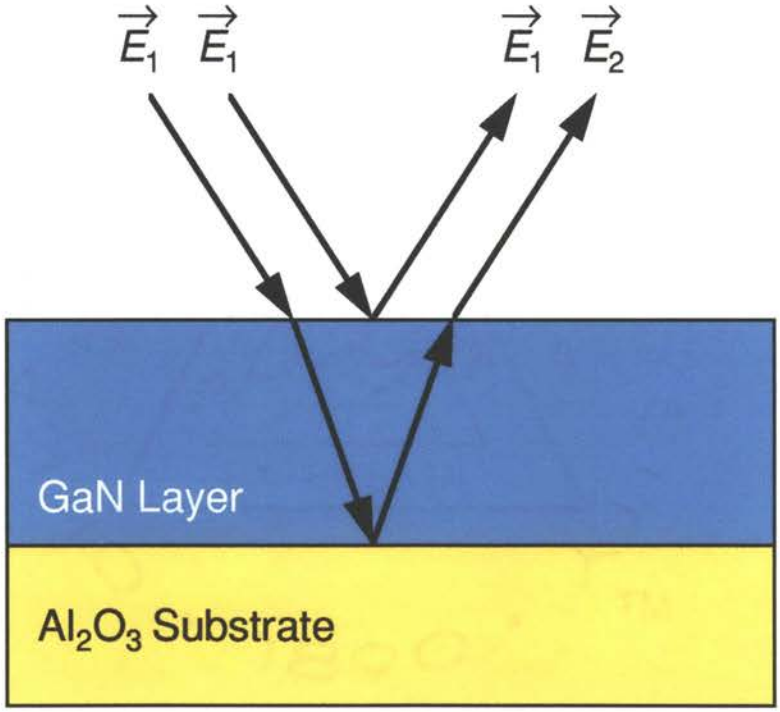

Figure A.1. Optical beam geometry for the reflectance measurement used to determine epilayer thicknesses. A difference in the optical path length results in interference of the beams reflected from the front and back surfaces of the GaN layer. This effect is utilized to measure epilayer thicknesses. The angle of the incident beam is exaggerated for clarity.

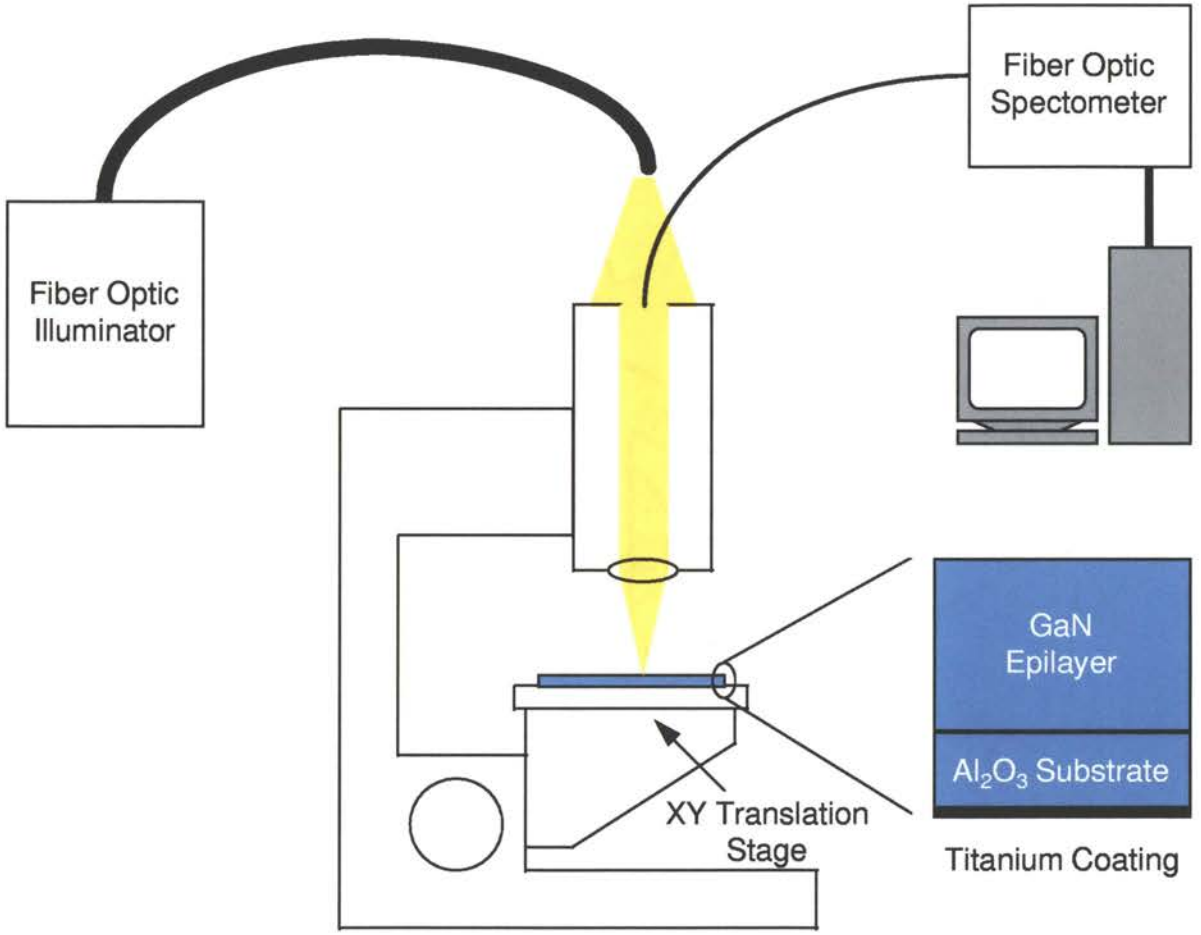

Figure A.2. The spatially-resolved reflectance spectroscopy experiment used for determining epilayer thicknesses is constructed using a standard laboratory microscope. Positioning of the sample with the XY translation allows reflectance spectroscopy measurements with a lateral resolution of approximately 1 mm. A microscope objective is used to focus light from a tungsten lamp on the sample. Reflected light is collected and delivered by an optical fiber to a spectrometer.

light to a spectrometer with approximately 1 nm spectral resolution. The XY translation stage allows positioning of the sample with approximately 1 mm resolution. A typical data set acquired using this experimental setup is shown in Fig. A.3(a) on p. 123. A data set is acquired from a bare Ti-backcoated sapphire wafer, for use as a reference for normalization, prior to acquiring data from a GaN sample. As can be seen in Fig. A.3(a), the intensity of reflected light from the GaN epilayer is generally greater than that from the sapphire wafer. There are two reasons for this to occur: Firstly, the greater difference in the indices of refraction of the GaN/air interface vs. the sapphire/air interface results in a higher reflection constant. Secondly, the MBE grown epilayer is generally microscopically smoother than the commercially prepared sapphire wafer. The reflectance of the GaN epilayer, normalized to the sapphire substrate, is obtained by dividing the GaN intensity data point-by-point by the sapphire reference data. Again, the result shown in Fig. A.3(b) is typical. Finally, the thickness of the epilayer t may be determined by fitting the reflectance data with a function of the form:

$$R = R_0 + R_1 \cos\left(\frac{4\pi}{\lambda} nt + \phi\right) \quad , \tag{A.2}$$

where the GaN index of refraction n is taken to be 2.3.[2] The justification of this functional form follows directly from Eq. A.1, with some degree of parameterization to allow for deviations of the experiment from the ideal case. It is worth noting that there are constraints on the experiment. First, assuming a constant index of refraction $n = 2.3$ requires using a spectral region well below the bandgap to avoid anomalous dispersion. Secondly, the spectral range on the light source, a tungsten lamp in this case, must be free of a significant component with energies above the bandgap of the GaN to avoid causing photoluminescence or inducing changes in the optical properties of the sample.

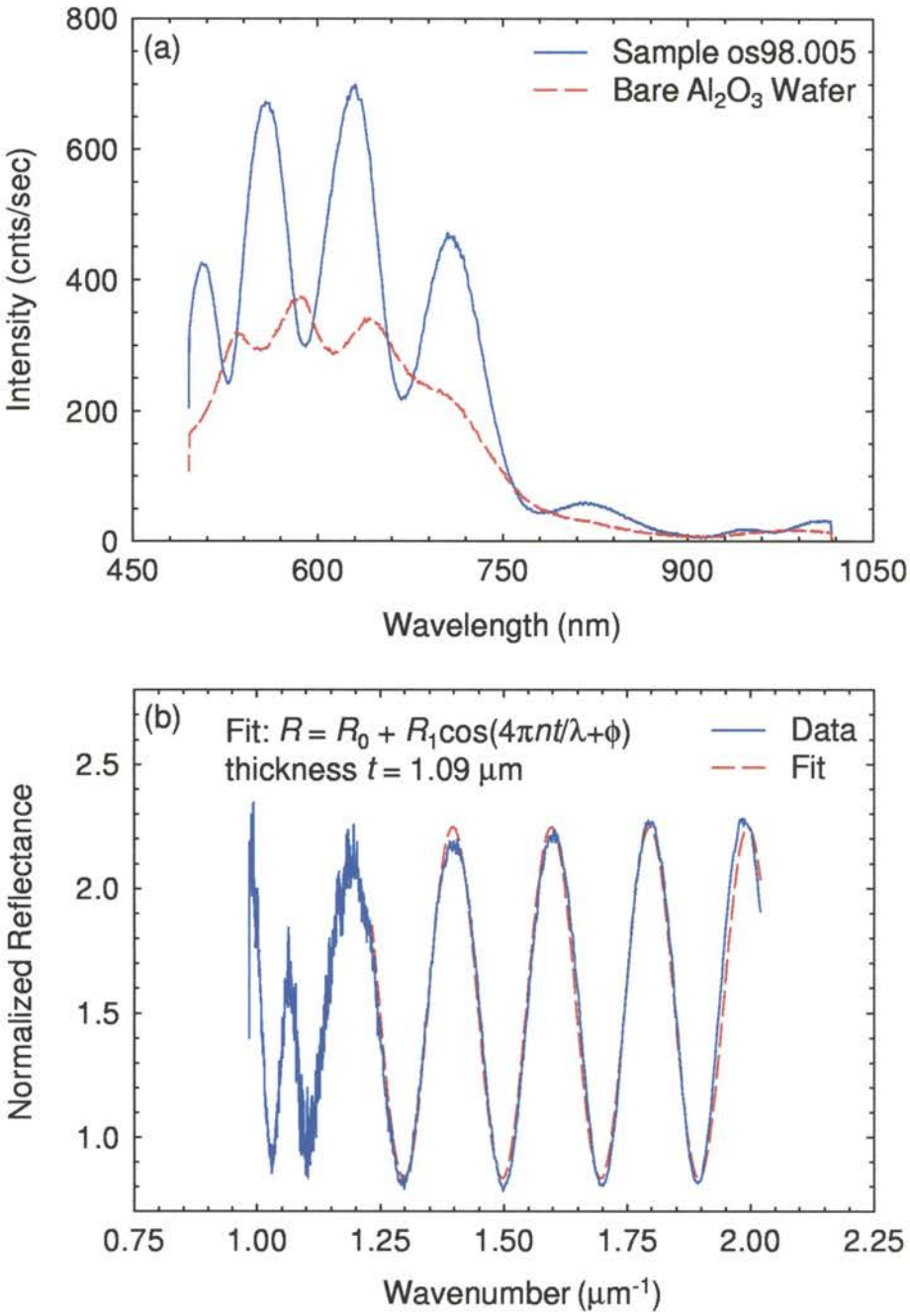

Figure A.3. Typical reflectance data from a 1.09 μm GaN epilayer deposited on a sapphire substrate. (a) Spectra obtained directly for a bare sapphire reference wafer and the GaN sample while illuminated with a tungsten lamp. (b) GaN epilayer reflectance normalized to the sapphire reference. The epilayer thickness is determined by fitting the data.

As mentioned previously, the above procedure is typically repeated for a number of points along the axis shown in Fig. A.1(a). Typical results of this are presented in Fig. A.4 on p. 125. In this particular example, significant variations in the epilayer thickness are observed across the sample. Epilayer thicknesses of 1.18 μm, 1.09 μm, and 0.92 μm are observed for regions of the sample near the N* plasma source, at the wafer center, and near the Ga source, respectively. The observed thickness variations are consistent with N* arrival-rate limited growth, as discussed in Chap. 2.

A.2 Computerized Monitoring of MBE Growth

The use of computers to automate data acquisition from the MBE system has increased by orders of magnitude the volume of data that can be recorded both during growth runs and while idle. This greatly enhances the ability to analyze, interpret, and understand MBE growth phenomenology, growth results, and system interactions. In short, automated acquisition of MBE system data greatly improves the quality and scope of the science that can be performed. Over approximately two years, automated data acquisition has been added for a number of key MBE growth parameters. In order to document the modifications to the MBE system and to simplify future changes, the details of the automated data acquisition will be discussed here.

Currently, a 486DX2-50 computer equipped with an IEEE-488 GPIB card is used to acquire data from nine instruments. The electronic bus connecting the instruments to the computer is illustrated in Fig. A.5 on p. 126. Two instruments are connected directly to the GPIB bus: the Residual Gas Analyzer (RGA) and a multichannel digital multimeter (DMM). Eight instrument are then monitored via analog signal lines by the DMM. The instruments monitored by the DMM are:

- Room temperature thermocouple
- Ion gauge controller

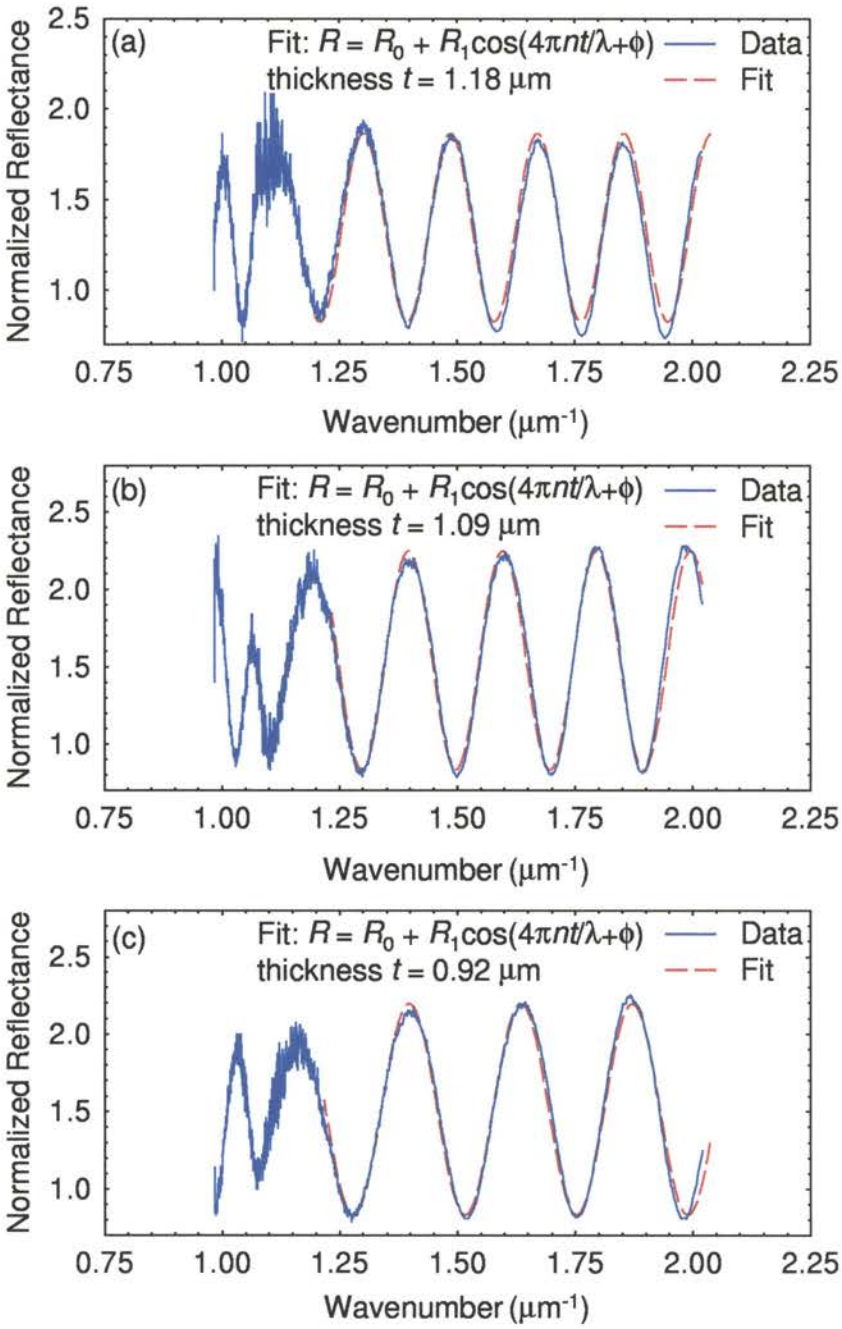

Figure A.4. Reflectance data acquired for several positions across sample os98.005. The measured film thicknesses 1.18 μm, 1.09 μm, and 0.92 μm correspond to positions (a) near the nitrogen source, (b) at the wafer center, and (c) near the Ga source, respectively.

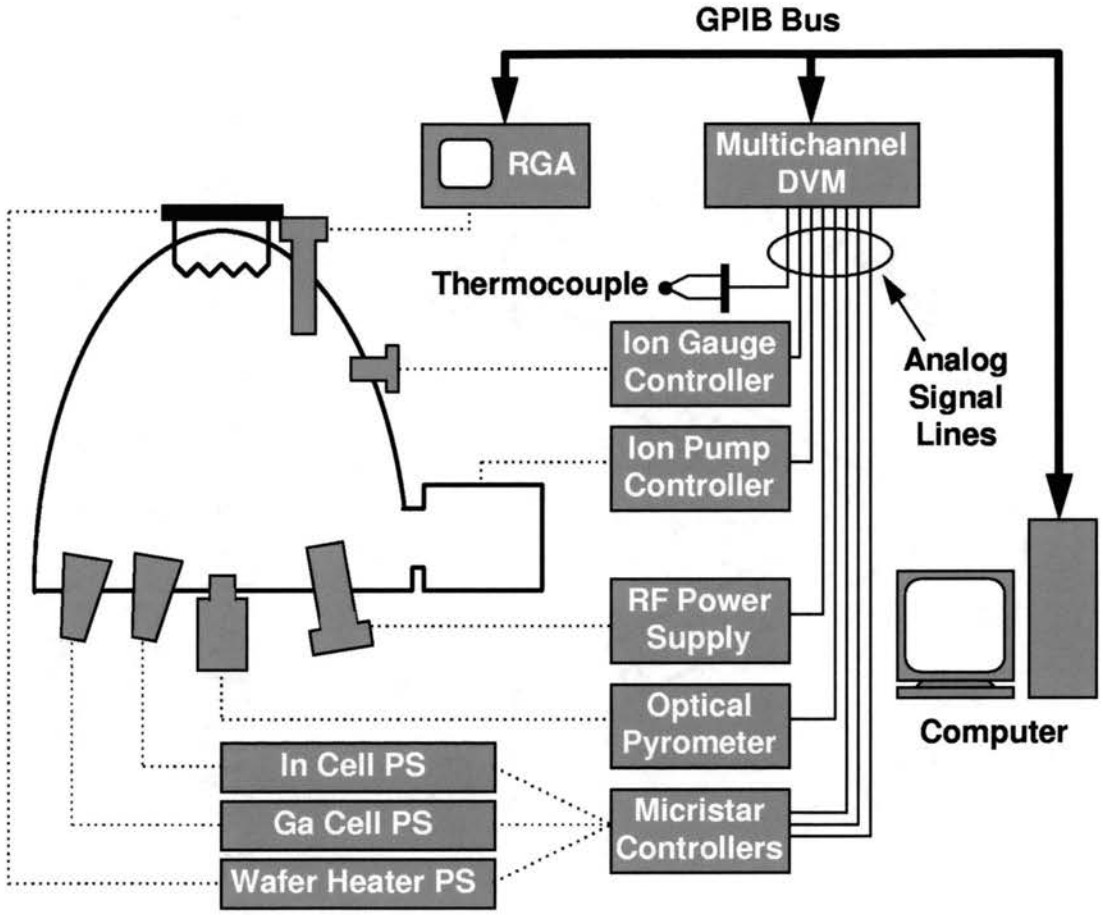

Figure A.5. Instruments and electronic bus used in automated acquisition of MBE data. The residual gas analyzer (RGA) and multichannel digital multimeter (DMM) are connected to the computer via the GPIB bus. The DMM is used to monitor analog signals from eight instruments. In total, nine MBE instruments are monitored.

- Ion pump controller
- RF power supply
- Optical pyrometer
- Micristar control voltages regulating the electrical power provided to the In and Ga effusion cells and the wafer stage heater.

An integrated cold junction compensator allows the DMM to directly interpret the DC voltage readings from the type-K thermocouple used to monitor the laboratory temperature. For this reason, temperature readings only are returned to the computer via the GPIB bus.* For the remaining instruments connected to the DMM, a DC voltage is measured and returned to the computer. Each voltage measurement can then be converted to reflect the corresponding growth parameter. The conversion method or scaling necessary for each instrument is easily found in its technical manuals and documentation. The connection of each instrument to the DMM and the scaling needed is summarized in Table. A.1 on p. 128.

In practice, the values obtained for growth parameters obtained by converting voltage readings according to the instructions in the documentation results in readings that deviate slightly from the values observed on the "front panel" of instruments. For this reason, it is necessary to calibrate the observed DC voltages against the correct readings from the instruments. This task is accomplished by a straight-forward fitting of the expected function to the observed data. Two examples of this are presented in Fig. A.6 and Fig. A.7. These two examples cover the two types of conversion that are necessary in this application: linear and exponential. In Fig. A.6 on p. 130, the In cell "% Output" is plotted against the control signal sent to the power supply that

*In order for the DMM to correctly interpret the type-K thermocouple, it must first be instructed, via computer programming, to read the integrated cold junction compensator.

Multimeter Channel	Instrument	Voltage Range	Data Range	Conversion Method
1	Cold Junction Compensator	N/A	N/A	N/A
2	Optical Pyrometer	0 - 100 mV	350 - 800 °C	Linear
3	Room Thermocouple	-6.5 - 25.3 mV	-270 - 610 °C	Automatic
4	RF Forward Power	0 - 5 V	0 - 600 Watts	Linear
5	Spare Micristar Channel	0 - 5 V	0 - 100 %	Linear
6	Ion Pump Controller	0 - -100 mV	10^{-9} - 10^{-4} Torr	Exponential
7	Ion Gauge Controller	0 - 10 V	10^{-10} - 10^{0} Torr	Exponential
8	In Cell	0 - 5 V	0 - 100 %	Linear
9	Wafer Stage Heater	0 - 5 V	0 - 100 %	Linear
10	Ga Cell	0 - 5 V	0 - 100 %	Linear

TABLE A.1. Shown is the connection of various instruments to the respective digital multimeter channels. Also shown are the voltage ranges of the analog signal lines, the corresponding data ranges, and the conversion methods necessary to convert DC voltage readings to growth parameter data.

heats the In cell. Physically, the % Output is the fraction of the maximum voltage the power supply can deliver that is applied to the cell. As expected, a strong linear relationship exists, however, the values of the slope and intercept deviate slightly from the expected values of 20 and 0, respectively. In the case of the Ion gauge controller, the output voltage is proportional to the logarithm of the pressure reading. Ideally, the output signal increases by 1 volt per decade increase in pressure. By plotting *log*[Pressure] vs. output signal, as shown in Fig. A.7 on p. 131, it is again shown that the observed data deviates slightly from the expected functional form. In both cases, correctly calibrated conversion equations are easily determined from the fit parameters.

A number of computer programs have been written to acquire data via the GPIB bus. Two programs are used particularly frequently and will be discussed here. Both programs utilize the C-programming libraries and Linux GPIB driver provided by `The Linux Lab Project`, managed by Clausi Shroeter of Freien Universität Berlin. The first program, called `rga_scan`, is used to obtain data from the residual gas analyzer (mass spectrometer) in the MBE system. Specifically, this program acquires the *saved* analog scan data stored in the system memory. This program allows a set of data, stored in the volatile memory of the RGA, to be moved to the computer at the convenience of the user. This is particularly useful since it reduces the exposure time of the RGA to molecular beams, thereby extending the life of the instrument. As is typical of UNIX commands, the program prints all information to standard output, which may be redirected by the user to a file. Header information is output first identifying the conditions of the scan; this includes the scan width, scan center, RGA gain, scan speed, and electron multiplier voltage. Following the header information, the scan data is printed in a two-column format with columns for the mass (actually

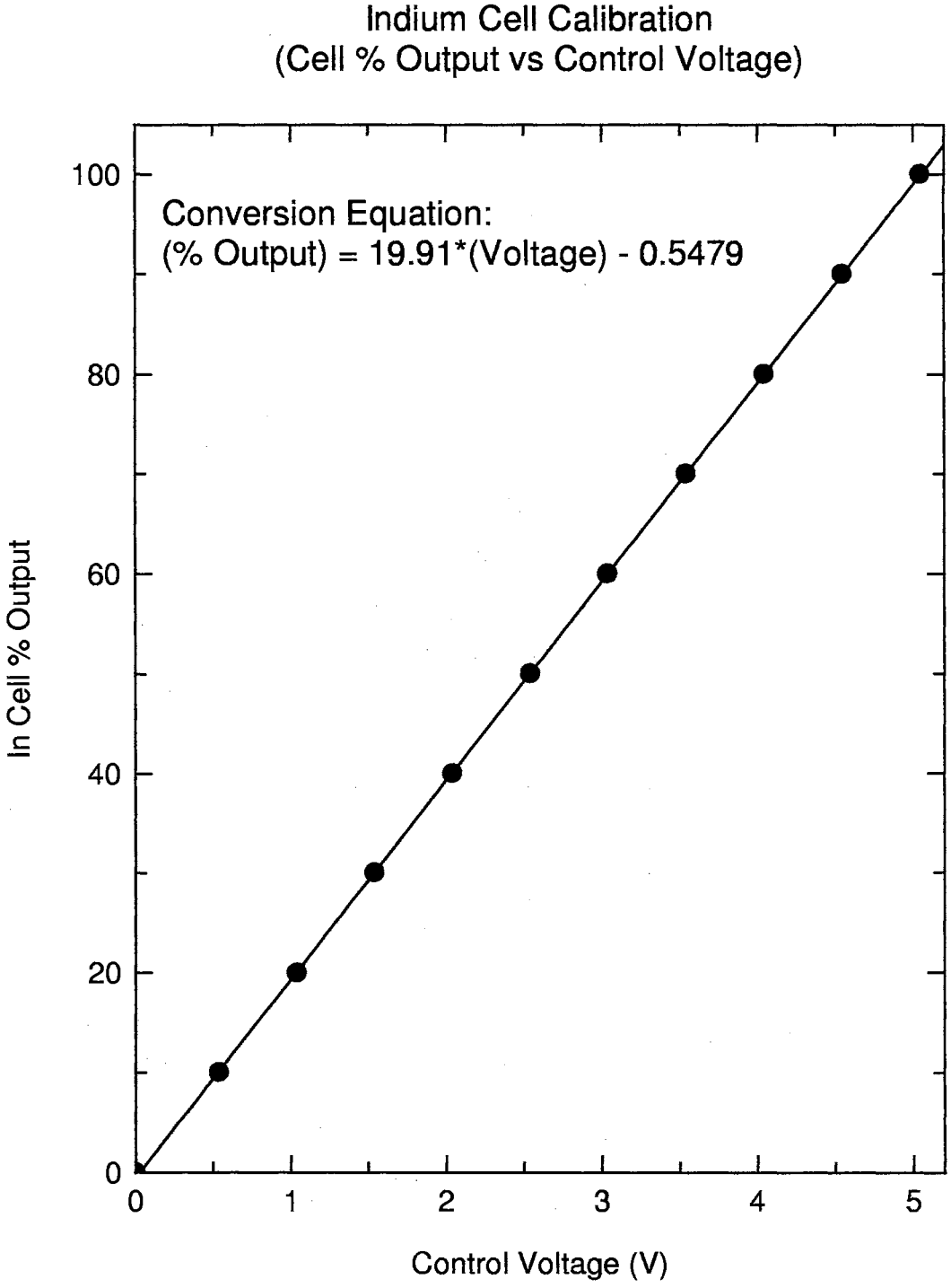

Figure A.6. Calibration of the output control voltage used to regulate the electrical power delivered to the In effusion cell. The "% Output" represents the fraction of the maximum voltage available from the power supply (25 V) that is applied to the cell. The slope and intercept values obtained by fitting the data deviate slightly from the expected values of 20 and 0, respectively.

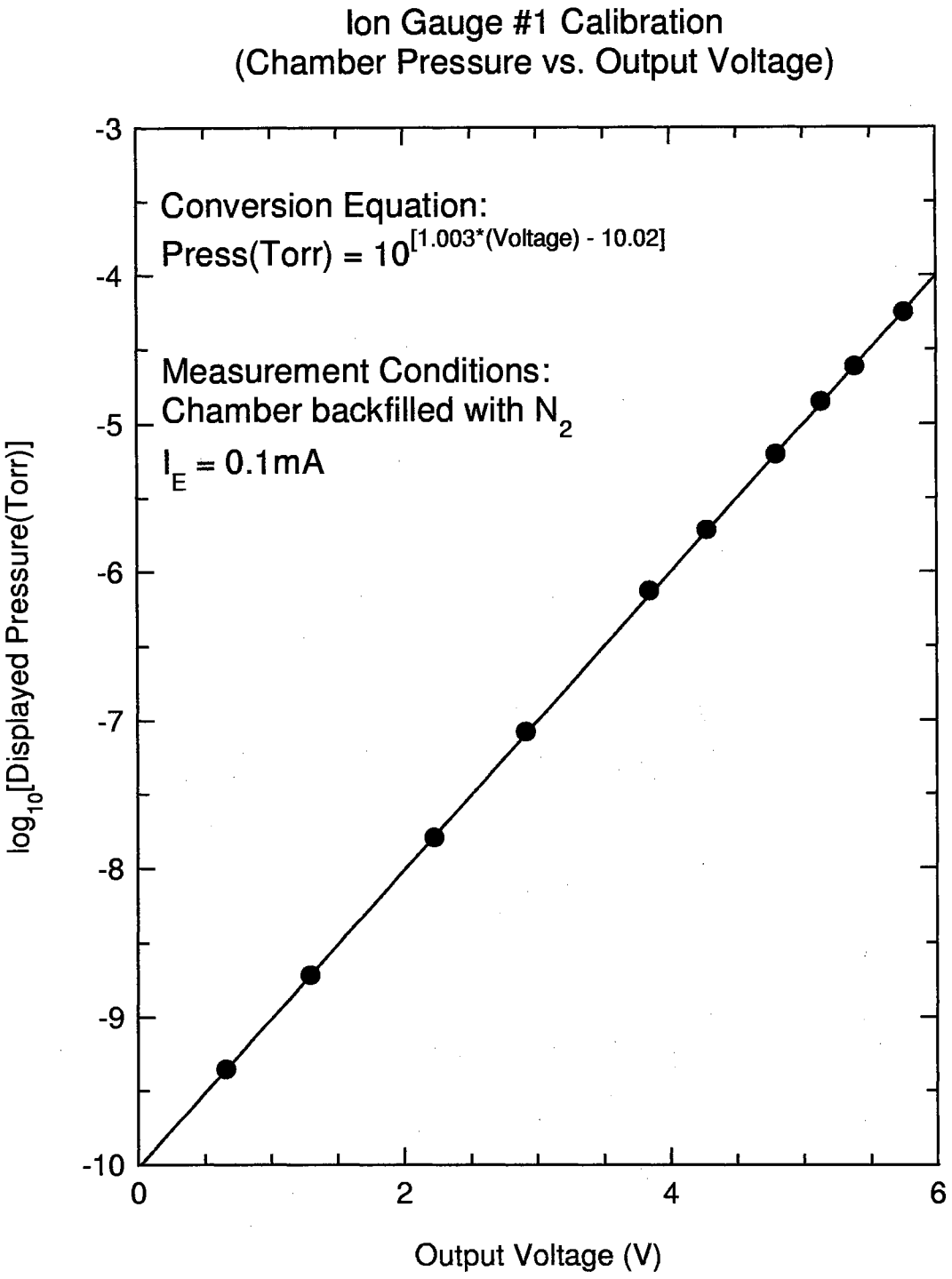

Figure A.7. Calibration of the ion gauge controller output signal. The output signal increases as the logarithm of the pressure. Calibration is performed while backfilling with ultra-high purity N_2 gas and with $I_{\text{Emission}} = 0.1\,\text{mA}$. Ideally, the output signal should increase by 1 volt per decade increase in pressure.

mass-to-charge ratio) and ion current. Here, the ion current is proportional to the partial pressure of the measured species.

The `rga_scan` program is typically used for measuring fluxes of molecular beams, either during growth runs or while calibrating effusion cell fluxes. An example of the usefulness of this program is shown in Fig. A.8 on p. 133. RGA data is shown for Ga flux measurements at several temperatures; peaks occurring at 69 and 71 amu are due to different isotopes of Ga. A more accurate measure of flux is obtained by integrating the RGA signal of a particular peak as opposed to using the peak amplitude. By integrating the RGA signal, the temperature dependence of Ga flux may be accurately calibrated via an Arrhenius plot, as shown in the inset of Fig. A.8.

The second program to be discussed is used to poll the various instruments connected to the channels of the DMM. Two versions of this program are used routinely: `mbe_status` and `mbe_scan`. The first version, `mbe_status` obtains voltage data from the DMM, converts it the corresponding MBE growth parameters, and prints the results to standard output. The second version, `mbe_scan`, performs the same functions with the exception that the data is stored in two files rather than being printed to standard output. The first of the two files receives the processed data; the second receives the raw voltage readings from the DMM. The files used by this program are provided as command line arguments. In the event that only one file name is provided, the program assumes the second file name will have the same root name as the first file and changes the final extension to `.raw`.

The action and output of both versions of this program are controlled by a system configuration file: `etc/mbe.conf`. The current `mbe.conf` file is shown in Fig. A.9 on p. 134. This configuration file is a simple text file composed of command lines, each describing a specific action that the `mbe_status` and `mbe_scan` programs are to

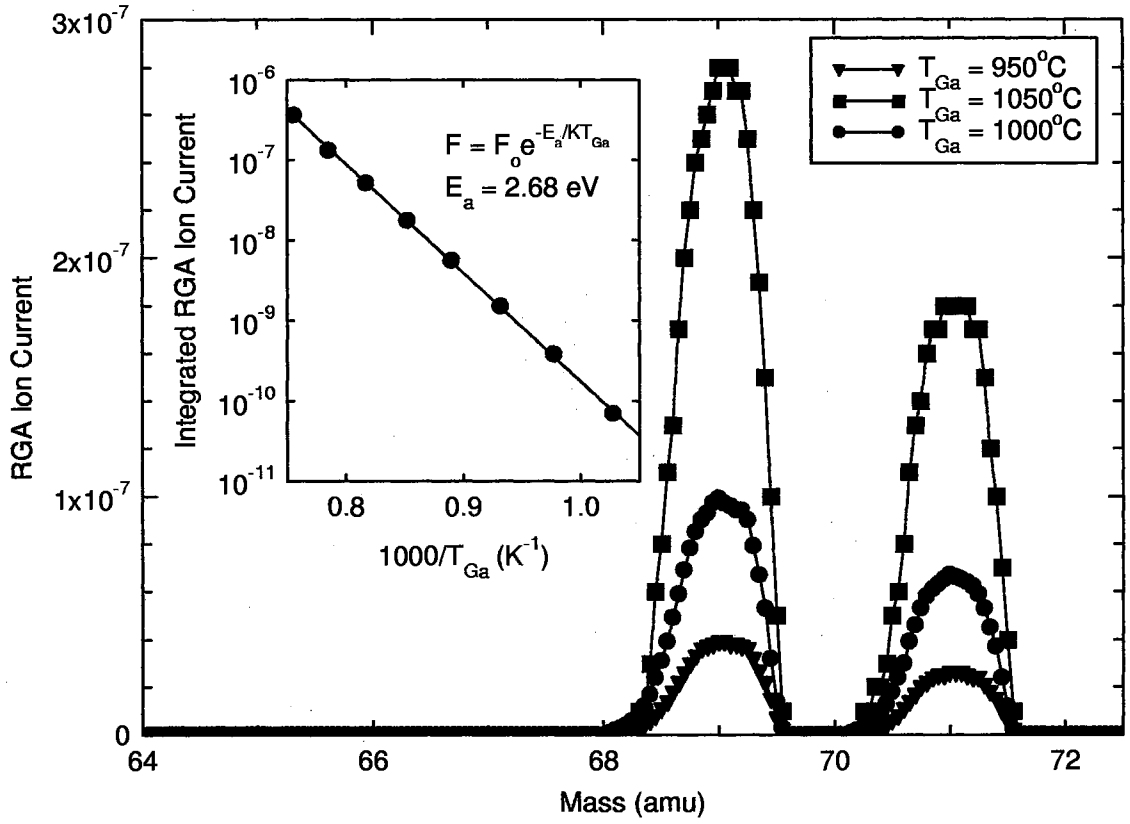

Figure A.8. Use of the `rga_scan` program to calibrate Ga effusion cell flux. The `rga_scan` program extracts mass spectra, allowing detailed analysis of the gases present in the MBE chamber. As an example of the utility of this, integration of the Ga peaks in the mass spectra provides the most accurate measure of the Ga flux at various temperatures. Peaks of 69 and 71 amu correspond to different isotopes of Ga. Inset: An Arrhenius plot of the Ga flux temperature dependence is used to calibrate the effusion cell.

```
#  This file contains scan control and conversion parameters for the
#  mbe_status and mbe_scan programs.
#
#  Each control line in this file causes mbe_status or mbe_scan to
#  perform a specific task (scan a channel) and print the results
#  to the appropriate place.  There may be as many or as few control
#  lines as needed.
#
#  The format of the control lines in this file are as follows:
#  string type a b c format comments
#
#  string should contain the control string to be sent to the
#  Keithley DMM2000 multimeter in the 196 DMM series language.
#
#  type indicates what type of fit is used to convert the
#  DMM output to data.  The valid types are:
#       type            conversion
#     ------------------------------------
#        0              No output for this channel
#        1              y=a*x+b  (c ignored)
#        2              y=a^(b*x+c)
#
#  The double precision numbers a, b, and c are conversion
#  parameters for the various scan channels of the Keithley DMM2000.
#
#  format is a string indicating the format of the output data for that
#  scan item.  The normal rules used in "printf" statements in C
#  programming apply.
#
#  All entries on a line must be separated by at least one space.  Only
#  spaces should be used between columns.  Anything following the "c"
#  column is ignored as a comment.  All comments lines must have a "#"
#  as the first character.  Null lines will cause nasty results.
#
# string      type  a          b         c         format   comments
F0R0N2X       1     4500.0     351.0      0.0      %6.2f    Opt Pyro
F0R0N4X       1     120.0      0.0        0.0      %6.2f    RF For Pow
F8R0N1J1O1X   0     0.0        0.0        0.0      ----     TC Cold Ref
F8R0N3J1O1X   1     1.0        0.0        0.0      %5.2f    RT TC Reading
F0R0N6X       2     10.0       -50.0      -9.0     %4.2e    Ion Pump
F0R0N7X       2     10.0       1.003      -10.02   %4.2e    Ion Gauge
F0R0N9X       1     19.228     -0.5672    0.0      %4.1f    Stage
F0R0N10X      1     19.954     -0.5886    0.0      %4.1f    Ga cell
F0R0N8X       1     19.654     -0.042     0.0      %4.1f    In cell
```

Figure A.9. The current configuration file, /etc/mbe.conf, for the **mbe_scan** and **mbe_status** programs. Lines beginning with # are comments. Command lines contain six columns, and may be followed by comments. The purpose of the columns, respectively, is: (1) controlling the DMM reading in the Keithley 196/199 Series DMM Language, (2) indicating the conversion method needed for a data sample, (3-5) providing calibration parameters for data conversion, and (6) formatting the output of converted data.

take. Each command line is executed in the order that it appears in the configuration file. The command lines are composed of six columns each having a specific function. The first column is a string written to the Keithley DMM instructing it to perform a specific measurement on a specific channel. The string sent to the DMM follows the standard language of the Keithley 196/199 series multimeters. After execution of the measurement, the programs read the data from the DMM data buffer, and processes it according to the parameters in columns 2-5. Column 2 indicates the type of conversion to be performed: linear, exponential, or none at all. Columns 3-5 provide the calibration parameters needed for the conversion of the voltage data to MBE growth parameters. Column 6 contains a format string that determines the output of the computed growth parameters that will be output to the screen or to a file. The format string in column 6 is used directly in the C `printf` or `fprintf` statement, and the standard rules for formatting in the C-programming language apply.* Any information following column 6 or any lines beginning with a # are ignored by these two programs.

The `mbe_status` program is most commonly executed remotely by individual users to check the current status of the MBE system. The `mbe_scan` program is most commonly used to systematically log data at a rapid rate during MBE growth runs and at a slow rate while the system is idle. During growth, the `mbe_scan` program is typically executed once per minute by the UNIX cron daemon. By acquiring data is this way, a detailed log of the key growth parameters and their fluctuations is obtained. A example of the data obtained by the `mbe_scan` program during the growth of a typical GaN epilayer is presented in Fig. A.10 on p. 136. The figure shows the voltage applied to the wafer heater and Ga effusion cell (expressed as a fraction of the maximum possible voltage), the pressure in the growth chamber as measured by

*The rules for formating C `printf` and `fprintf` statements are well documented elsewhere.[49]

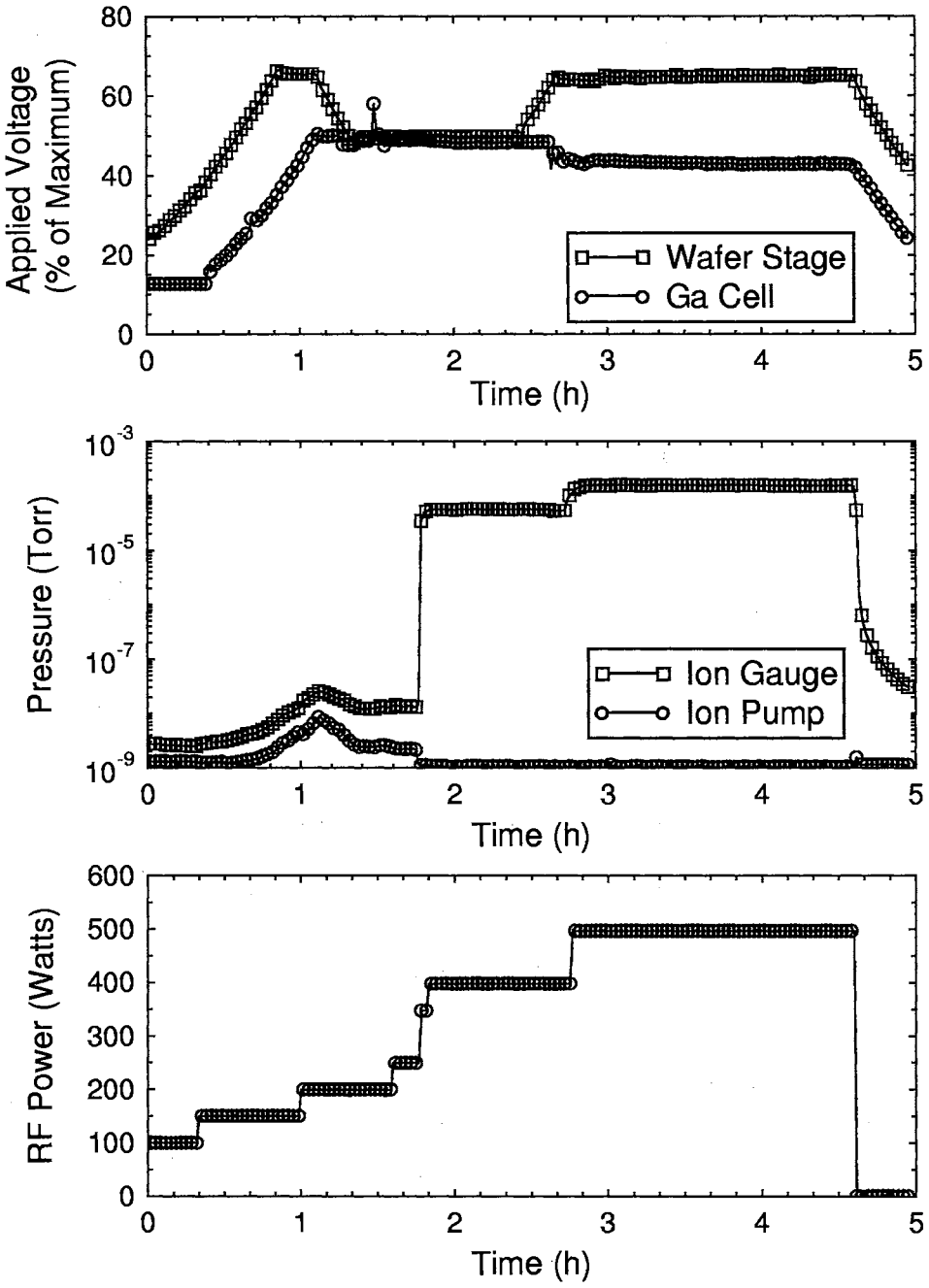

Figure A.10. Shown is growth data acquired using the **mbe_scan** program during a typical GaN epilayer deposition. The parameters presented are the voltage applied to the sample heater and Ga effusion cell (as a fraction of the maximum voltage), pressure readings from the ion gauge and main ion pump, and RF forward power applied to the N* plasma source. Details of the growth process are discussed in Chap. 2.

the ion gauge and the pressure in the ion pump, and the forward RF power delivered to the N* plasma source. As can be seen in the figure, even small fluctuations of the growth parameters are recorded for detailed analysis.

VITA

MARK L. O'STEEN

Candidate for the Degree of

Doctor of Philosophy

Thesis: PLASMA-ASSISTED MBE GROWTH KINETICS AND CHARACTERIZATION STUDIES OF WIDE BANDGAP III-V EPITAXIAL MATERIALS

Major Field: Physics

Biographical:

Personal Data:Born in Denison, Texas, on March 23, 1971, the son of Jim and Karen O'Steen.

Education:Graduated from Durant High School, Durant, Oklahoma in May 1989; received Bachelor of Science degree in Physics and Mathematics from Southeastern Oklahoma State University, Durant, Oklahoma in May 1993. Received Master of Science degree in Physics from Oklahoma State University, Stillwater, Oklahoma in December 1995. Completed the requirements for the Doctor of Philosophy degree with a major in Physics at Oklahoma State University in December 2000.

Professional Memberships:American Physical Society, Material Research Society.